

Dual-phase-lag heat conduction and thermally induced vibration in beams
and shells of different sizes

by

Aminallah Pourasghar

A thesis submitted in partial fulfillment of the requirements for the degree of

Doctor of Philosophy

Department of Mechanical Engineering

University of Alberta

© Aminallah Pourasghar, 2020

Abstract

The conventional form of heat conduction, Fourier's law, has broad and successful applications in the thermal systems which have a large spatial dimension with the focus of its long time behavior. However, for problems involving high temperature gradient, materials with porosity or multiple phases, ultrafast heating and/or, micro/nano-scale heat conduction, the Fourier heat conduction is not accurate. This is due to the incorrect assumption of the infinite speed of heat propagation, which in turn, comes from the inability of Fourier heat conduction in considering the microstructural interactions and nonhomogeneity effect of the material

The field of Thermal Stresses lies at the crossroad of Stress Analysis, Theory of Elasticity, Thermoelasticity, Heat Conduction Theory, and advanced methods of Applied Mathematics. Each of these areas is covered to some extent and explained step by step in this thesis. The heat conduction theory employed here eliminates the paradox of an infinite velocity of heat propagation by employing a more general, functional relation between heat flow and temperature gradient than the existing theory. Also, as a first attempt, the combined application of the differential quadrature method (DQM) and the Newton Raphson method is used to solve the hyperbolic (non-Fourier) and dual-phase-lag (DPL) heat conduction equations to obtain temperature, displacements and nonlinear frequency in the functionally graded (FG) nanocomposite Timoshenko beam and cylinder of different sizes. The hyperbolic heat conduction is solved to obtain temperature in the spatial and temporal domains. Then by implementing the obtained temperature in thermoelastic equations, the displacements and stresses are obtained at each time step. Here, the time domain is divided into a few blocks. In each block, there are several time levels, and the

numerical results at these time levels are obtained simultaneously. Through this way, the numerical solution at the $(n+1)$ th time level depends on the solutions at previous levels from the 1st to the n th levels. The results in the temporal domain are obtained using the Newton-Raphson method.

In general, the variation of temperature field within an elastic continuum results in thermal stresses. So, thermally induced vibration is investigated after obtaining the temperature distribution and thermal forces of carbon nanotube (CNT) reinforced nanocomposite beams and shells. The influence of temperature field in the governing equations of thermoelasticity is reflected through the constitutive law. The theory of linear thermoelasticity is based on linear addition of thermal strains to mechanical strains. All material properties such as heat capacity (C_p), thermal relaxation time (τ), density (ρ) and thermal conductivity (K) are considered as a function of both temperature and CNT volume fraction. While the equilibrium and compatibility equations of the nanocomposite remain the same as for elasticity problems, the main difference rests in the constitutive law where the effect of volume fraction and distribution of CNTs is reflected in the thermoelastic response of nanocomposite.

It has been shown that in certain situations, non-Fourier heat conduction models such as the Cattaneo and Vernotte (CV) and DPL show interesting results like temperature overshoot phenomena observed in a slab subjected to sudden temperature rise on its boundaries. As the vast majority of devices with micro- and nano-scale dimensions emerge in various micromechanical and microelectronic systems, it seems crucial to accurately measure the imposed temperature. The overshooting phenomenon, which is investigated in this research may lead to permanent damages on the sensitive electrical devices if not

handled properly. Accordingly, the effects of this phenomenon on the deformation, and vibrational behavior of the beams and shells are investigated to recognize the importance of using non-conventional heat conduction methods. We showed that non-Fourier heat conduction models would play important roles in the thermoelastic design of nanocomposite structures.

Acknowledgements

First and foremost, I would like to express my sincerest gratitude and appreciation to my supervisor, Prof. Zengtao Chen for his guidance, continuous support and excellent supervision throughout the course of my doctoral program. His unremitting pursuit of truth sets me an example of a true scholar. Completion of this research program would have been impossible without his support, hard work, and encouragement.

To my family, particularly my parents, sister and brother, thank you for your love, support, and unwavering belief in me. Without you, I would not be the person I am today. Your long-lasting love and support across so many years are indispensable to me and all my achievements.

Above all I would like to thank my wife Ameneh for her love and constant support, for all the late nights and early mornings, and for keeping me sane over the past few months. Thank you for being my muse, editor, proofreader, and sounding board.

Table of Contents

Abstract	ii
Acknowledgements	v
Chapter 1:	
Overall introduction	1
1.1 Motivations and objectives	1
1.2 History	2
1.3 Fourier heat conduction.....	3
1.4 Hyperbolic (single-phase-lag) heat conduction.....	3
1.5 Dual-phase-lag heat conduction.....	4
1.6 Nonlocal Heat Conduction.....	5
1.7 Thermally induced vibration	6
Chapter 2:	
Dual-phase-lag heat conduction in the composites by introducing a new application of DQM	9
2.1 Introduction	10
2.2 DQ solution of governing equations	12
2.3 Problem description	13
2.4 Results and discussion	17
2.4.1 Validation	17
2.4.2 Results	18
2.5 Conclusion	24
Chapter 3:	
Dual-phase-lag heat conduction in FG carbon nanotube reinforced polymer composites.....	25

3.1 Introduction	26
3.2 Carbon nanotubes: Thermal conductivity (K), relaxation time (τ) and heat capacity (C) of CNTs	29
3.3 Composites reinforced with randomly oriented, straight CNTs	30
3.4 GDQ solution of governing equations	35
3.5 Dual-phase-lag heat conduction.....	36
3.6 Conclusion.....	48
 Chapter 4:	
Nonlocal thermoelasticity: nonlocal heat conduction in nanostructures by new application of DQM	
49	
4.1 Introduction	49
4.2 Nonlocal heat conduction.....	52
4.3 Nonlocal heat conduction analysis of carbon nanotubes (CNTs)	52
4.4 Solution method	54
4.5 Results and discussion.....	56
4.5.1 Validation	56
4.5.2 Numerical results and discussion	56
4.6 Conclusion.....	65
 Chapter 5:	
Nonlinear vibration and modal analysis of FG nanocomposite sandwich beams reinforced by aggregated CNTs.....	
66	
5.1 Introduction	66
5.2 Material properties of CNT reinforced composites	69
5.2.1 Effect of CNT aggregation on the properties of the composite.....	69
5.3 Equations of motion	73
5.4 Solution method, DQM.....	77

5.5 Results and discussion	79
5.5.1 Verification.....	79
5.5.2 Discussion.....	81
5.6 Conclusion.....	90

Chapter 6:

Effect of hyperbolic heat conduction on the linear and nonlinear vibration of CNT reinforced size-dependent functionally graded microbeams	92
6.1 Introduction	93
6.2 Hyperbolic (Non-Fourier) heat conduction.....	96
6.3 Thermal conductivity (K), relaxation time (τ) and heat capacity (C_p) of CNT....	100
6.4 Composites reinforced with randomly oriented, straight CNTs	101
6.5 Equations of motion	103
6.6 GDQ method	106
6.7 Results and discussion.....	109
6.7.1 Verification.....	109
6.8 Conclusion.....	118

Chapter 7:

Thermally induced vibration in nanocomposites cylindrical panel subjected to heat pulse.....	120
7.1 Introduction	121
7.2 Generalized differential quadrature solution of governing equations	124
7.3 Problem description	125
7.3.1 Non-Fourier heat conduction.....	125
7.3.2 Thermal conductivity (K), relaxation time (τ) and heat capacity (C_p) of CNT.	127
7.3.3 CNT-reinforced composite.....	128
7.4 Thermoelastic solution of the cylindrical panel	130

7.5 Results and discussion.....	134
7.5.1 Validation and comparison studies.....	134
7.5.2 CNT reinforced cylindrical panel.....	136
7.6 Conclusions	145
Chapter 8:	
Conclusions and future perspectives.....	146
8.1 Conclusions.....	146
8.2 Recommendations for future work.....	148
References.....	150

List of Tables

Table 3. 1 Time delays for SWCNT.....	30
Table 5. 1 Material properties of equivalent fiber [136].....	80
Table 5. 2 Comparison of dimensionless nonlinear frequency ω_{nl} / ω_l for UD-CNTRC beams ($L/h=10$).....	81
Table 5. 3 Nonlinear frequency ω_{nl} for C-C CNTRC sandwich beams ($L/h=10, q=1, V_i=0.05, V_o=0.1, \eta=0.4, \mu=0.4$).....	83
Table 5. 4 Nonlinear frequency ω_{nl} for H-H CNTRC sandwich beams ($L/h=10, q=1, V_i=0.05, V_o=0.1, \eta=0.4, \mu=0.4$).....	84
Table 5. 5 Nonlinear frequency ω_{nl} for C-H CNTRC sandwich beams ($L/h=10, q=1, V_i=0.05, V_o=0.1, \eta=0.4, \mu=0.4$).....	84
Table 6. 1 Material properties of the specimen [37].....	99
Table 6. 2 Comparison of dimensionless nonlinear frequency ω_{nl} / ω_l for UD-CNTRC beams ($L/h=10$).....	110
Table 6. 3 Thermal effect on the dimensionless natural frequencies for the microbeams with $L/h=10$ and $h/l=2$	111
Table 6. 4 Dimensionless linear and nonlinear frequencies of FGM microbeams with various length scale parameters and CNT volume fraction at different time steps ($L/h=12, BC=C-C, q=1$).....	114

List of Figures

Figure 2. 1 Implementation of DQ and Newton-Raphson method in the hyperbolic type DPL heat conduction equation	14
Figure 2. 2 Convergence study of the presented DQM ($t^* = 0.2$).....	16
Figure 2. 3 Comparison between the two different solution method, 1: DQM (Present method) 2: Fourier transformation [35]	177
Figure 2.4 Effects of the phase lags of heat flux and temperature gradient on temperature and heat flux distribution	1919
Figure 2. 5 Time evolution of the temperature ($^{\circ}\text{C}$) at different temperature gradient and heat flux time lags	200
Figure 2. 6 Time evolution of the heat flux at different temperature gradient and heat flux time lags	211
Figure 2. 7 Effects of heat flux time lag in temperature history in case of DPL heat conduction	222
Figure 2. 8 Time evolution of the temperature at different points along the thickness of the beam in case of DPL heat conduction	233
Figure 3. 1 Representative volume element (RVE) with randomly oriented, straight CNTs	34
Figure 3. 2 Configuration of block-marching technique and mesh point distribution in each block.....	37
Figure 3. 3 One-dimensional heat conduction through a slab	38
Figure 3. 4 Variation of the time lags and thermal conductivity through the thickness of the nanocomposite	40
Figure 3. 5 Transition from non-Fourier heat conduction to Fourier heat conduction by changing the time duration of thermal shock on boundary condition at $x=0.23h$	42
Figure 3. 6 Temperature and heat flux history in different volume fraction of CNT at $x=0.23h$	43
Figure 3. 7 Temperature history at different locations of the thickness of the medium	44
Figure 3. 8 Time evolution of the heat flux at different points along the thickness of the medium	46
Figure 3. 9 Time evolution of the temperature at different points along the thickness of the medium at $x=0.23h$	47
Figure 4. 1 Single wall carbon nanotube (SWCNT) modeled as a nonlocal Timoshenko nanobeam	53
Figure 4. 2 Time history of the temperature distribution at different points through the thickness.....	58

Figure 4. 4 Temperature distribution through the thickness by changing the time duration of the thermal shock (t^*) (a) Boundary conditions, (b) temperature distribution across the thickness of the carbon nano-tube at $t = 20$ fs.	5959
Figure 4. 5 Effects of the characteristic length (l) on the temperature distribution at $t = 20$ fs.	60
Figure 4. 6 Effects of the relaxation time on the temperature distribution at $t = 20$ fs.	61
Figure 4. 7 Temperature history of the temperature, BC: II	62
Figure 4. 8 Visualizing temperature with single heatmap, BC: II	63
Figure 4. 9 Transition from non-Fourier heat conduction to Fourier heat conduction at $t = 20$ fs.	64
Figure 4. 10 Effects of the thickness ratio on the temperature distribution	64
Figure 5. 1 RVE with Eshelby cluster model of aggregation of CNTs.....	70
Figure 5. 2 Geometry of FGS-CNTR beam.....	72
Figure 5. 3 Variation of the CNT volume fraction through the thickness of the beam (q is the volume fraction index).....	73
Figure 5. 4 The variation of Young's modulus and along the thickness of the FGS-CNTR beam with aggregation effect.....	82
Figure 5. 5 Nonlinear mode shapes of CNTRC sandwich beams at $w_{max}=0.5$ and $L/h=15$: (a) C–C, (b) H–H and (c) C–H ($V_i=0.05$, $V_o=0.1$).....	86
Figure 5. 6 Nonlinear mode shapes of CNTRC sandwich beams at $L/h=15$ for C–H boundary condition...87	
Figure 5. 7 Effect of core thickness on the nonlinear frequency ratio versus dimensionless amplitude curves of the CNTRC beams with $q=1$ $V_i=0$, $V_o=0.05$ and $L/h=15$ (a) C–C, (b) H–H	88
Figure 5. 8 Effect of state of aggregation on the nonlinear frequency ratio versus dimensionless amplitude curves of the CNTRC beams with $q=1$	90
Figure 6. 1 Geometry of the microbeam.....	96
Figure 6. 2 Convergence study of the presented DQM ($t^* = 0.2$).....	98
Figure 6. 3 Comparison of solving techniques with results available in the literature (Mitra et al., 1995) (Fourier, hyperbolic and experimental data).....	99
Figure 6. 4 Representative volume element (RVE) with randomly oriented, straight CNTs	102
Figure 6. 5 Time evolution of the temperature at different points along the thickness of the beam.	112

Figure 6. 6 Time evolution of nonlinear frequency and thermal force (N_T^*) $L/h=12$ and BC=C-C, a: $h/l=1.7$ b: $h/l=3.4$	113
Figure 6. 7 Temperature along the thickness of the microbeam after 0.05 Second ($dt=0.0001$, $h=30 \mu\text{m}$).	115
Figure 6. 8 Effects of amplitude curves W_{max} on nonlinear frequency for the microbeam as a function of L/h with $h/l=2$: (a) S-S, (b) C-C and (C) C-S	116
Figure 6. 9 Effects of amplitude curves W_{max} on nonlinear frequency for the microbeam as a function of h/l with $L/h=12$: (d) S-S, (e) C-C and (f) C-S	116
Figure 6. 10 Effect of temperature at different time steps on the non-dimensional nonlinear frequency for the microbeam $h/l=1.7$, $L/h=12$, BC=C-C	118
Figure 7. 1 Geometry of cylindrical panel.....	125
Figure 7. 2 Comparison of the non-dimensional radial and circumferential displacement under uniform Thermal load.....	135
Figure 7. 3 Time evolution of the temperature ($p=1$)	137
Figure 7. 4 Effect of temperature at different time steps on the non-dimensional displacements and stresses of cylindrical panels when $q(r_i, t)$ is imposed ($p=1$).....	138
Figure 7. 5 Time evolution of the temperature ($p=1$)	140
Figure 7. 6 Effect of temperature at different time steps on the non-dimensional displacements and stresses of cylindrical panels when $T(r_i, t)$ is imposed ($p=1$).....	141
Figure 7. 7 Effect of temperature at different time steps on the non-dimensional displacements and stresses of cylindrical panels when $T(r_i, t)$ is imposed ($V_i=V_o=0.03$).....	143
Figure 7. 8 Effect of different pattern of CNT distribution at first second on the non-dimensional radial displacement and stresses of cylindrical panels when $T(r_i, t)$ is imposed	144

Chapter 1:

Overall introduction

1.1 Motivations and objectives

It has been shown that when the thickness of a medium is within a certain range and temperature gradient is sufficiently high, non-Fourier heat conduction models such as the Cattaneo and Vernotte (CV) and dual-phase-lag (DPL) show interesting results like temperature overshoot phenomena or heat wave interference. Furthermore, thermal resonance may exist with an appropriate heat source or boundary condition in DPL or hyperbolic heat conduction in which thermal waves exist. The resonance will significantly enhance the heat transfer process in nanofluids and multi-phase media. This phenomenon could damage electronic or mechanical devices if it is not appropriately handled.

Furthermore, Fourier and Laplace transforms can be used to solve the non-Fourier heat conduction problems, but for problems with complex geometries, integral transform based methods face some challenges in transform inversion. Also, the calculated temperatures by these transforms are inaccurate at early stages, as many previous studies shown [references]. These challenges motivated the author to use a different methodology to cope with these problems.

The main objectives of this research are: (1) developing a methodology to deal with non-Fourier heat conduction problems; (2) investigating the heat conduction in small scale through nonlocal thermoelasticity; (3) presenting the unique effect of non-Fourier heat conduction on the thermomechanical behaviour of the material.

To reach the research objectives as aforementioned, the differential quadrature method (DQM) to solve for the first time, the nonlinear DPL heat conduction equations while the materials

and properties are geometry- and temperature-dependent to obtain the temperature distribution. Then the obtained temperature is employed in the thermoelastic equations of a slab, a microbeam, and a shell to obtain displacements and frequency at each time step by direct iterative method.

In this study, all material properties such as Young's modulus (E), heat capacity (C_p), relaxation time (τ), density (ρ) and thermal conductivity (K) are considered as a function of temperature and CNT volume fraction. The effects of temperature change, thermal conductivity, CNTs volume fraction, length to span ratio, heat flux, and end support conditions on the linear and nonlinear vibration of beams or shells are discussed in detail.

1.2 History

Heat conduction is a traditional subject that dated back to the eighteen's century, when Fourier's conduction law was established. The heat conduction research based on Fourier's conduction law usually focuses on how to transfer heat efficiently for heating or cooling objects. Heat propagation in solids, traditionally, has been interpreted as either a diffusion or a wave phenomenon. When there is no heat generation, the diffusion theory leads to a decayed temperature in time due to presence of the first order time-derivative in the diffusion equation. On the other hand, the thermal wave model engages the wave term in the energy equation which introduces a sharp wavefront in the history of thermal wave propagation. As a result, several physical phenomena will be revealed that cannot be reflected by diffusion [1].

In the past three decades, with the development of short pulse laser technique and fabrication of nanomaterials, the validation of Fourier's law has been challenged. In studies on ultrafast laser heating of materials from the 1980s, it is observed that the temperature response on laser heating exhibits the behavior of lagging, relaxation, or delay, which indicates the failure of Fourier's law. On the other hand, in low-dimensional materials such as carbon nanotubes and

graphene, as well as nanosized semiconductors, the heat conduction shows a size-dependent behavior.

1.3 Fourier heat conduction

In one-dimensional, steady-state heat flow, thermal conductivity of a material is a parameter that relates the rate of heat conduction to the temperature gradient of the bulk material, and it assumes that heat flux and temperature gradient occur at the same time instant. This means that heat disturbances, with parabolic-type heat conduction equation, need to spread at an infinite speed [2] as shown in the following equation.

$$q(x, t) = -k\nabla T(x, t) \quad (1.1)$$

where $\nabla T(x, t)$ is the temperature gradient, which is a vector function of the position vector \mathbf{x} and the time variable t , $q(x, t)$ is the heat flux, and k is the thermal conductivity. Even though Fourier heat conduction has been used to solve most engineering problems at classical length and time scale successfully, it cannot model situations involving low temperatures near absolute zero, high-temperature gradient, and very high frequencies of heat flux [3,4].

1.4 Hyperbolic (single-phase-lag) heat conduction

The heat conduction theory presented here eliminates the paradox of an infinite velocity of propagation by employing a more general, functional relation between heat flow and temperature gradient than the existing Fourier's theory.

Besides, because the heat flux and the temperature gradient are simultaneous, one cannot differentiate between the cause and effect of heat flow which is critical for the transient behavior at an extremely short time, for example on the order of picoseconds to femtoseconds [5]. Also, in the absence of heat source, in the Fourier heat conduction, the temperature will reach its maximum or minimum value at the boundary of the medium at the first instant. However, for the heat

conduction models such as the hyperbolic, Cattaneo and Vernotte (CV) and dual-phase-lag (DPL) models, the temperature of some inner regions in the medium may exceed the temperature at the boundary which is called the overshooting phenomenon. Evidently, this phenomenon may lead to the damage of electronic or mechanical devices if it is not appropriately handled [6]. So, the hyperbolic heat conduction equation is introduced based on the Cattaneo and Vernotte for the heat flux to incorporate a relaxation mechanism in order to gradually adjust to a change in the temperature gradient [7,8]. This theory eliminates the paradox of an infinite velocity of heat propagation by employing a more general, functional relation between heat flow and temperature gradient than classical theory and can yield the hyperbolic diffusion equation within the continuum assumption. In the hyperbolic (single-phase-lag) model,

$$q(x, t + \tau_q) = -k\nabla T(x, t) \quad (1.2)$$

where τ_q is the time lag of the heat flux. The temperature gradient always precedes the heat flux vector. A new time integration scheme proposed by Fung [9] based on the differential quadrature method (DQM) to solve Eq (1.2) in a continuum can be used, as it was illustrated that the scheme is unconditionally stable. By using the same concept, Rahideh et al. [10] employed the layerwise-incremental DQM to show the effect of heat wave speed on the thermal characteristics of a multi-layered domain made of functionally graded materials.

1.5 Dual-phase-lag heat conduction

Multiphase systems are not following Fourier's law as well, such as in nanofluids, porous media, and biomaterials [11,12]. To mitigate the deviations from Fourier's law, Tzou [12] introduced dual-phase-lag (DPL) heat conduction as

$$q(x, t + \tau_q) = -k\nabla T(x, t + \tau_T) \quad (1.3)$$

where τ_T is the time lag of the temperature gradient. This model can capture the effect of heat

conduction with high heat flux and short heating period. For example, Dai et al. [13] developed a new higher-order finite difference scheme for solving the DPL equation in nano heat conduction with the temperature jump boundary condition. Furthermore, if $\frac{\tau_q}{\tau_T} > 1$, Eq. (1.3) is hyperbolic and thermal waves will be produced in the heat conduction process. If, otherwise, $\frac{\tau_q}{\tau_T} \leq 1$, this equation is parabolic and thermal waves do not exist [14].

1.6 Nonlocal Heat Conduction

Many studies about CNTs and nanoscale structures were based on the classical continuum theory, which ignores the strong size effect [15]. To tackle this problem, nonlocal elasticity theories were introduced for the nanoscale structures to develop size-dependent material relations [16]. These approaches have shown superior performance in coping with this problem over any other approach. Furthermore, there have been lots of research on the heat conduction of nanostructures theoretically [17,18] and experimentally [19]. They showed that improvement of thermal contact to initially rough metal electrodes is attributed to the local melting of metal surface under laser heating.

In the classical model, the temperature gradient causes heat flux at the same point. At the nanoscale, a sufficient number of collisions among energy carriers are required for heat transport to take place [20]. In general, quantifying the value of a physical property at one point through another physical property in a region near that point is considered as the nonlocal treatment in the continuum theory, which has been supported by experimental results [21].

Based on the investigations of Soboley [22] and Tzou [12], since heat flux at micro/nano scale is substantially nonlocal, classical models should be modified using nonlocal theory by introducing the characteristic length of the material. Prior research generally confirms that at the

nanoscale, heat transfer is quite different from that estimated by classical laws. To tackle this problem, Guyer and Krumhansl (GK) [23, 24] introduced a generalized model by considering the characteristic length of the material as follows:

$$q(z, t + \tau_q) = -k\nabla T(z, t) + l^2\nabla^2 q(z, t) \quad (1.4)$$

where τ_q and l are the time lag of heat flux and internal characteristic length, respectively. To investigate the transient heat conduction from nano- to macro-scales, Wang et al. [25] considered the effects of both non-Fourier heat conduction and the nonlocality of the problem simultaneously. Xu [26] investigated the nanoscale heat conduction in silicon thin films by considering the temporally and spatially nonlocal effects. They showed thermal wave propagation in nanoscale materials.

1.7 Thermally induced vibration

The history of thermoelasticity and thermal stresses is much younger than the history of the theory of elasticity, albeit, from the literature review, it is noted that the temperature effect on the linear and nonlinear vibrations of microscale structures has been an object of many studies. However, thermally induced vibration of structures under transient heat conduction along with considering the size effect have not been studied yet. In this thesis, the thermally induced vibration behaviors of carbon nanotube (CNT) reinforced functionally graded (FG) microbeam have been studied based on the hyperbolic heat conduction.

As a first step, non-Fourier heat conduction in the beam with temperature-dependent material properties is studied. Then a mathematical model is developed for considering the effect of transient heat conduction on the vibration analysis of nanocomposite beam using differential quadrature method (DQM). Nonlinear free vibration analysis of FG-CNT reinforced composite structures is studied based on the Timoshenko beam theory using Hamilton's principle, Mori-

Tanaka (MT) model, and DQM, a simple and efficient numerical technique for solving partial differential equations [27-30].

This thesis is organized in a paper-based format. It includes eight chapters. All Chapters presented in this thesis except Chapters 1, 3, and 8 have been published or accepted by peer reviewed journals as follows:

- Chapter 2 of this thesis has been published as Paper No. 1. In this chapter, DQM is used to discretize the governing equations of hyperbolic and dual-phased-lag heat conduction in a medium. Then a Newton-Raphson method is used to solve the problem. The effects of time lag on the temperature distribution and heat flux are illustrated.
- Chapter 3 of this thesis has been published as Paper No. 2. In this chapter, the mechanical properties temperature distribution of a CNT reinforced composite are investigated
- Chapter 4 of this thesis is under review as Paper No. 3. In this chapter, the effect of length scale on the thermoelastic behaviour of the nanocomposite material. We introduce nonlocal thermoelasticity and imply the effect of characteristic length on the temperature distribution.
- Chapter 5 of this thesis has been published as Paper No. 4. Nonlinear frequency response of a sandwiched, nanocomposite beam is investigated in this chapter.
- Chapter 6 of this thesis has been published as Paper No. 5. The thermoelastic behaviour of a microbeam is investigated based on non-Fourier heat conduction in this chapter.
- Chapter 7 of this thesis has been published as Paper No. 6. In this chapter, the thermomechanical behaviour of a nanocomposite cylindrical panel is investigated using non-Fourier heat conduction under a thermal shock on the boundary.

1. Paper No. 1: A Pourasghar and Z Chen. "Dual-phase-lag heat conduction in the composites

- by introducing a new application of DQM”, Heat and Mass Transfer, 1-7, 2019.
2. Paper No. 2: A Pourasghar and Z Chen. “Dual-phase-lag heat conduction in FG carbon nanotube reinforced polymer composites”, Physica B: Condensed Matter, 564:147-156, 2019.
 3. Paper No. 3: A Pourasghar and Z Chen. “Nonlocal thermoelasticity: nonlocal heat conduction in single-walled carbon nanotubes”, Journal of Thermal Stresses, Under Review, 2020.
 4. Paper No. 4: A Pourasghar and Z Chen. “Nonlinear vibration and modal analysis of FG nanocomposite sandwich beams reinforced by aggregated CNTs”, Polymer Engineering & Science, 2019, doi: 10.1002/pen.25119.
 5. Paper No. 5: A Pourasghar and Z Chen. “Hyperbolic heat conduction and thermoelastic solution of functionally graded cnt reinforced cylindrical panel subjected to heat pulse”, International Journal of Solids and Structures, 163:117-129, 2018.
 6. Paper No. 6: A Pourasghar and Z Chen. “Effect of hyperbolic heat conduction on the linear and nonlinear vibration of cnt reinforced size-dependent functionally graded microbeams”, International Journal of Engineering Science, 137:57–72, 2019.

Chapter 2:

Dual-phase-lag heat conduction in the composites by introducing a new application of DQM¹

The first application of the differential quadrature method (DQM) in solving the nonlinear dual-phase-lag (DPL) heat conduction equation is demonstrated here. To show the effect of DPL parameters, the temperature response of the medium obtained from Fourier's law, hyperbolic heat conduction, and hyperbolic type DPL heat conduction model were compared. Furthermore, the transient temperature and heat flux distributions have been calculated for various types of dynamic thermal loading. We show whether thermal waves exist in hyperbolic type DPL heat conduction by considering the time lag parameter in the microstructural interactions of fast transient heat conduction. Also, overshooting which is one of the results of considering hyperbolic heat conduction is investigated here. The numerical solution at each time level depends on the solutions at its previous levels. This means the temperature and heat flux obtained at the n th time step are the initial conditions for the $(n+1)$ th time step. After demonstrating the convergence and accuracy of the method, the effects of different parameters on the temperature and heat flux distribution of the medium are studied.

¹ A version of this chapter is published in the journal of *Heat and Mass Transfer*, 1-7, 2019,

2.1 Introduction

In the conventional heat conduction theory, which is based on classical Fourier's law, heat flux and temperature gradient generate at the same time instant. This means that heat disturbances, with parabolic-type heat conduction equation, need to spread at an infinite speed [2] as shown in Eq. (2.1).

$$q(x, t) = -k\nabla(x, t) \quad (2.1)$$

where $\nabla(x, t)$ is the temperature gradient which is a vector function of the position vector x and the time variable t , $q(x, t)$ is the heat flux, and k is the thermal conductivity. It puts up a good performance to construe most engineering problems at classical length and time scale, but cannot fully model situations involving very low temperatures near absolute zero, high temperature gradient, and very high frequencies of heat flux [31-33]. Moreover, because the heat flux and the temperature gradient are simultaneous, one can not differentiate between the cause and effect of heat flow which is critical for the transient behavior at extremely short time, for example on the order of picoseconds to femtoseconds [5]. Also, in the absence of heat source, in the Fourier heat conduction, the temperature will gain its maximum or minimum value at the boundary of the medium or at the initial instant. But for the heat conduction models such as the Cattaneo and Vernotte (C-V) and DPL models, the temperature of some inner regions in the medium may exceed the temperature at the boundary. This phenomenon is called overshooting. Evidently, this phenomenon may lead to the damage of electronic or mechanical devices if it is not handled properly [5, 34]. So, the hyperbolic heat conduction equation is introduced based on the Cattaneo and Vernotte model Eq. (2) for the heat flux incorporates a relaxation mechanism in order to gradually adjust to a change in the temperature gradient [7,8,35, 36]. This model has been a satisfactory extension of classical diffusion theory and can yield the hyperbolic diffusion equation

within the continuum assumption.

$$q(x, t + \tau_q) = -k\nabla(x, t) \quad (2.2)$$

where τ_q is the time lag of the heat flux. In fact, the temperature gradient always precedes the heat flux vector. Rahideh et al. [10] used the layerwise-incremental DQM to show the effect of heat wave speed on the thermal characteristics of a multi-layered domain made of functionally graded materials. The other example of the systems which do not obey Fourier's law are multiphase systems, such as nanofluids, porous media, and biomaterials [11, 37, 38]. To tackle the deviations from Fourier's law, Tzou [1,2] introduced a two phase lags heat conduction, presenting the DPL model as

$$q(x, t + \tau_q) = -k\nabla(x, t + \tau_T) \quad (2.3)$$

where τ_T is the time lag of the temperature gradient. This model is able to capture the effect of heat conduction with high heat flux and short heating periods. Dai et al. [13] developed a higher-order finite difference scheme for solving the DPL equation in nano heat conduction with the temperature jump boundary condition. Furthermore, if $\frac{\tau_q}{\tau_T} > 1$, Eq. (2.3) presents a hyperbolic type heat conduction and thermal waves will be produced in the heat conduction process. If, otherwise, $\frac{\tau_q}{\tau_T} \leq 1$, this equation is parabolic and thermal waves do not exist [14, 39].

Wang and Zhou [40] established methods of measuring the time lags and obtained analytical solutions for the regular 1-D, 2-D and 3-D heat conduction domains under arbitrary initial and boundary conditions. A combination study of the non-Fourier heat conduction with thermalphonon theory has also been performed [41]. Also, Basirat et al. [42] obtained the phase lag values corresponding to the metal films. Values of these parameters are mainly determined experimentally [43, 44] and they are ranged from 0.01 to 32 s. The effect of laser, as a heat source,

on a thin film was studied by Noroozi et al. [45]. They have used the Adomian decomposition to solve the DPL equations, as an approximate-analytical method. Wang et al. [26] presented a peridynamic non-Fourier heat conduction model, in the framework of generalized state-based peridynamics by introducing the concept of dual phase lags into the peridynamic framework, to consider the non-Fourier and nonlocal effects simultaneously.

In summary, the objective of this study is to introduce a new application of differential quadrature method [30, 46] to resolve DPL heat conduction in nanocomposites with considering the nonlinear terms of heat conduction. The proposed method marches in the time direction block by block. In each block, there are several time levels, and the numerical results at these time levels are obtained simultaneously. In this way, the numerical solution at the $(n+1)$ th time level depends on the solutions at its previous levels from the 1st to the n th ($n=1:N_t$) levels. Both the spatial as well as the temporal domain is discretized using the DQM. To the authors' best knowledge, this is the first research on the effects of dual phase lag model based on this method. Using the DQM allows us to choose a relatively coarse grid and obtain a reasonable solution. Also, it is much easier to implement rather than solving heat conduction equations in the Laplace domain or analytically. Moreover, the DQM requires no restriction on the boundary conditions or material properties, and is much easier to apply than other available methods on two or three-dimensional problems.

2.2 DQ solution of governing equations

The general differential quadratur (DQ) approach is used to solve the heat transfer equations. This approach was developed by Shu and co-researchers based on the differential quadrature (DQ) technique [30]. In GDQ method the n th order partial derivative of a continuous function $f(x, t)$ with respect to x at a given point x^i can be approximated as a linear summation of weighted function values at all of the discrete points in the domain of x , i.e.

$$\frac{\partial f(x,t_j)}{\partial x} \Big|_{x=x_i} = \sum_{k=1}^N C_{ik} f(x_{ik}, t_j), \quad (2.4)$$

$$(i = 1, 2, \dots, N_x, j = 1, 2, \dots, N_t)$$

$$\frac{\partial f(x,t_j)}{\partial t} \Big|_{t=t_i} = \sum_{k=1}^N D_{jk} f(x_{ik}, t_j), \quad (2.5)$$

$$(i = 1, 2, \dots, N_x, j = 1, 2, \dots, N_t)$$

where N_x and N_t are the number of sampling points along x and t directions, respectively, also C_{ik} and D_{jk} are the x_i and t_j dependent weight coefficients. Details of this procedure can be found in the literature [47, 48]. In this work, the Chebyshev-Gauss-Lobatto quadrature points are used [30],

$$x_i = \frac{1}{2} \left(1 - \cos \left(\frac{i-1}{N-1} \pi \right) \right), i = 1, 2, \dots, N \quad (2.6)$$

2.3 Problem description

The transient, hyperbolic heat conduction equation is expressed as follows [17]

$$q + \tau_q \frac{\partial q}{\partial t} = -k \left(\frac{\partial T}{\partial x} + \tau_T \frac{\partial^2 T}{\partial x \partial t} \right) \quad (2.7)$$

where τ_q and τ_T were introduced to account for the effects of thermal inertia and microstructural interaction such as electron-phonon interaction or phonon scattering, respectively. Moreover, the energy equation can be written as [1],

$$\rho C \frac{\partial T}{\partial t} + \frac{\partial q}{\partial x} = g(x, t) \quad (2.8)$$

In the above equation, $g(x, t)$ is the heat source which is equal to zero. The DQM is used to discretize the spatial derivatives, and the incremental DQM is employed to discretize the temporal domain. Based on this approach, the total temporal domain is divided into a set of time intervals where the DQ rule is employed to discretize the temporal derivatives. The DQ method being applied to Eqs. (2.7) and (2.8), then the following equations at an arbitrary sampling point x_i and t_j are then obtained:

$$k_{ij}(\tau_T \sum_{m=1}^{N_x} C_{im}^1 T_{mj} \sum_{n=1}^{N_t} D_{in}^1 T_{in}) + k_{ij}(\sum_{m=1}^{N_x} C_{im}^1 T_{mj}) + \tau_q(\sum_{n=1}^{N_t} D_{jn}^1 q_{in}) + q_{ij} = 0 \quad (2.9)$$

$$(\sum_{m=1}^{N_x} C_{im}^1 q_{mj}) + \rho_{ij} C_{ij}(\sum_{n=1}^{N_t} D_{jn}^1 T_{in}) = g_{ij} \quad (2.10)$$

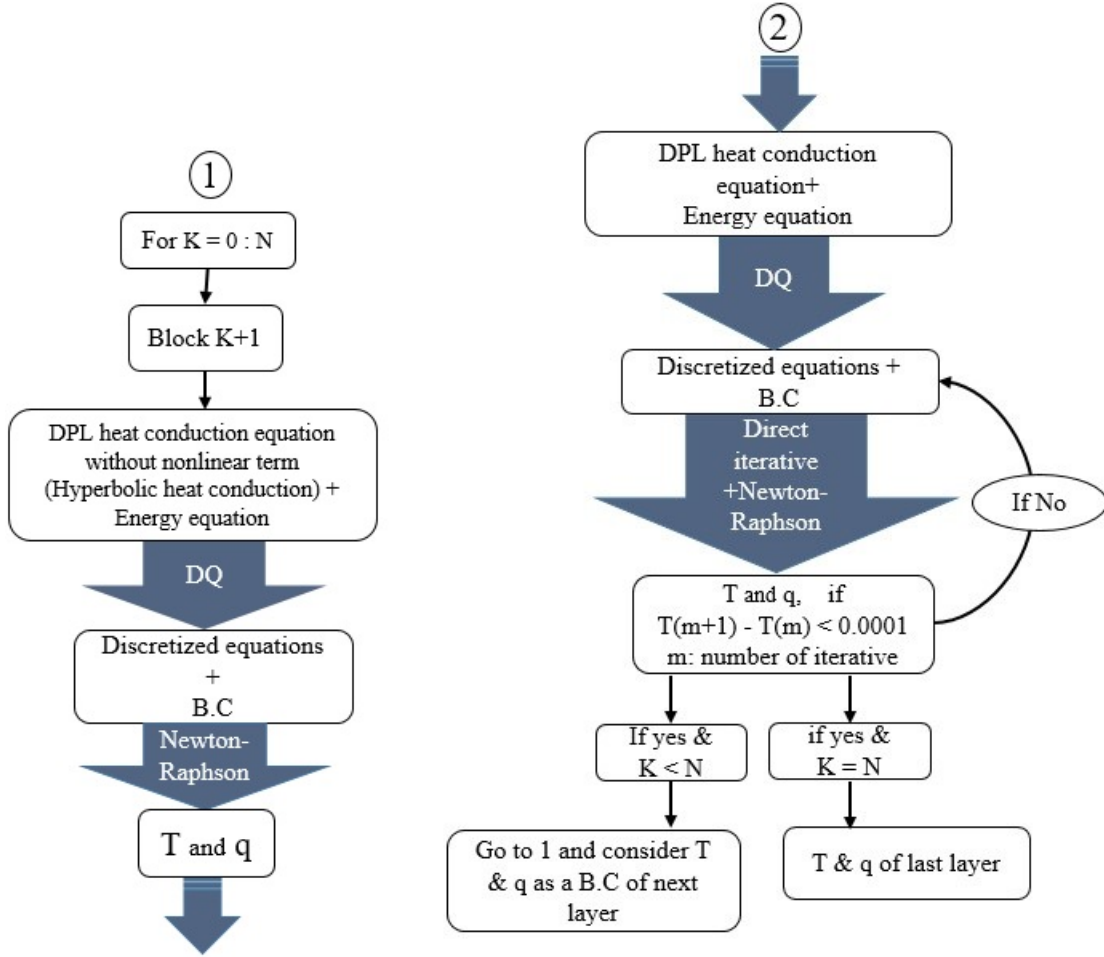


Figure 2. 1 Implementation of DQ and Newton-Raphson method in the hyperbolic type DPL heat conduction equation

Figure 2.1 shows how the hyperbolic type DPL heat conduction equations have been solved by using DQM. In order to solve these nonlinear equations, an iterative procedure is used. To do so, in the first step as shown in Fig 2.1, the nonlinear terms are neglected and the resulting problem is solved. In the second step, the obtained temperature is considered as a first guess of the nonlinear

term in Eq (2.9). Then, the problem is solved again to obtain the new temperature and heat flux. Step 2 is repeated until the discrepancy between the temperatures from the two consecutive iterations is within $0.1 * 10^{-3}$. For this step, at the beginning we are in first time interval ($N_t=1$), and we need to apply DQM in this time interval to obtain the temperature history by having the temperature at the end of each time interval. So, there should be N_{ts} sample points in each block to solve it through DQM. For convenience we considered $N_t = N_{ts}$. After we solved the problem in the first time interval, we can move to the next block ($N_t + 1$) and use the obtained temperature and heat flux as an initial condition for the next block.

Let us consider the beam which is under a sudden temperature change on the lower surface. The boundary conditions of the problem can be expressed as [49,50]:

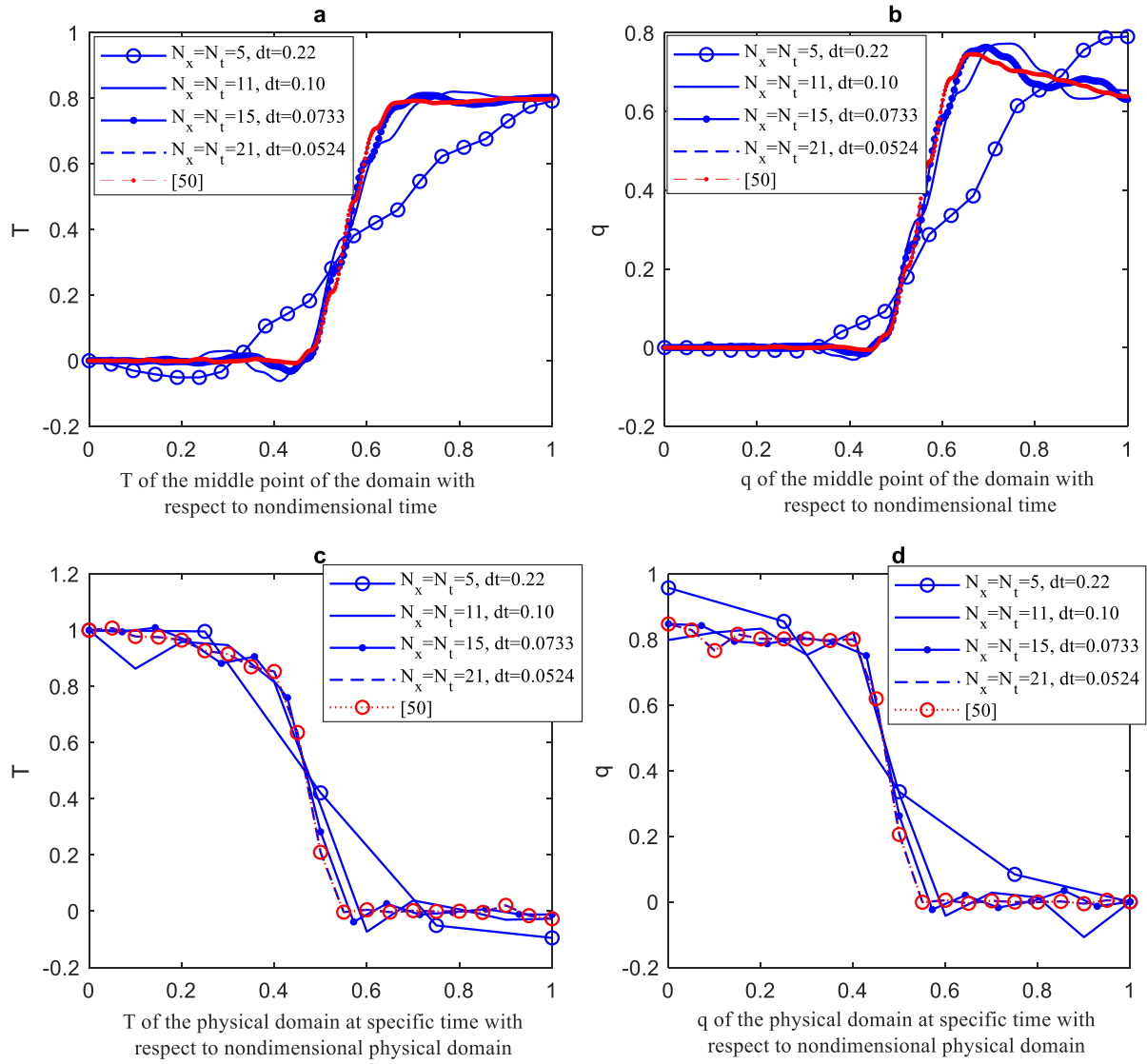


Figure 2. 2 Convergence study of the presented DQM ($t^* = 0.2$).

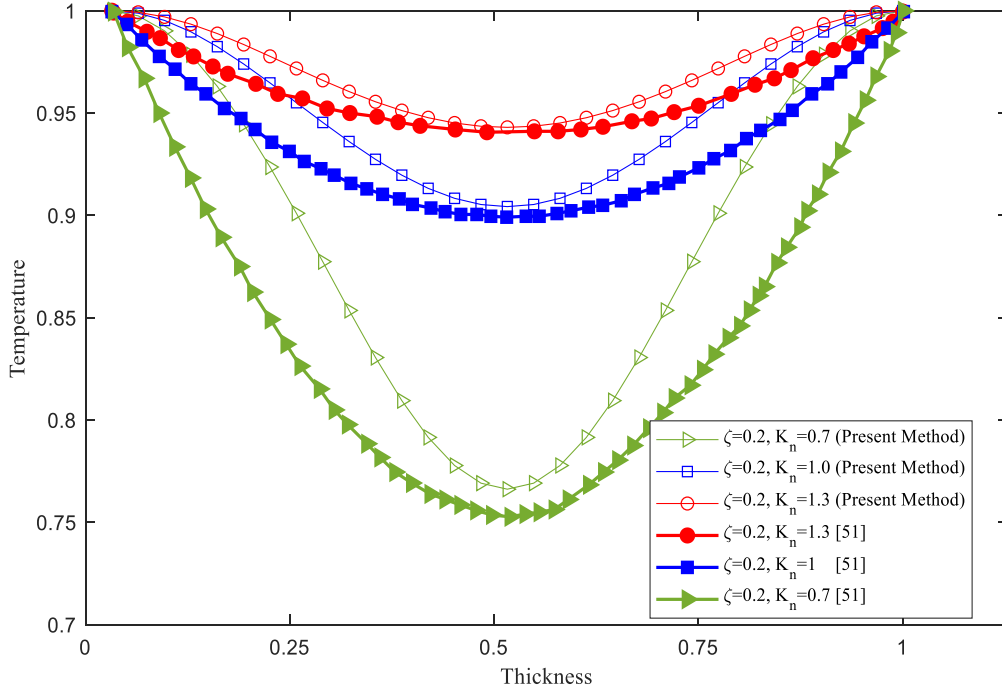


Figure 2. 3 Comparison between the two different solution method, 1: DQM (Present method) 2: Fourier transformation [51]

$$T(0, t) = \begin{cases} 100 \left(\frac{1}{2} + \frac{3}{4} \left(\frac{2t}{t^*} - 1 \right) - \frac{1}{4} \left(\frac{2t}{t^*} - 1 \right)^3 \right) & \text{if } 0 \leq t \leq t^*, \\ 100, & \text{if } t \geq t^* \end{cases} \quad (2.11)$$

$$T(x, 0) = 0,$$

$$q(0, t) = 0,$$

$$q(x, 0) = 0,$$

where $t^* = 0.1$ s in all calculations.

2.4 Results and discussion

2.4.1 Validation

The convergence of the presented DQM is shown in Fig 2.2. The same values for the parameters as those in the work of [50] are considered here. A heating pulse is applied to the lower surface of a plate. The results for convergence behavior of the time history and spatial distribution

of the nondimensional temperature and heat flux are presented as well. It should be noted that $N_t \cdot dt = \text{constant}$. In fact, the whole process is investigated in the same duration of time for all the tests. It is shown that with increasing the number of sample points in both temporal and physical domains ($N_x = N_t$), followed by decreasing the time interval, converged results are obtained. However, this is not enough and the convergence of DQM should be further verified by comparing the results with another method. The present method is validated by comparing the results with those available in [51]. The results are presented for the hyperbolic heat conduction in a slab of nanoscale and compared with published results [51] as shown in Fig 2.3. In [51], the authors solved their problem in the Laplace domain and introduced K_n to consider the effect of nonlocality. As one can see, good agreement is achieved between the current results and the results of [51].

2.4.2 Results

Next, let us consider a heating pulse applied to the left boundary of a parallely sided slab.

The initial and boundary conditions are:

$$\begin{aligned}
 q(0, t) &= \begin{cases} 100 \left(-1 + \left(\frac{2t}{t^*} + 1 \right)^{\frac{2}{3}} \right) & \text{if } 0 \leq t \leq t^*, \\ 0 & \text{if } t \geq t^*, \end{cases} \\
 q(x, 0) &= 0, \\
 q(0, t) &= 0, \\
 T(x, 0) &= 0.
 \end{aligned} \tag{2.12}$$

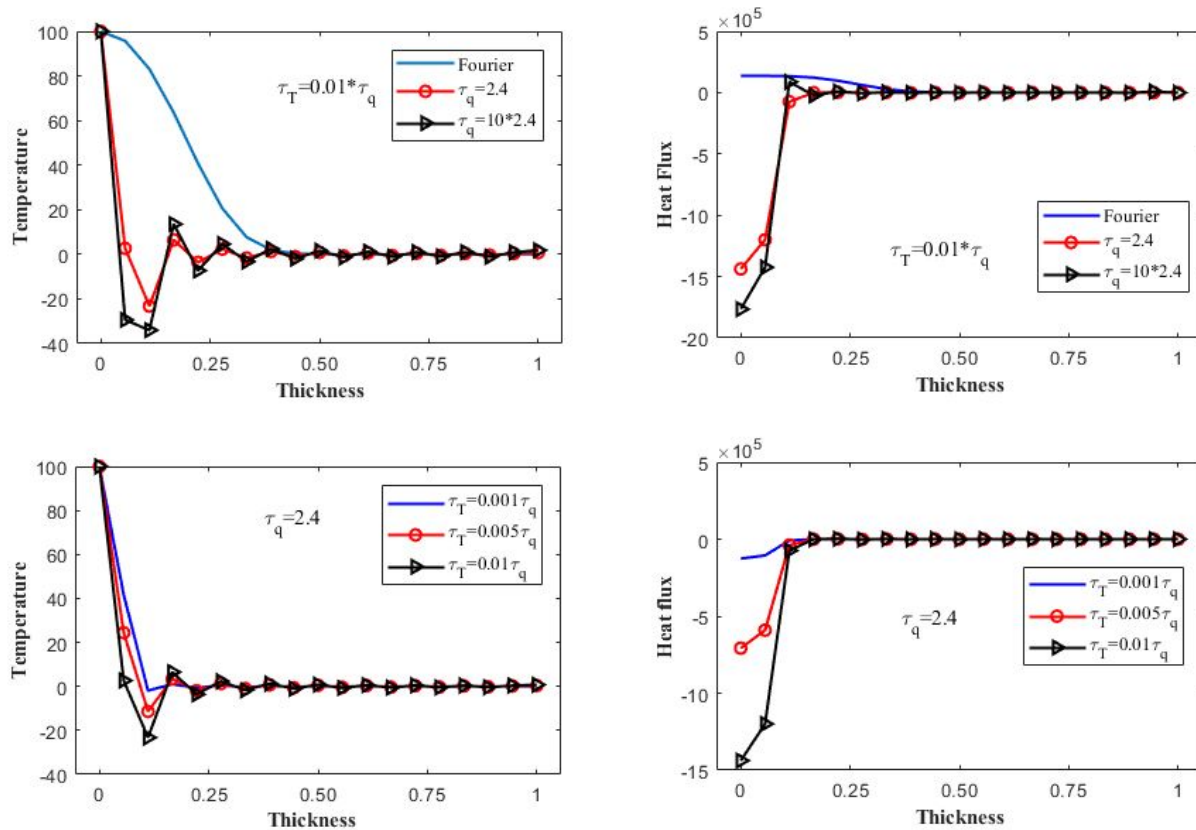


Figure 2.4 Effects of the phase lags of heat flux and temperature gradient on temperature and heat flux distribution

The distributions of the temperature and heat flux at $t=0.007$ are illustrated in Fig 2.4 . As is known, τ_q is the phase lag of the heat flux and τ_T is the phase lag of the temperature gradient. DPL theory states that the gradient of temperature at a point x and time $t + \tau_T$ corresponds to the heat flux vector at the same point and time $t + \tau_q$. So, the bigger the phase lag τ_T , the more difficult for temperature to catch up with the heat flux. As Fig 2.4 shows (while $\tau_q=2.4$), for higher τ_T , the thermal wave initiation occurs sooner and also a longer time duration is needed for temperature to get steady.

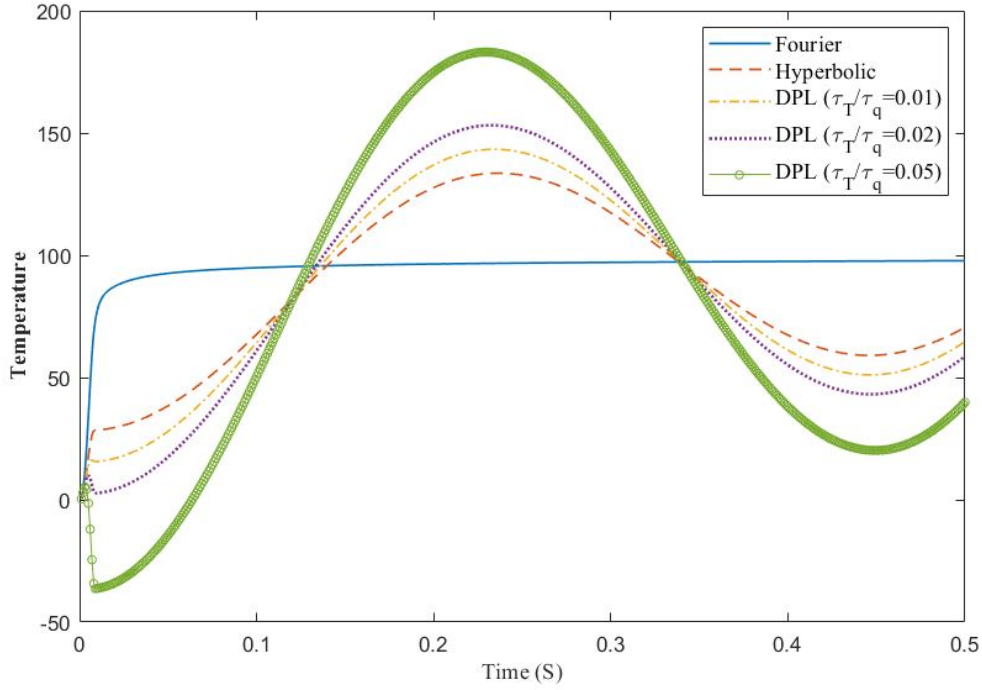


Figure 2. 5 Time evolution of the temperature (°C) at different temperature gradient and heat flux time lags

Figure 2.5 shows the temperature history at the second sample point ($Nx = 2$). Here, we consider $dt = 0.001$ and $N_x = N_t = N_{ts} = 13$, so x is equal to $\frac{2}{13} * \frac{-h}{2}$ ($h=0.001$ m) and there is a thermal shock at $t = 0$ and $x = -h/2$ like Eq. 2.11. For both DPL (when we have both time lags) and C-V (when we have one time lag (τ_T)) models, the temperature propagates through the medium with a finite speed, so a finite time is required for the medium to adapt itself to the prescribed boundary conditions. It is an interesting point to note that increasing the time lag τ_T while τ_q remaining constant rises the maximum transient temperature and the thermal wave speed. Also, Fig 2.5 shows that the thermal wave speed based on the DPL model is greater than that based on the C-V model due to the existence of time lag of temperature gradient, τ_T . This figure shows that by using C-V or DPL heat conduction, the slab experiences a temperature beyond the imposed boundary conditions in the absence of heat generation. This phenomenon is called

overshooting and will be enhanced by increasing the time lag, τ_T . Also, it should be noticed that for $\tau_T > 0.02 * \tau_q$, the results become unrealistic to some extent as negative values of temperature occur. The existence of negative values of temperature can be explained briefly here. As discussed earlier, hyperbolic and DPL heat conduction models involve two coupled equations: 1) heat conduction equation, 2) equation of energy conservation. It is the requirement of energy conservation that attributes to this incident. In the beginning, we have an abrupt temperature rise at the boundary, and the adjacent areas will need to provide the energy to support this change. The negative temperature regions are where energy loss occurs, while this lost energy was transferred to the adjacent areas to support the abrupt temperature rise. It should be noted that the negative heat flux in the beginning has not been observed in any experiment. It is possible to avoid getting the negative heat flux or temperature in the beginning by choosing a proper value of time delays or a right thickness of the specimen.

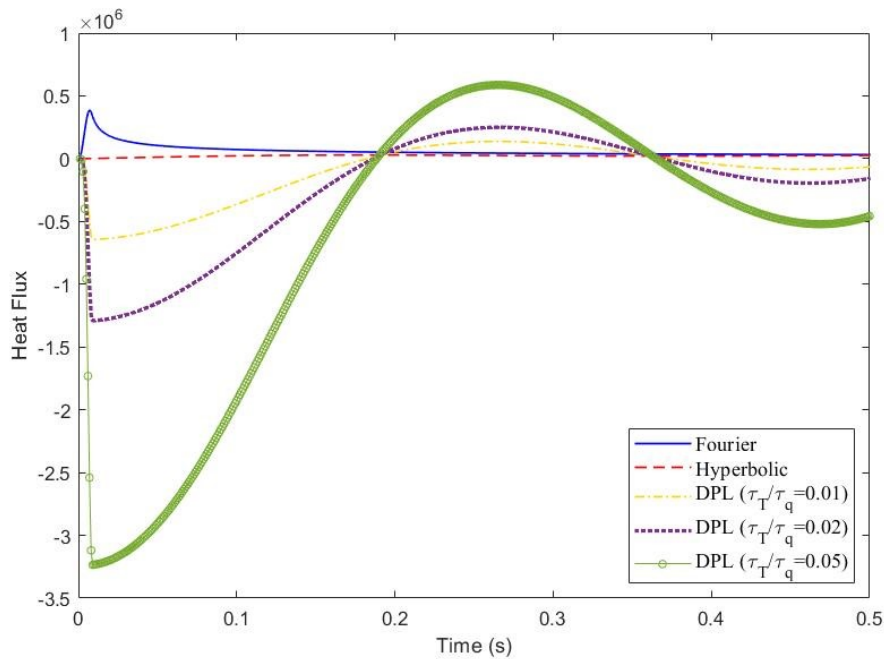


Figure 2. 6 Time evolution of the heat flux at different temperature gradient and heat flux time lags

The effects of the phase lag of temperature gradient, τ_T , on the heat flux distributions, while $\tau_q = 2.4$ s, in the thickness direction of the medium at $t = 0.003$ s are presented in Fig 2.6. The imposed thermal boundary condition on the one slap causes thermal wave initiation which travels toward the other side as a result of time delay. Also, as is shown in Fig 2.6, the DPL model would reduce to the C-V model when $\tau_T=0$ which means the temperature gradient is preceding the heat flux.

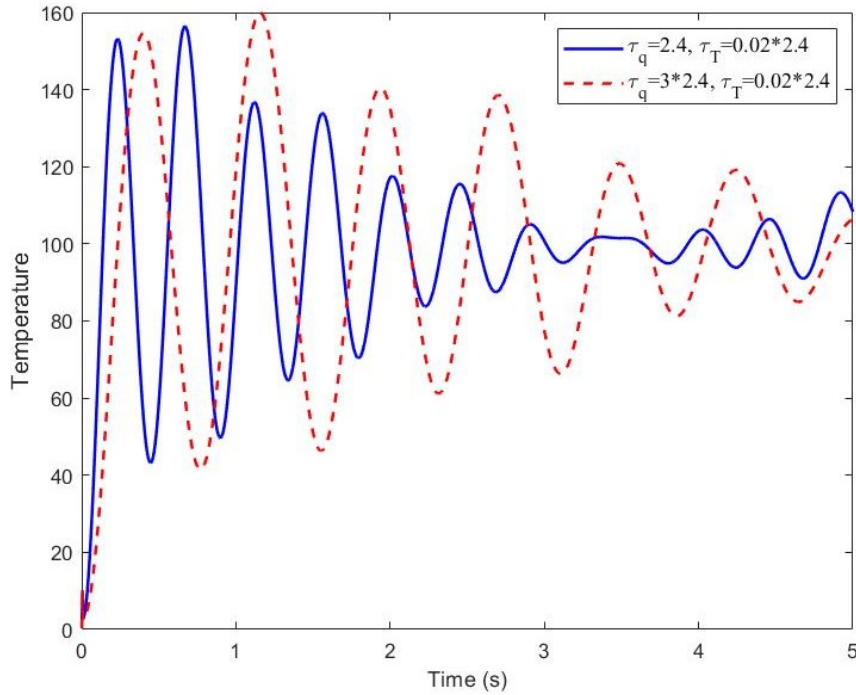


Figure 2. 7 Effects of heat flux time lag in temperature history in case of DPL heat conduction

Figure 2.7 illustrates the influence of τ_q on the time history of the temperature by exhibiting the results at point $N_x = 3$. When τ_T is kept unchanged, varying the value of τ_q can result in different characteristics of temperature distribution. As one can observe, increasing the time lag of heat flux, τ_q , lessens both the thermal wave speed and maximum transient temperature.

The lower speed of thermal waves leads to a later convergence of temperature.

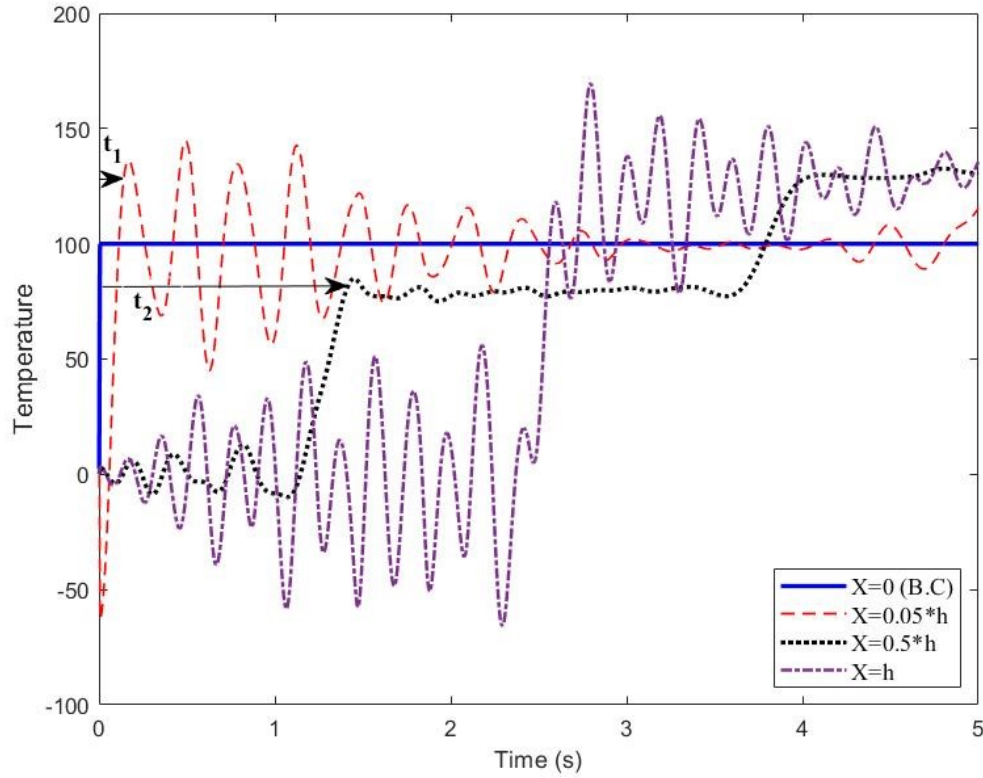


Figure 2. 8 Time evolution of the temperature at different points along the thickness of the beam in case of DPL heat conduction

Figure 2.8 depicts the time history of temperature at four distinct points ($x=0$, $x=0.05h$, $x=0.5h$, and $x=h$) when τ_T and τ_q are constant. Clearly, thermal wave needs more time to navigate from $x = 0$ to $x = 0.5h$, here this time is shown as t_2 . This is the time duration that an area in the middle of the medium ($N_x = 7$, N_x shows the number of nodes) needs to completely get affected by the imposed thermal boundary condition. Based on this figure, one can reach the point that temperature distribution is the expression of energy allocation, which is the consequence of heat flux. In the area close to the imposed thermal boundary condition ($N_x = 3$, N_x shows the number of nodes), stabilization occurs sooner due to the earlier infection (t_1). And

for $N_x = 7$, it takes more time for the temperature to get stabilized.

2.5 Conclusion

Temperature and heat flux propagation in a medium is investigated by adopting the dual-phase-lag heat conduction model. For the first time, differential quadrature approach is utilized to develop a solution. The method leads to the easier solution and is convenient to apply to different kind of boundary conditions or material properties, and even two or three-dimensional problems. The convergence of the solution method is investigated by comparing the results with available analytical solutions. It is shown that the negative temperature regions are where energy loss occurs, while this lost energy has been transferred to the adjacent areas to support the abrupt temperature rise. Moreover, it is shown that both time lags, τ_q and τ_t , play a vital role in the temperature and heat flux. An increase in the value of τ_T , leads to faster wave motion, and as a result, a later convergence. On the contrary, increasing the value of τ_q leads to slower wave motion, a lower peak value of transient temperature and shorter time duration for temperature to become stable. In general, the transient effect of heat conduction is shown to decay quickly, and both the Fourier and non-Fourier models will coincide with each other after the initial, transient period. It should be mentioned that the temperature overshoot phenomenon highly depends on the specimen size. As the specimen size increases, the local time-rate of temperature change dramatically decreases, resulting in a rapid diminution of the overshooting phenomenon. On the other hand, as the physical scale of a solid shrinks, especially if it shrinks to micro-scale or to the order of the mean free path of the phonons, individual behaviour of energy carriers becomes pronounced, and other parameters such as characteristic length would play an important role in the thermoelastic response. The effect of adding another phase to the system such as CNTs and shrinkage of the scale of the device is investigated in the next chapters.

Chapter 3:

Dual-phase-lag heat conduction in FG carbon nanotube reinforced polymer composites²

The numerical simulation of non-Fourier, dual-phase-lag (DPL) heat conduction in carbon nanotube (CNT) reinforced composites has been performed by developing the differential quadrature method (DQM) application. Although using the non-Fourier heat conduction has become popular, most of the simulations are conducted over simple geometries due to numerical restrictions. DQM copes with this problem easily even with complicated boundary conditions. The proposed method discretizes the time domain in the form of blocks. Each block contains several time levels, and each block needs to solve separately by using the output of one block as an initial condition of the next block. The effect of volume fraction of CNT on the temperature and heat flux profile is investigated, and all parameters are considered temperature dependent. To show the influence of time lag parameters, the Fourier, hyperbolic heat conduction and DPL heat conduction models were compared. Furthermore, various types of dynamic thermal loading have been examined to obtain the transient temperature distributions. We show the presence of heat wave in DPL heat conduction by considering the time lag parameter in the microstructural interactions of fast transient heat conduction. It is found that considering the mechanical properties of the CNTs

² A version of this chapter is published in journal of Physica B: Condensed Matter 564, 147-156, 2019.

dependent to the temperature is crucial to obtain accurate results.

3.1 Introduction

Polymers are widely used in industry because of their diverse functionality, lightweight, and excellent chemical stability. However, the low thermal conductivity is a major technological barrier in some applications such as heat exchangers and electronic packaging. Compositing is one of the best methods to modify the thermal conductivity of polymers by the incorporation of fillers with a high thermal conductivity such as carbon nanotubes (CNTs). Carbon nanotubes, with exceptional electronic and mechanical properties, was considered as a newly excellent candidate for reinforcement of composite materials [52-58]. Numerous studies have been made to analytically and experimentally determine the mechanical properties of CNT reinforced nanocomposites via molecular dynamics (MD) simulation [59,60], continuum mechanics [61,62] and multi-scale simulations [59,63]. The macro-mechanical properties of nanocomposites are affected by the microstructure and volume fraction of CNTs. Several methods are used to evaluate the effective properties of nanocomposites, including those based on single inclusion theory [64], such as Mori-Tanaka method [65], the self-consistent scheme [66], and differential method [67], among others. The Mori-Tanaka (MT) model as one of the best known analytical approaches to determine the effective material constants of composite materials is implemented in this research.

In one-dimensional steady-state heat flow, the material's thermal conductivity is a parameter that relates the rate of heat conduction to the temperature gradient of the bulk material, and it assumes that heat flux and temperature gradient generate at the same time instant. This means that heat disturbances, with parabolic-type heat conduction equation, need to spread at an infinite speed [2] as shown in Eq. (3.1).

$$q(x, t) = -k\nabla T(x, t) \quad (3.1)$$

where $\nabla T(x, t)$ is the temperature gradient which is a vector function of the position vector x and the time variable t , $q(x, t)$ is the heat flux, and k is the thermal conductivity. It can be used to solve most engineering problems at classical length and time scale, but cannot entirely model situations involving shallow temperatures near absolute zero, high-temperature gradient, and very high frequencies of heat flux [3,4,31-33,68-71]. Besides, because the heat flux and the temperature gradient are simultaneous, one can not differentiate between the cause and effect of heat flow which is critical for the transient behavior at an extremely short time, for example on the order of picoseconds to femtoseconds [5]. Also, in the absence of heat source, in the Fourier heat conduction, the temperature will be reached its maximum or minimum value at the boundary of the medium at the first instant. However, for the heat conduction models such as the Cattaneo and Vernotte (CV) and DPL models, the temperature of some inner regions in the medium may exceed the temperature at the boundary which is called the overshooting phenomenon. Evidently, this phenomenon may lead to the damage of electronic or mechanical devices if it is not appropriately handled [7]. So, the hyperbolic heat conduction equation is introduced based on the Cattaneo and Vernotte model (Eq. (3.2)) for the heat flux incorporates a relaxation mechanism in order to gradually adjust to a change in the temperature gradient [9,32,33]. This model has been a satisfactory extension of classical diffusion theory and can yield the hyperbolic diffusion equation within the continuum assumption.

$$q(x, t + \tau_q) = -k\nabla T(x, t) \quad (3.2)$$

where τ_q is the time lag of the heat flux. The temperature gradient always precedes the heat flux vector. A new time integration scheme was proposed by Fung [9, 72] based on the DQM and it was illustrated that the scheme is unconditionally stable. The differential quadrature time

integration scheme proposed by Fung [9,72] was assessed in Liu and Wang [73]. By using the same concept, Rahideh et al. [10] used the layerwise-incremental DQM to show the effect of heat wave speed on the thermal characteristics of a multi-layered domain made of functionally graded materials. Furthermore, multiphase systems are not following Fourier's law as well, such as in nanofluids, porous media, and biomaterials [11,37,38,74]. To tackle the deviations from Fourier's law, Tzou [11,12] introduced two-phase lags heat conduction, presenting the DPL model as:

$$q(x, t + \tau_q) = -k\nabla T(x, t + \tau_T) \quad (3.3)$$

where τ_T is the time lag of the temperature gradient. This model can capture the effect of heat conduction with high heat flux and short heating period. For example, Dai et al. [13] developed a new higher-order finite difference scheme for solving the DPL equation in nano heat conduction with the temperature jump boundary condition. Furthermore, if $\frac{\tau_q}{\tau_T} > 1$, Eq. (3.3) is hyperbolic and thermal waves will be produced in the heat conduction process. If, otherwise, $\frac{\tau_q}{\tau_T} \leq 1$, this equation is parabolic and thermal waves does not exist [14,39].

Wang and Zhou [40] established methods of measuring the time lags and obtained an analytical solution for the regular 1-D, 2-D and 3-D heat conduction domains under arbitrary initial and boundary conditions. A combination study of non-Fourier heat conduction with thermal phonon theory has also been performed [41]. Also, Basirat et al. [42] have reported values for phase lags corresponding to some metal films. Values of these parameters are mainly determined experimentally [41,42] and they ranged from 0.01 to 32 s. The effect of laser, as a heat source, on a thin film was studied by Noroozi et al. [45]. They have used the approximate-analytical Adomian Decomposition Method to solve the DPL equations. Wang et al. [26] presented a peridynamic non-Fourier heat conduction model, in the framework of generalized state-based peridynamics by introducing the concept of dual phase lags into the peridynamic framework, to consider the non-

Fourier and nonlocal effects simultaneously.

This study is a crucial research advancement in elucidating the processing-structure-property relationships of thermally conductive polymer composites and nanocomposites. The DPL model is of great importance in describing the transient heat conduction. To the authors' best knowledge, all published papers are suffering from the convenient way of implementing the boundary conditions or flexibility in using FGMs since using analytical, or semi-analytical solutions has lots of restrictions. In summary, the objective of this study is to introduce a new application of differential quadrature method [30,46] to resolve DPL heat conduction in nanocomposites with considering the nonlinear terms of heat conduction. This report is the first research on the effects of dual phase lag on nanocomposites via DQM. Using the DQM allows us to choose a relatively coarse grid and obtain a reasonable solution. Also, it is much easier to implement rather than solving heat conduction equations in the Laplace domain or other analytical methods. Finally, the DQM will give no restriction on the boundary conditions and material properties.

3.2 Carbon nanotubes: Thermal conductivity (K), relaxation time (τ) and heat capacity (C) of CNTs

Thermal conductivities of the random and aligned CNT reinforced composites are calculated as a function of the volume fraction of CNTs. Thermal conductivity is greatly improved as the volume fraction of CNTs increases in both random composites and aligned composites [75].

Second-order polynomial equations are used to obtain the thermal conductivity as follow:

$$K_R = 51.9V_{cn}^2 + 0.43V_{cn} + 0.64 \quad (3.4)$$

$$K_A = 90.9V_{cn}^2 + 4.35V_{cn} + 0.77 \quad (3.5)$$

where K_R and K_A refer to the thermal conductivities of randomly distributed CNTs and aligned

CNTs. Clearly, for a specific volume fraction of CNTs, K_A is higher than K_R , which leads to a faster motion of heatwaves in the media [76]. In order to approach reality, just the composite with a random distribution of CNTs is considered.

Table 3. 1 Time delays for SWCNT.

CNT length	τ (Time delay ns)
5 μm	12.353
10 μm	25.846
15 μm	61.283
20 μm	107.780

Since the relaxation time of CNTs shown in table 3.1 is extremely smaller than the relaxation time of the matrix, we have used CNT with length of 5 μm as an example. The length of CNTs does not play a key role in the heat conduction of nanocomposite based polymer since the relaxation time of the polymer is relatively high. The specific heat capacity (C_p) of a CNT as a function of temperature is stated in [76]. They showed that increasing temperature would increase the specific heat capacity C_p proportionally by approximately a constant amount as follows:

$$C = aT + b \quad (3.6)$$

with $a = 2.5642 \left(\frac{J}{kg*K} \right)$ and $b = -61.7294 \left(\frac{J}{kg*K} \right)$.

3.3 Composites reinforced with randomly oriented, straight CNTs

The effective properties of composites with randomly oriented non-clustered CNTs, such as shown in Fig 3.1, are studied in previously published papers of authors [77]. Following the standard Mori-Tanaka derivation, one can develop the expression for the effective composite stiffness, C .

$$C = C_m + f_r \langle (C_r - C_m) A_r \rangle (f_m I + f_r \langle A_r \rangle)^{-1} \quad (3.7)$$

where f_r and f_m are the fiber and matrix volume fractions, respectively, C_m is the stiffness tensor of the matrix material, C_r is the stiffness tensor of the equivalent fiber, I is the fourth-order identity tensor and A_r is the dilute strain-concentration tensor of the r th phase [78] for the fiber which is given as:

$$A_r = [I + S(C_m)^{-1}(C_r - C_m)]^{-1} \quad (3.8)$$

The tensor S is Eshelby's tensor, as given by Eshelby [64] and Mura [79]. The terms enclosed with angle brackets in Eq. (3.7) represent the average value of the term overall orientations defined by transformation from the local fiber coordinates $(o-x_1x_2x_3)$ to the global coordinates $(o-x_1x_2x_3)$ (Fig 3.1) with axis x_2 being the direction along the aligned nanotube. The elastic properties of the nanocomposite are determined from the average strain obtained in the representative volume element. The matrix is assumed to be elastic and isotropic, with Young's modulus E_m and Poisson's ratio ν_m . Each straight CNT is modeled as a long fiber with transversely isotropic elastic properties and has a stiffness matrix given by Eq. (3.7). Therefore, the composite is also transversely isotropic, with five independent elastic constants. The substitution of non-vanishing components of the Eshelby tensor S for a straight, long fiber along the x_2 -direction [78] in Eq. (3.8) gives the dilute mechanical strain concentration tensor. Then the substitution of Eq. (3.8) into Eq. (3.7) gives the tensor of effective elastic moduli of the composite reinforced by aligned, straight CNTs. In particular, the Hill's elastic moduli are found as [78].

$$k = \frac{E_m \{E_m f_m + 2k_r(1 + \nu_m)[1 + f_r(1 - 2\nu_m)]\}}{2(1 + \nu_m)[E_m(1 + f_r - 2\nu_m) + 2f_m k_r(1 - \nu_m - 2\nu_m^2)]} \quad (3.9)$$

$$l = \frac{E_m \{ \nu_m f_m [E_m + 2k_r(1 + \nu_m)] + 2f_r k_r (1 - \nu_m^2) \}}{(1 + \nu_m) [E_m (1 + f_r - 2\nu_m) + 2f_m k_r (1 - \nu_m - 2\nu_m^2)]} \quad (3.10)$$

$$n = \frac{E_m^2 f_m (1 + f_r - f_m \nu_m) + 2f_m f_r (k_r n_r - l_r^2) (1 + \nu_m)^2 (1 - 2\nu_m)}{(1 + \nu_m) [E_m (1 + f_r - 2\nu_m) + 2f_m k_r (1 - \nu_m - 2\nu_m^2)]} + \frac{E_m [2f_m^2 k_r (1 - \nu_m) + f_r n_r (1 + f_r - 2\nu_m) - 4f_m l_r \nu_m]}{E_m (1 + f_r - 2\nu_m) + 2f_m k_r (1 - \nu_m - 2\nu_m^2)} \quad (3.11)$$

$$p = \frac{E_m [E_m f_m + 2p_r (1 + \nu_m) (1 + f_r)]}{2(1 + \nu_m) [E_m (1 + f_r) + 2f_m p_r (1 + \nu_m)]} \quad (3.12)$$

$$m = \frac{E_m [E_m f_m + 2m_r (1 + \nu_m) (3 + f_r - 4\nu_m)]}{2(1 + \nu_m) \{ E_m [f_m + 4f_r (1 - \nu_m) + 2f_m m_r (3 - \nu_m - 4\nu_m^2)] \}} \quad (3.13)$$

where k , l , m , n and p are its plane-strain bulk modulus normal to the fiber direction, cross modulus, transverse shear modulus, axial modulus and axial shear modulus, respectively; k_r , l_r , m_r , n_r , and p_r are the Hill's elastic moduli for the reinforcing phase (CNTs); f_r and f_m are the volume fractions for carbon nanotube and matrix, related by

$$f_r + f_m = 1 \quad (3.14)$$

As mentioned before, the CNTs are transversely isotropic and have a stiffness matrix given below (Hill's elastic moduli)

$$C_r = \begin{bmatrix} n_r & l_r & l_r & 0 & 0 & 0 \\ l_r & k_r + m_r & k_r - m_r & 0 & 0 & 0 \\ l_r & k_r - m_r & k_r + m_r & 0 & 0 & 0 \\ 0 & 0 & 0 & p_r & 0 & 0 \\ 0 & 0 & 0 & 0 & m_r & 0 \\ 0 & 0 & 0 & 0 & 0 & p_r \end{bmatrix} \quad (3.15)$$

$$C_r = \begin{bmatrix} \frac{1}{E_L} & -\frac{\nu_{TL}}{E_T} & -\frac{\nu_{ZL}}{E_Z} & 0 & 0 & 0 \\ -\frac{\nu_{LT}}{E_L} & \frac{1}{E_T} & -\frac{\nu_{ZT}}{E_Z} & 0 & 0 & 0 \\ -\frac{\nu_{LZ}}{E_L} & -\frac{\nu_{TZ}}{E_T} & \frac{1}{E_Z} & 0 & 0 & 0 \\ 0 & 0 & 0 & \frac{1}{G_{TZ}} & 0 & 0 \\ 0 & 0 & 0 & 0 & \frac{1}{G_{ZL}} & 0 \\ 0 & 0 & 0 & 0 & 0 & \frac{1}{G_{LT}} \end{bmatrix}^{-1} \quad (3.16)$$

where $E_L, E_T, E_Z, G_{TZ}, G_{ZL}, G_{LT}, \nu_{LT}, \nu_{LT}, \nu_{LT}, \nu_{LT}, \nu_{LT}, \nu_{LT}$ are material properties of the reinforcing fiber.

Now, the effective properties of composites with randomly oriented, non-clustered CNTs, such as in Fig 3.1, can be obtained. The resulting effective properties for the randomly oriented, CNT composite are isotropic, despite the CNTs having transversely isotropic effective properties. The orientation of a straight CNT is characterized by two Euler angles α and β , as shown in Fig 3. 1. When CNTs are completely, randomly oriented in the matrix, the composite is then isotropic, and its bulk modulus k and shear modulus G are derived as [78]

$$k = k_m + \frac{f_r(\delta_r - 3K_m\alpha_r)}{3(f_m + f_r\alpha_r)} \quad (3.17)$$

$$G = G_m + \frac{f_r(\eta_r - 2G_m\beta_r)}{2(f_m + f_r\beta_r)}$$

where

$$\alpha_r = \frac{3(K_m + G_m) + k_r - l_r}{3(G_m + k_r)} \quad (3.18)$$

$$\beta_r = \frac{1}{5} \left\{ \frac{4G_m + 2k_r + l_r}{3(G_m + k_r)} + \frac{4G_m}{G_m + p_r} + \frac{2[G_m(3K_m + G_m) + G_m(3K_m + 7G_m)]}{G_m(3K_m + G_m) + m_r(3K_m + 7G_m)} \right\} \quad (3.19)$$

$$\delta_r = \frac{1}{3} \left[n_r + 2l_r + \frac{(2k_r + l_r)(3K_m + 2G_m - l_r)}{G_m + k_r} \right] \quad (3.22)$$

$$\eta_r = \frac{1}{5} \left[\frac{2}{3} (n_r - l_r) + \frac{8G_m p_r}{G_m + p_r} + \frac{8m_r G_m (3K_m + 4G_m)}{3K_m (m_r + G_m) + G_m (7m_r + G_m)} + \frac{2(k_r - l_r)(2G_m + l_r)}{3(G_m + k_r)} \right] \quad (3.23)$$

The effective Young's modulus E and Poisson's ratio ν of the composite are given by:

$$E = \frac{9KG}{3K + G} \quad (3.24)$$

$$\nu = \frac{3K - 2G}{6K + 2G} \quad (3.25)$$

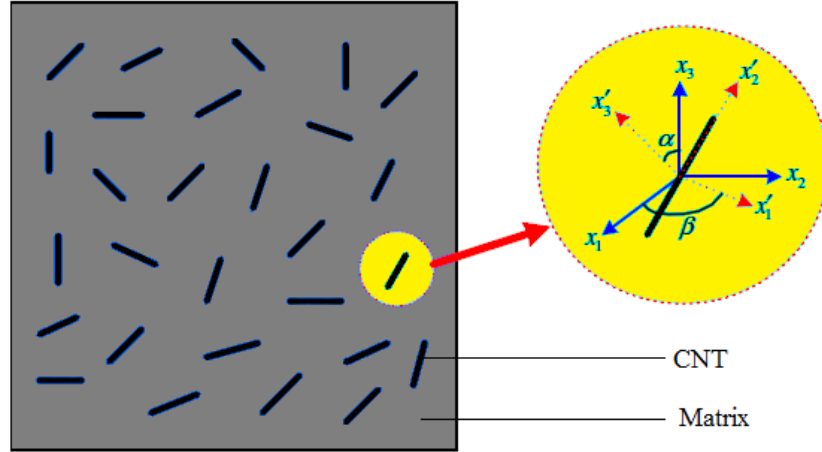


Figure 3. 1 Representative volume element (RVE) with randomly oriented, straight CNTs

In the present work, V_{cn} and V_m are considered as the CNT and matrix volume fractions, respectively. We assume for the FG medium, the volume fraction of the CNTs is given by the power-law-type function:

$$V_{cn}(z) = V_i + (V_o - V_i) \left(\frac{z}{h}\right)^q \quad (3.26)$$

where q is the volume fraction index, $0 \leq q \leq \infty$, h is the thicknesses of the medium, and V_o and V_i , which have values ranging from 0 to 1, denote the maximum and minimum volume fractions of CNTs that could exist in the thickness direction of the medium.

3.4 GDQ solution of governing equations

The generalized differential quadrature (GDQ) approach was developed by Shu and co-researchers based on the differential quadrature technique [46]. In GDQ method the p th order partial derivative of a continuous function $f(x, t)$ with respect to x at a given point x^i can be approximated as a linear summation of weighted function values at all of the discrete points in the domain of x , i.e.

$$\frac{\partial f^p(x, t_j)}{\partial x^p} \Big|_{x=x_i} = \sum_{k=1}^N C_{ik}^p f(x_{ik}, t_j), \quad (3.27)$$

$$(i = 1, 2, \dots, N_x, j = 1, 2, \dots, N_t, p = 1, 2, \dots, N_x - 1)$$

$$\frac{\partial f^p(x, t_j)}{\partial t^p} \Big|_{t=t_i} = \sum_{k=1}^N D_{jk}^p f(x_{ik}, t_j), \quad (3.28)$$

$$(i = 1, 2, \dots, N_x, j = 1, 2, \dots, N_t, p = 1, 2, \dots, N_x - 1)$$

where N_x and N_t are the number of sampling points along x and t directions respectively, also C_{ik}^p and D_{jk}^p are the x_i and t_j dependent weight coefficients. Details of this procedure can be found in the literature [80,81]. In this work, the Chebyshev-Gauss-Lobatto quadrature points are used [30],

$$x_i = \frac{1}{2} \left(1 - \cos \left(\frac{i-1}{N-1} \pi \right) \right), i = 1, 2, \dots, N \quad (3.29)$$

3.5 Dual-phase-lag heat conduction

The hyperbolic constitutive relation governing the transient heat transfer is as follows

$$q + \tau_q \frac{\partial q_x}{\partial t} = -k \left(\frac{\partial T}{\partial x} + \tau_T \frac{\partial^2 T}{\partial x \partial t} \right) \quad (3.30)$$

where τ_q and τ_T are introduced to account for the effects of thermal inertia and microstructural interaction such as electron phonon interaction or phonon scattering, respectively. Moreover, the energy equation can be written as,

$$\rho C \frac{\partial T}{\partial t} + \frac{\partial q}{\partial x} = g(x, t) \quad (3.31)$$

The DQM is used to discretize the spatial derivatives, and the incremental DQM is employed to discretize the temporal domain. Based on this approach, the total temporal domain is divided into a set of time intervals where the DQ rule is employed to discretize the temporal derivatives. The DQ method being applied to Eqs. (3.11,3.12), the following equations at an arbitrary sampling point x_i and t_j are then obtained:

$$k_{ij} \left(\tau_{ij} \sum_{m=1}^{N_x} C_{im}^1 T_{mj} \sum_{n=1}^{N_t} D_{in}^1 T_{in} \right) + k_{ij} \left(\sum_{m=1}^{N_x} C_{im}^1 T_{mj} \right) + \tau_{ij} \left(\sum_{n=1}^{N_t} D_{jn}^1 q_{in} \right) + q_{ij} = 0 \quad (3.32)$$

$$\left(\sum_{m=1}^{N_x} C_{im}^1 q_{mj} \right) + \rho_{ij} C_{ij} \left(\sum_{n=1}^{N_t} D_{jn}^1 T_{in} \right) = g_{ij} \quad (3.33)$$

Here, the proposed method marches in the time direction block by block [42]. In each block, there are several sub-domains ($n = 1:N_{ts}$) as it is shown in Fig 3.2, and the numerical results at these time levels are obtained simultaneously. Through this way, the numerical solution

at the $(n+1)$ th time level depends on the solutions at its previous levels since the output of each block is considered as an initial condition of the next block.

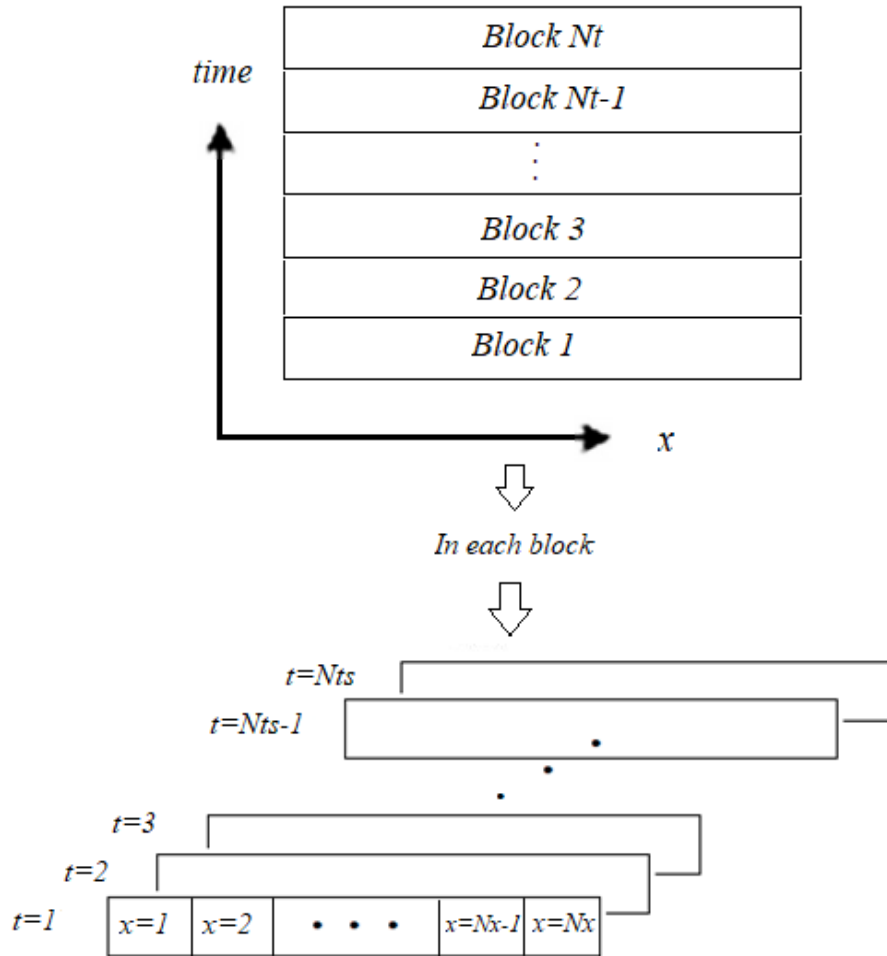


Figure 3. 2 Configuration of block-marching technique and mesh point distribution in each block

Figure 3.2 shows how the DPL heat conduction equation has been solved by using DQM. To solve these nonlinear equations, an iterative procedure should be used. For this purpose, in the first step, the nonlinear terms are neglected, and the resulting problem is solved. In the second step, the obtained temperature should be considered as a first guess of the nonlinear term in Eq (3.13). Then, the problems are solved again to obtain the new temperature and heat flux. Step 2 is repeated

until the discrepancy between the temperature from the two consecutive iterations is within $0.1 * 10^{-3}$. In the third step, the temperature and the heat flux obtained in the second step are used as the initial condition for the next time interval.

Let us consider a medium as shown in Fig 3.3 under a sudden temperature change on the left slab. The boundary conditions of the problem can be expressed as [49,50].

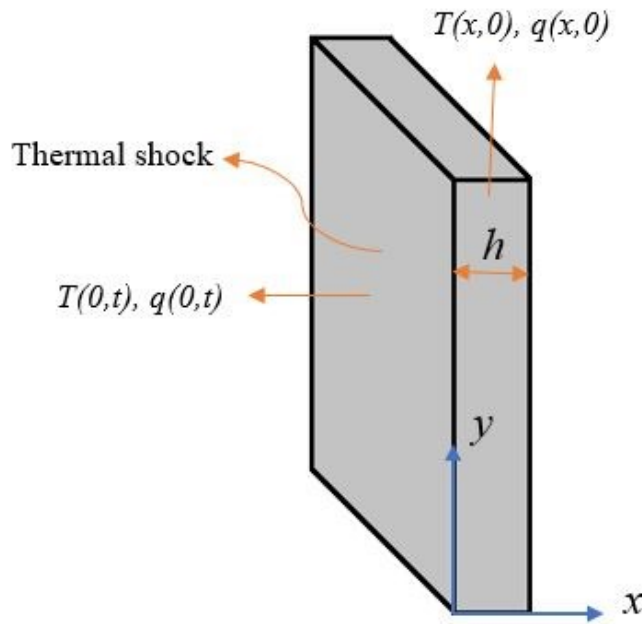


Figure 3. 3 One-dimensional heat conduction through a slab

$$T(x_i, t) = \begin{cases} \frac{1}{2} + \frac{3}{4} \left(\frac{2t}{t^* - 1} \right) - \frac{1}{4} \left(\frac{2t}{t^*} - 1 \right)^3 & \text{if } 0 \leq t \leq t^* \\ 1 & \text{if } t \geq t^* \end{cases} \quad (3.34)$$

$$T(x, 0) = 0$$

$$q(0, t) = 0$$

$$q(x, 0) = 0$$

Next, let us consider heating pulse applied to the left boundary of a parallel sided slab. The initial and boundary conditions are

$$\begin{aligned}
q(x_i, t) &= \begin{cases} -1 + \left(\frac{2t}{t^*} + 1\right)^{\frac{2}{3}} & \text{if } 0 \leq t \leq t^* \\ 0 & \text{if } t \geq t^* \end{cases} \\
q(x, 0) &= 0 \\
q(0, t) &= 0 \\
T(x, 0) &= 0
\end{aligned} \tag{3.35}$$

These boundary conditions are taking the place of the first or last sampling point in the discretized form of the governing equation. For example, $T(x_i, t)$ shows the temperature at the first sampling point in the physical domain at any time. Thus, all T_{ij} in which i is equal to 1 (T_{1j}) should be replaced by $T(x_i, t)$ which is already given at the boundary.

In all calculations, the following values are considered for heat conduction unless it is otherwise mentioned.

For polymer: $\rho^p = 1188$, $t_q^p = 2.4$, $C_p^p = 550$, $K^p = 0.243$

For CNT: $\rho^{cn} = 1400$, $t_q^{cn} = 12 * 10^{-12}$, $C_p^{cn} = 2.5642T - 61.7294$, $K^{cn} = 51.9 * V^{cn} + 0.43 * V^{cn} + 0.64$

Also, the value of temperature gradient time lag is considered as a ratio of heat conduction time lag like $t_T^{cn} = 0.02t_q^{cn}$ and $t_T^p = 0.02t_q^p$ and the thickness of the medium is $h = 0.001m$.

The effective thermal conductivity of nanocomposites is a function of the intrinsic thermal conductivity of the constituents, loading fraction, filler shape and size and filler dispersion. These parameters make it difficult to predict the thermal transport properties in the composites. Figure 3.4 shows the dependency of the heat flux and temperature gradient time lags and also illustrates that the volume fraction of CNTs largely governs thermal conductivity. The variation of the volume fraction of CNTs is linear ($p=1$), and number of sample points in the thickness direction (N_x) is equal to 13. This means $N_x=1$ and $N_x=13$ are equivalent to $x=0$ and $x=h$, respectively. Increasing the volume fraction of the CNTs leads to a higher thermal conductivity of

nanocomposite because of a higher thermal conductivity of CNTs than polymers. So, increasing the volume fraction of CNTs in the thickness direction increases the thermal conductivity of nanocomposite as we navigate through the thickness. On the other hand, a relatively low time lag of CNTs in comparison to polymer reduces the time lag of the nanocomposite. The effects of these variations are shown in Fig. 3.6.

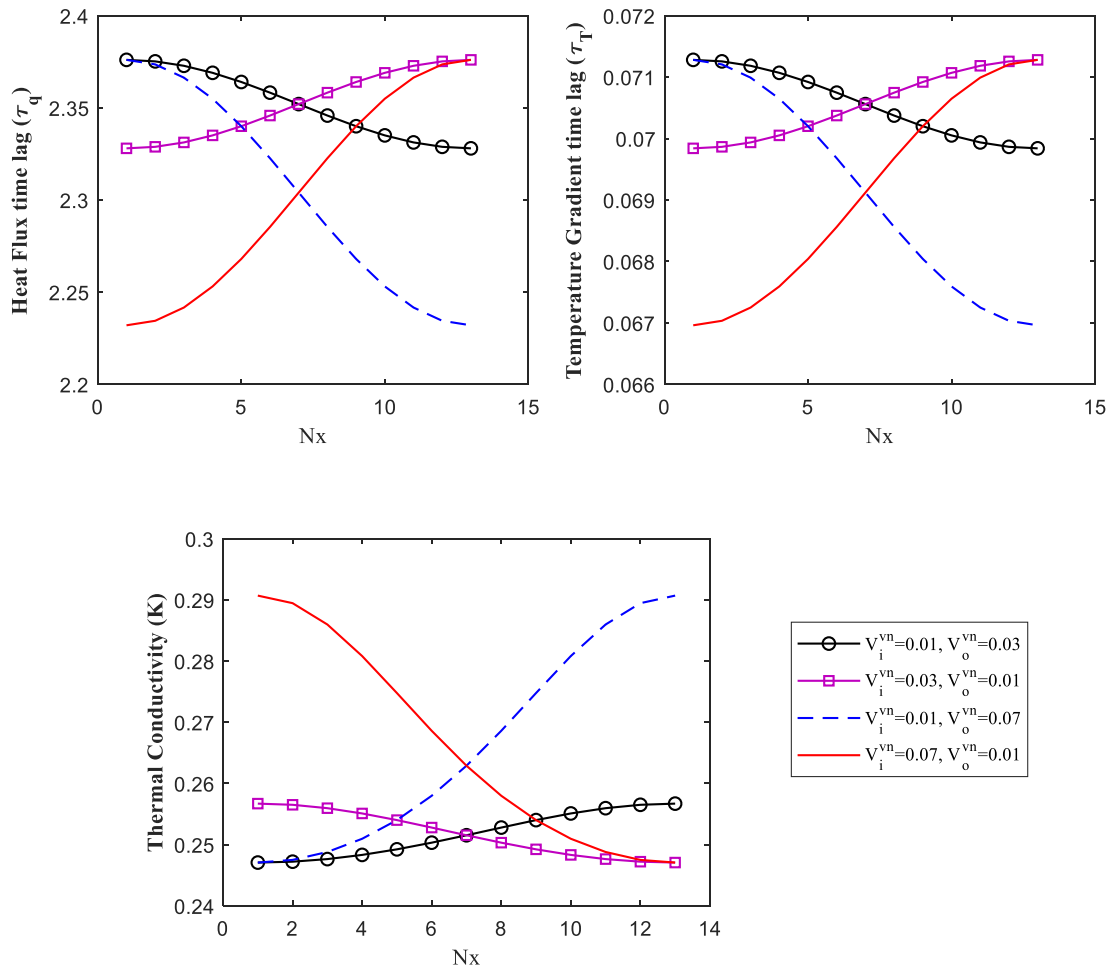


Figure 3. 4 Variation of the time lags and thermal conductivity through the thickness of the nanocomposite

As we mentioned earlier, t^* shows the time duration of the implementation of the thermal load. Thus, small values of t^* indicate the presence of thermal load for a short period of time known as a thermal shock, and higher values of the t^* indicate presence of the thermal load for a longer

duration of time. Fig. 3.5 shows the effects of increasing the time duration of the prescribed thermal load on the resultant temperature and heat flux in the media. By definition, as t^* increases, the thermal shock will be phased out, and we have a smooth rise in temperature in the boundary. It is evident from this figure that for the mild increase of temperature in boundary ($t^* = 5\text{s}$ and 15s), the results are getting close to the Fourier heat conduction. Thus, in case of having thermal shock for long time duration ($t^* = 15\text{s}$), the temperature may not exceed the temperature of boundary in the absence of heat generation, and there would be no sign of the thermal wave. Finally, the thermal shock with shortest time duration (t^*) has the highest peak of transient temperature and faster thermal wave motion which results in a long time to approach equilibrium.

As we expected, heat transfer takes place in waveform with finite speed of propagation of heat signals. Figure 3.6 manifests that aggregation of more CNTs close to the affected boundary condition (V_i) leads to faster thermal wave motion and higher peak of transient temperature. We considered $dt = 0.001$ and $Nx = Nt = Nts = 13$, here, $N_x = 3$ so $x = 0.23h$ and there is a thermal shock at $t=0$ and $x = -\frac{h}{2}$ like Eq. 3.30. Based on Fig. 3.4, in the case of $V_i^{cn} = 0.07$ and $V_o^{cn} = 0.01$, thermal conductivity has the maximum value and time lags are minimum at the beginning. So, the imposed thermal shock has the maximum possible effect. On the contrary, when $V_i^{cn} = 0.01$ and $V_o^{cn} = 0.07$, the effects of thermal shock on the boundary are prohibited by the low thermal conductivity of nanocomposite in the area close to the boundary ($x = -\frac{h}{2}$).

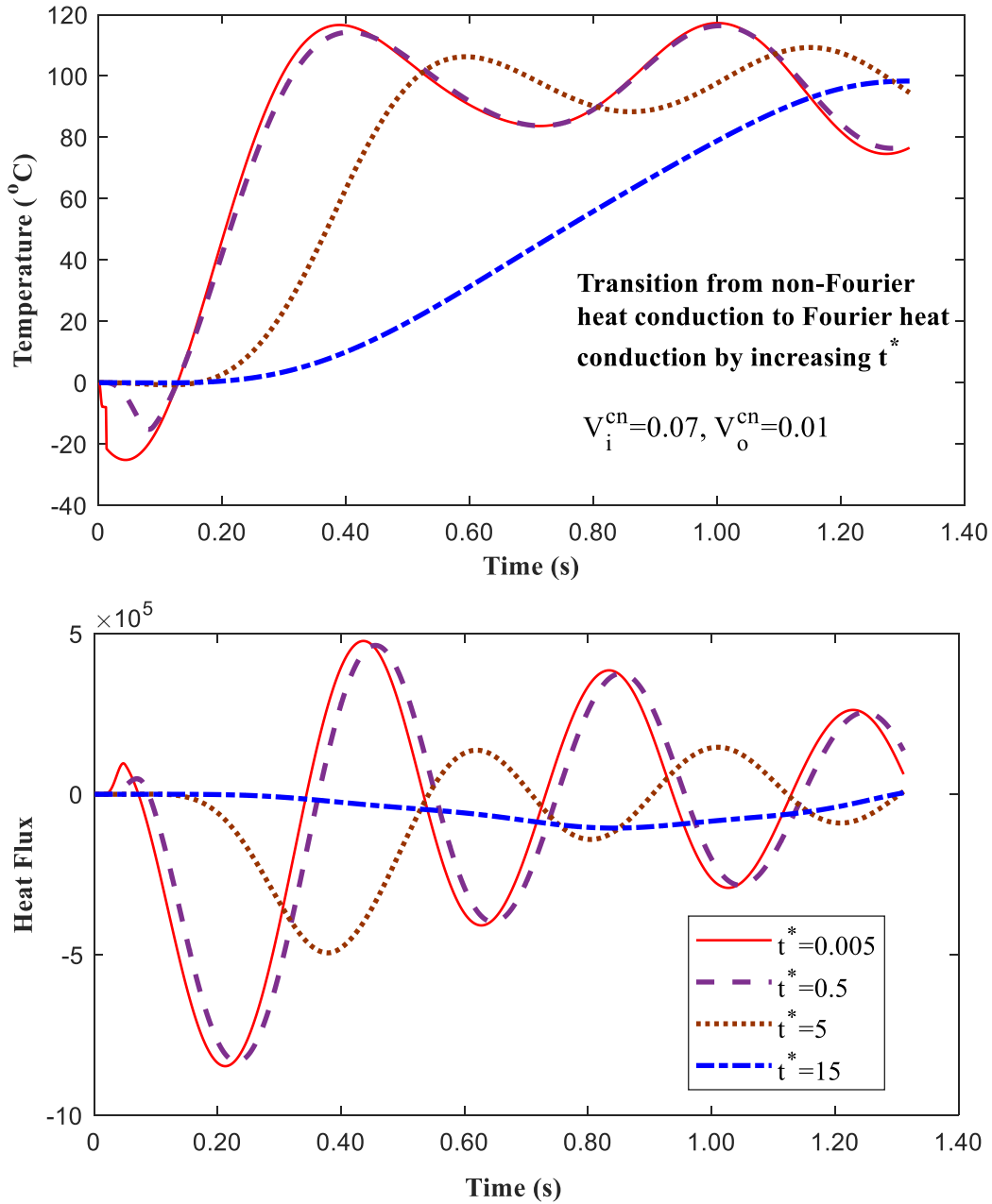


Figure 3. 5 Transition from non-Fourier heat conduction to Fourier heat conduction by changing the time duration of thermal shock on boundary condition at $x=0.23h$

Also, the plots for uniform distribution of CNT, $V_i^{cn} = V_o^{cn} = 0.01$ and FG type $V_i^{cn} = 0.01$ and $V_o^{cn} = 0.07$ almost coincides with each other which proves the dominance of thermal

conductivity in the area close to the boundary under thermal impulse. On the other hand, the content of CNTs, far away from the thermal shock does not play an important role.

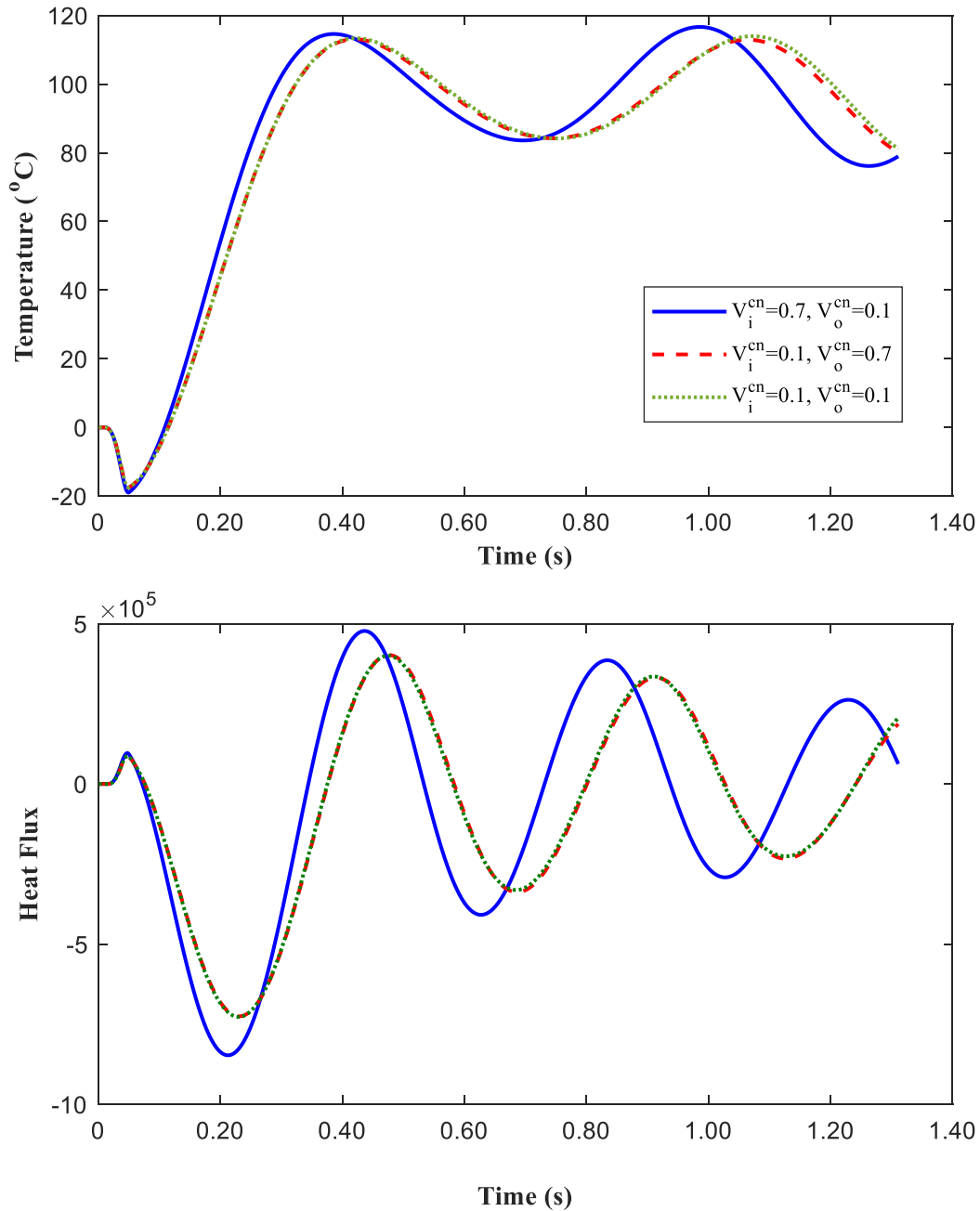


Figure 3. 6 Temperature and heat flux history in different volume fraction of CNT at $x=0.23h$

Figure 3.7 depicts the time history of temperature at boundaries, and three distinct points within the medium while τ_T and τ_q are constant. It takes more time for the temperature to navigate through the thickness, for example, t^* is the time that the outer boundary needs to be entirely influenced by the imposed boundary condition. Based on this figure, the temperature distribution indicates the energy allocation, which is the consequence of heat flux. In the area close to the imposed boundary condition ($N_x = 2$), stabilization occurs sooner due to the earlier thermal distribution. Moreover, for $N_x = 8$, it takes more time for the temperature to get stable with the lower peak value.

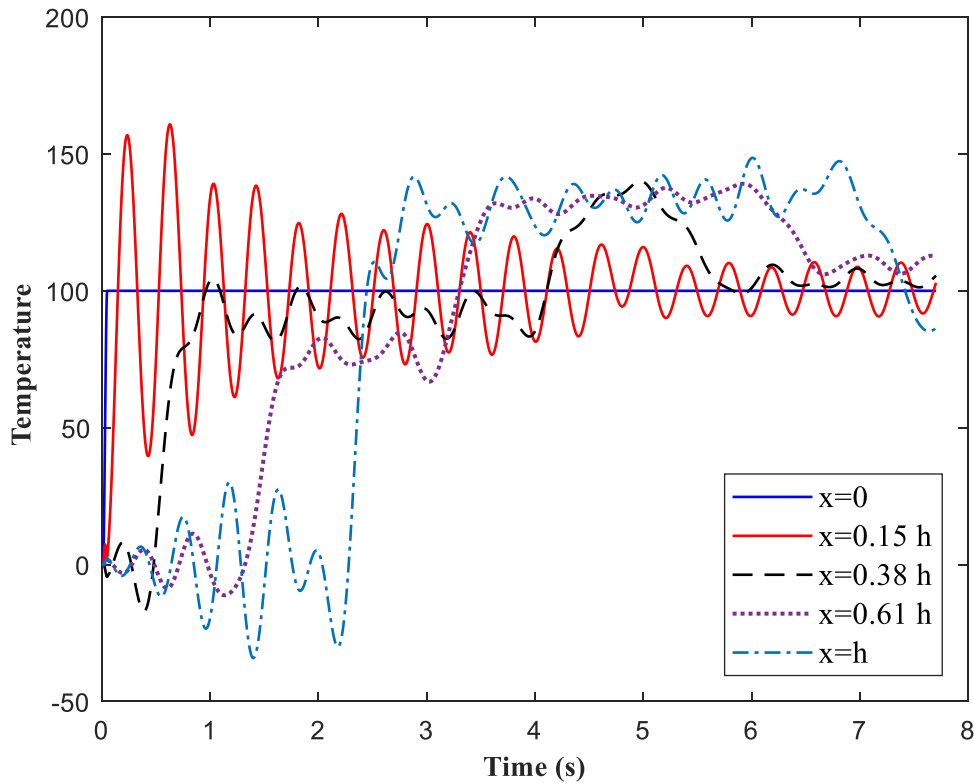


Figure 3. 7 Temperature history at different locations of the thickness of the medium

The distributions of temperature at $t=0.045$ are illustrated in Fig. 3.8. The DPL theory states that the gradient of temperature at a point x in the material at time $t + \tau_T$ corresponds to the heat flux vector at the same point and time $t + \tau_q$. So, the bigger the phase lag τ_T , the harder to

catch up with the heat flux. As Fig 3.8 shows, for higher τ_T , the thermal wave initiation occurs sooner and a longer time duration is needed for temperature to get steady. On the other hand, the higher τ_q forces the pace of convergences in heat conduction based on the DPL model due to the later initiation of the thermal wave.

Figure 3.9 shows the temperature history at the third sample point ($N_x = 3$). Here, we considered $dt = 0.001$ and $N_x = N_t = N_{ts} = 13$, so $x = 0.24h$ and there is a thermal shock at $t=0$ and $x=-h/2$ like Eq. 3.30. For both the DPL and C-V models, the temperature propagates through the medium with a finite speed, so a finite time is required for the medium to adapt itself to the prescribed boundary conditions. It is interesting that increasing the time lag τ_T while τ_q is constant, raises the maximum transient temperature. This figure shows that by using the hyperbolic or DPL heat conduction, the slab will experience a temperature beyond the imposed boundary conditions in the absence of heat generation. This phenomenon is called overshooting, and it will be enhanced by increasing the time lag, τ_T . Finally, for higher τ_T , a longer time duration is needed for temperature to get steady. The DPL model would reduce to the C-V model when $\tau_T=0$ which means the temperature gradient is preceding the heat flux.

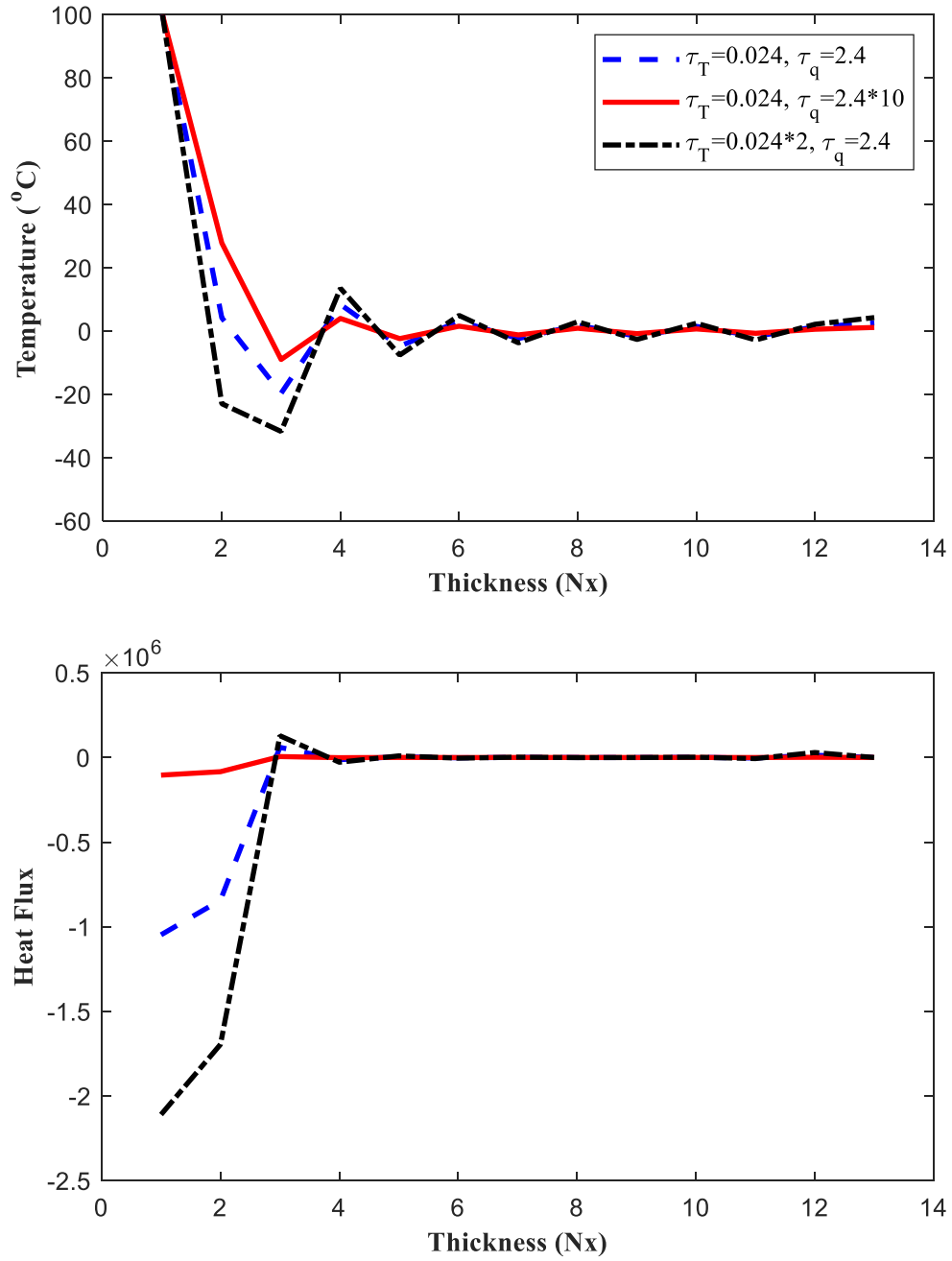


Figure 3. 8 Time evolution of the heat flux at different points along the thickness of the medium ($V_i = 0.07, V_o = 0.01$)

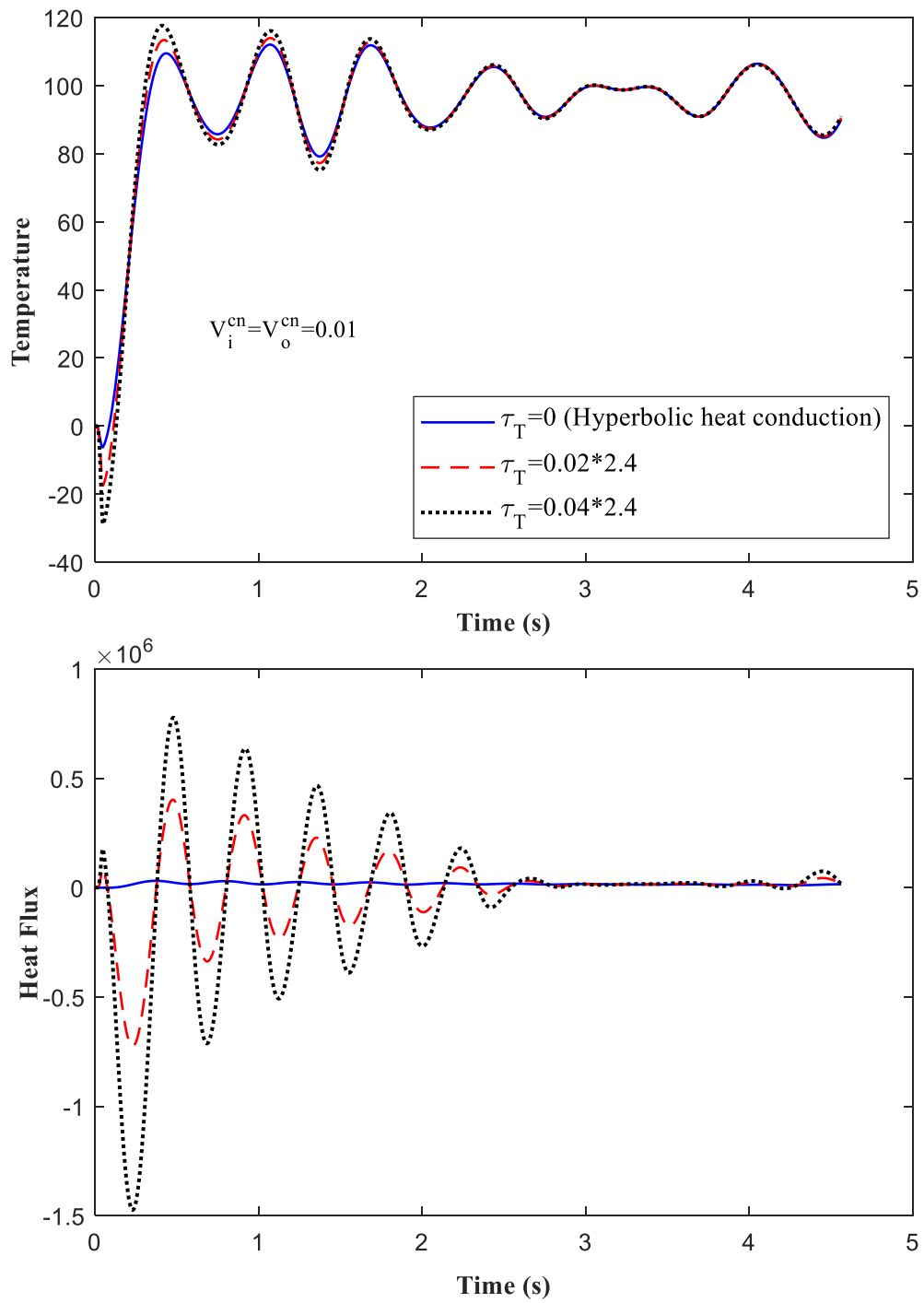


Figure 3. 9 Time evolution of the temperature at different points along the thickness of the medium at $x=0.23h$

3.6 Conclusion

We have studied the behavior of the dual-phase-lag (DPL) heat transfer model inside functionally graded carbon nanotube reinforced composite structures. All material properties are considered temperature-dependent. The differential quadrature (DQ) approach is utilized to develop a new solution led to the more straightforward solution, convenient way to apply different boundary conditions or changing the material properties, also an even simple way of expanding the problem to the two or three-dimensional problems. It is proved that the presence of CNTs, close to the prescribed boundaries, acts as a trigger and increases the peak of transient temperature while increasing the CNT volume fraction away from the imposed boundary heat impulse does not play an important role on the temperature and heat flux profiles. Moreover, it is shown that both time lags, τ_q and τ_t , play a vital role in the temperature and heat flux. The increase of τ_T , leads to fast wave motion and as a result later convergence. On the contrary, increasing τ_q leads to a slow wave motion, low peak values of transient temperature and short time duration before stable state is reached. The wave-like motion establishes as a result of lattice vibration, unlike the collision of the free electrons which is diffusive. In the diffusive transport, the characteristic length is greater than the mean free path (average distance traveled by energy carriers); and the energy transport is a macroscopic process. On the other hand, when the mean free path is greater than the characteristic length, the energy transport is said to be microscopic and will be investigated in the next chapter.

Chapter 4:

Nonlocal thermoelasticity: nonlocal heat conduction in nanostructures by new application of DQM³

This paper explores how reinforcing the hyperbolic heat conduction by the nonlocality affects temperature distribution in nanostructures such as nanobeam and single-walled carbon nanotubes (SWCNTs). The work dissects the nonlocal heat conduction by advocating a thoroughly new application of the differential quadrature method (DQM). The nanobeam is modelled as a cylindrical shell like a single-walled carbon nanotube (SWCNT), and the boundaries on the inner and outer sides are considered under a temperature-jump at the nanoscale. The effects of several parameters on the temperature distribution through the thickness of the nanobeam are highlighted, including time-dependent boundary conditions, time lag, nonlocal parameter, length and radius of the hollow beam.

4.1 Introduction

Over the last decade, nanostructures have attracted much interest due to their astounding characteristics that influence electrical, physical, chemical, optoelectrical, and biological properties. Carbon nanotubes (CNTs), one of the most popular carbon-based devices, have been investigated thoroughly over the past several decades for their potential applications including

³ A version of this chapter is submitted in journal of thermal stresses.

field-effect transistors (FETs), interconnects, electron field emitters, sensors, and energy storage and energy conversion devices [82-85]. Although the thermal conductivity of polymer matrix reinforced by CNTs improves when CNTs are randomly distributed, due to their large aspect ratio and the strong Van der Waals force between the CNTs and the medium, they tend to aggregate and form clusters in the nano-composite [86,87].

Many studies about CNTs and nanoscale structures were based on the classical continuum theory, which ignores the size effect. To tackle this problem, nonlocal elasticity theories were introduced for the nanoscale structures to develop size-dependent relations [88-91]. These approaches have shown superior performance in coping with this problem than any other approaches. Furthermore, there has been lots of research on the heat conduction of nanostructures theoretically [92,93] and experimentally [94,95].

In the classical model, the temperature gradient causes heat flux at the same point. At the nanoscale, a sufficient number of collisions among energy carriers are required for heat transport to take place [20,96]. In general, quantifying the value of a physical property at one point through another physical property in a region near that point is considered as the nonlocal effect in the continuum theory and has been observed experimentally [21].

Based on the investigations of Sobolev [22] and Tzou [12], since the heat flux at micro/nano scale is substantially nonlocal, classical models should be modified by introducing the characteristic length of the material. Prior research generally confirms that at the nanoscale, heat transfer is quite different from that estimated by classical laws. To tackle this problem, Guyer and Krumhansl (GK) [24, 25] introduced a generalized model by considering the characteristic length of the material as follows:

$$q(z, t + \tau_q) = -k\nabla T(z, t) + l^2\nabla^2 q(z, t) \quad (4.1)$$

where τ_q and l are the time lag of heat flux and internal characteristic length, respectively. To investigate the transient heat conduction from nano- to macro-scales, Wang et al. [27] considered the effects of both non-Fourier heat conduction and the nonlocality of the problem simultaneously. Xu [27] investigated the nanoscale heat conduction in silicon thin films by considering the temporally and spatially nonlocal effects. They showed thermal wave propagation in nanoscale materials.

Employing the DQM to solve the transient or time-dependent problems is a challenging problem in solid mechanics. There have been a few reports of implementing DQM to discretize the spatial domain and one of them employing finite difference, using the Runge Kutta or Newton-Raphson method, to discretize the temporal domain [97, 98]. Instability is the most crucial drawback of this method [99]. There have been a few reports of discretization of the temporal domain using DQM and block marching [100,101,33-35]. Pourasghar and Chen [37,47] introduced a new application for differential quadrature method (DQM) to solve the hyperbolic and dual-phase-lag heat conduction. They discretized the spatial and temporal domain by DQM. Finally, they implemented the Newton-Raphson method to obtain the temperature history along with temperature distribution through the thickness of the material.

A novel contribution of this study is to propose a new approach to accommodate both the temperature nonlocality and phase lagging, by modifying the non-Fourier heat conduction introduced in [26], and solving the problem by DQM [30, 39]. Using the DQM allows us to convert the partial differential equations to the ordinary differential equations. It also allows us to discretize the equations in both temporal and spatial directions. Finally, by applying the Newton-Raphson method to the discretized equations, the temperature and heat flux history will be obtained.

4.2 Nonlocal heat conduction

Cattaneo [7] and Vernotte [8] proposed the classical thermal wave model, in which the increase of the heat flux vector is considered due to the phonon collision in a duration of the relaxation time (τ_q):

$$q + \tau_q \frac{\partial q}{\partial t} = -k \nabla T. \quad (4.2)$$

where q is heat flux vector, t is time, k is thermal conductivity, T is temperature, ∇ is gradient operator. In nanostructures, the average distance travelled by energy carriers such as electrons and phonons comes to reflect the size-effect. The following equation shows the participation of the energy carriers into the heat conduction relation by l :

$$[1 - (l)^2 \nabla^2] q = -k \frac{\partial T}{\partial z} \quad (4.3)$$

where z is the thickness direction as shown in Fig 4.1 and l is the mean free paths of phonons, which makes the temperature at one specific point a function of the temperature of all points in the body. As mentioned earlier, the modified form of the non-Fourier heat conduction is used [26]:

$$\left[1 - l^2 \nabla^2 + \tau_q \frac{\partial}{\partial t}\right] q = -k \frac{\partial T}{\partial z} \quad (4.4)$$

where τ_q reflects the effects of thermal inertia.

4.3 Nonlocal heat conduction analysis of carbon nanotubes (CNTs)

Fourier and non-Fourier heat conduction models, such as hyperbolic and dual-phase-lagging heat conduction, do not accommodate the size effect, while the GK model reflects both the nonlocal and phase lagging effects [25,26, 102]:

$$q + \tau_q \frac{\partial q_z}{\partial t} = -k \frac{\partial T}{\partial z} + l^2 \left(\frac{\partial^2 T}{\partial z^2} \right) \quad (4.5)$$

Furthermore, from the first law of thermodynamics, the conservation of energy takes the

following form:

$$C_p \frac{\partial T}{\partial t} + \frac{\partial q}{\partial z} = g(z, t) \quad (4.6)$$

with C_p being the volumetric heat capacity, $C_p = \rho c$.

Let us consider a SWCNT, as shown in Fig 4.1, which is subjected to a heat shock at the inner or outer surfaces. A SWCNT modelled as a Timoshenko nanobeam with radius r , length L , and effective tube thickness h .

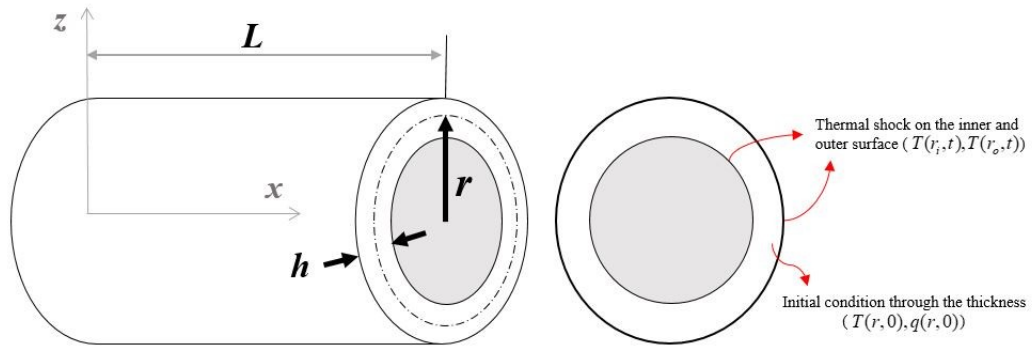


Figure 4. 1 Single wall carbon nanotube (SWCNT) modeled as a nonlocal Timoshenko nanobeam

The temperature fields in the above equations can be obtained from nonlocal heat conduction and energy equation as follows:

$$q + \tau_q \frac{\partial q_z}{\partial t} = -k \frac{\partial T}{\partial z} + l^2 \frac{\partial^2 T}{\partial z^2} \quad (4.7)$$

$$\rho C \frac{\partial T}{\partial t} + \frac{\partial q}{\partial z} = g(z, t) \quad (4.8)$$

where $g(z, t)$ is the heat source, which is taken to be zero in this paper.

For the thermal boundary conditions, it is assumed that the CNT is under a sudden temperature change on the outer surface ($r_o = r + \frac{h}{2}$) and all other boundaries are considered adiabatic. The initial and boundary conditions of the beam can be expressed as [49,50]:

$$\begin{aligned}
T(z, t) &= \beta(t) \\
T(z, 0) &= 0 \\
q(0, t) &= 0 \\
q(z, 0) &= 0,
\end{aligned} \tag{4.9}$$

$$\text{in which } \beta(t) = \begin{cases} \frac{1}{2} + \frac{3}{4} \left(\frac{2t}{t^* - 1} \right) - \frac{1}{4} \left(\frac{2t}{t^*} - 1 \right)^3 & \text{if } 0 \leq t \leq t^* \\ 1 & \text{if } t \geq t^* \\ 0 & \text{if } t \leq t^* \end{cases}$$

is a third order polynomial approximating a sudden change in the temperature. For boundary condition type 1 (BCI), we consider $\beta(t) = 1$ when $t \geq t^*$, and for boundary condition type 2 (BCII), the value of $\beta(t) = 0$ when $t \leq t^*$.

4.4 Solution method

Unlike other solution methods, DQM does the computation over the entire spatial-temporal domain (z-x plane) at one step. Therefore, to accommodate the whole boundary conditions accurately, the time step should be considered very small. Increasing the number of sampling grid points to capture the boundary conditions causes a few problems: (1) increasing the order of the system of equations; (2) increasing the running time to compute the state variables; (3) the considerable accumulation of numerical errors due to the weighting coefficient of sampling grid points. To eliminate these drawbacks while keeping high-level accuracy, Shu [46] proposed an efficient temporal discretization approach based on block-marching in time and DQ discretization in both the spatial and temporal directions, as shown in Fig 3.2 [50]. The same approach is used here to solve the nonlocal heat conduction in a nanostructure. More details of this procedure can be found in the literature [46,48,103]. The p^{th} order derivative of the continuous function $f(z,t)$ in the spatial or temporal directions at an arbitrary sampling grid point z_i can be written as follows:

$$\frac{\partial f^p(z,t)}{\partial z^p} \Big|_{z=z_i} = \sum_{k=1}^N C_{ik}^p f(z_{ik}, t_j), \quad (4.10)$$

$$(i = 1, 2, \dots, N_z, j = 1, 2, \dots, N_t, p = 1, 2, \dots, N_z - 1)$$

$$\frac{\partial f^p(z,t)}{\partial t^p} \Big|_{t=t_i} = \sum_{k=1}^N D_{jk}^p f(z_{ik}, t_j), \quad (4.11)$$

$$(i = 1, 2, \dots, N_z, j = 1, 2, \dots, N_t, p = 1, 2, \dots, N_z - 1),$$

where N_z and N_t are the number of sampling points along z and t directions, respectively.

Also, C_{ik}^p and D_{jk}^p are the z_i and t_j dependent weight coefficients.

By considering the test functions as the Lagrange interpolation polynomials, the weighting coefficients of the first- and second-order derivatives are available in [27], and they are defined, respectively, by

$$C_{ik}^1 = \frac{M^{(1)}(z_i)}{(z_i - z_k)M^{(1)}(z_k)}, \quad \text{for } i \neq k, \quad i, k = 1, 2, \dots, N \quad (4.12)$$

$$C_{ik}^2 = 2C_{ik}^1 \left(C_{ii}^{(1)} - \frac{1}{z_i - z_k} \right), \quad \text{for } k \neq i, \quad i, j = 1, 2, \dots, N \quad (4.13)$$

$$C_{ii}^2 = - \sum_{k=1, k \neq i}^N C_{ik}^2,$$

where

$$M^{(1)}(z_i) = \prod_{m=1, m \neq i}^N (z_j - z_m) \quad (4.14)$$

DQM is employed to discretize the temporal and spatial derivatives. The total temporal domain is divided into a set of time intervals and the obtained temperature at the end of each time interval is used as an initial condition for the next time interval. Thereby, in the beginning, temperature and heat flux at a given control volume, P, at time, t , are obtained from the boundary conditions and then the value at time interval, $t + \Delta t$, is found, and will be considered as an initial condition for the next time step. So, all time intervals are connected, and the time history of temperature will be obtained. The DQM being applied to Eqs. (4.7, 4.8), the following equations at arbitrary sampling points z_i and t_j are then obtained:

$$k_{ij} \sum_{m=1}^{N_x} C_{im}^{z1} T_{mj} - l^2 \sum_{m=1}^{N_x} C_{im}^{z2} T_{mj} + \tau_q \sum_{n=1}^{N_t} D_{jn}^1 q_{in} + q_{ij} = 0 \quad (4.15)$$

$$\sum_{m=1}^{N_x} C_{im}^{z1} q_{mj} + \rho_{ij} C_{ij} \sum_{n=1}^{N_t} D_{jn}^1 T_{in} = g_{ij} \quad (4.16)$$

The solutions of Eqs. (4.15) and (4.16) will be obtained by employing the Newton-Raphson method.

4.5 Results and discussion

4.5.1 Validation

To predict the temperature distribution, the DQM has shown good agreement in all nodes with the analytical solution [51], as shown in Fig 2.3. The same values for the parameters are considered here as those in [51]. The results are presented for the hyperbolic heat conduction in a slab which is heated on both sides with zero initial conditions at the nanoscale. Reference [51] solved the hyperbolic heat conduction in the Laplace domain and used K_n to consider the effect of nonlocality.

4.5.2 Numerical results and discussion

In the following calculations, the heat conduction related parameters take these values, unless otherwise mentioned.

For nanobeam: $\rho = 1600 \frac{\text{kg}}{\text{m}^3}$, $t_o = 12 * 10^{-7} \text{ s}$, $C_p = 630 \frac{\text{J}}{\text{K}}$, $K = 30$, $r_i = 4 * 10^{-12} \text{ m}$, $r_o = 16 * 10^{-12} \text{ m}$ and $l = 2 * 10^{-8} \text{ m}$. Here r_i and r_o are the inner and outer radii of the hollow cylinder, $r = \frac{r_i + r_o}{2}$.

Also, the number of sampling grid points for DQM is considered equal to 21, time increment (dt) is 1 fs and $t^* = 50 \text{ fs}$ unless otherwise mentioned.

In Figs 4.2 and 4.3 are showing the temperature distribution from different angles and we

assumed that there is a thermal shock on both inner (r_i) and outer (r_o) surfaces of the cylinder. For the thermal shock, there is a $10\text{ }^\circ\text{C}$ increase in temperature in 50 fs and then it stays still. The fast rise in temperature at the boundaries (r_i and r_o) happens as a result of prescribed boundary conditions. The increase in the temperature in the middle parts of the thickness is slower due to the time required for heat flux to entirely reach and cover this area. Also, thermal waves can be seen in Fig 4.2, and the amplitude of waves in the beginning are bigger and sharper wavefronts appear, but after a while the effect of thermal shock phases out and waves become smoother. (The amplitudes of wave at $t = 250\text{ fs}$ are smaller than the amplitude of waves at $t = 50$ or 100 fs)

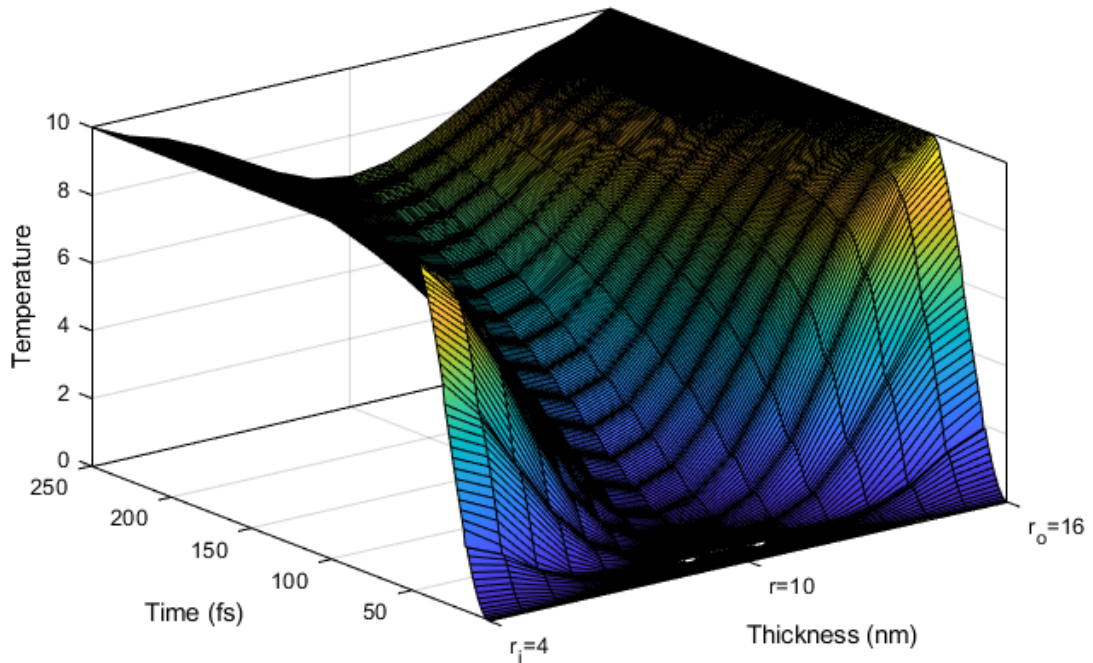


Figure 4. 2 Time history of the temperature distribution at different points through the thickness

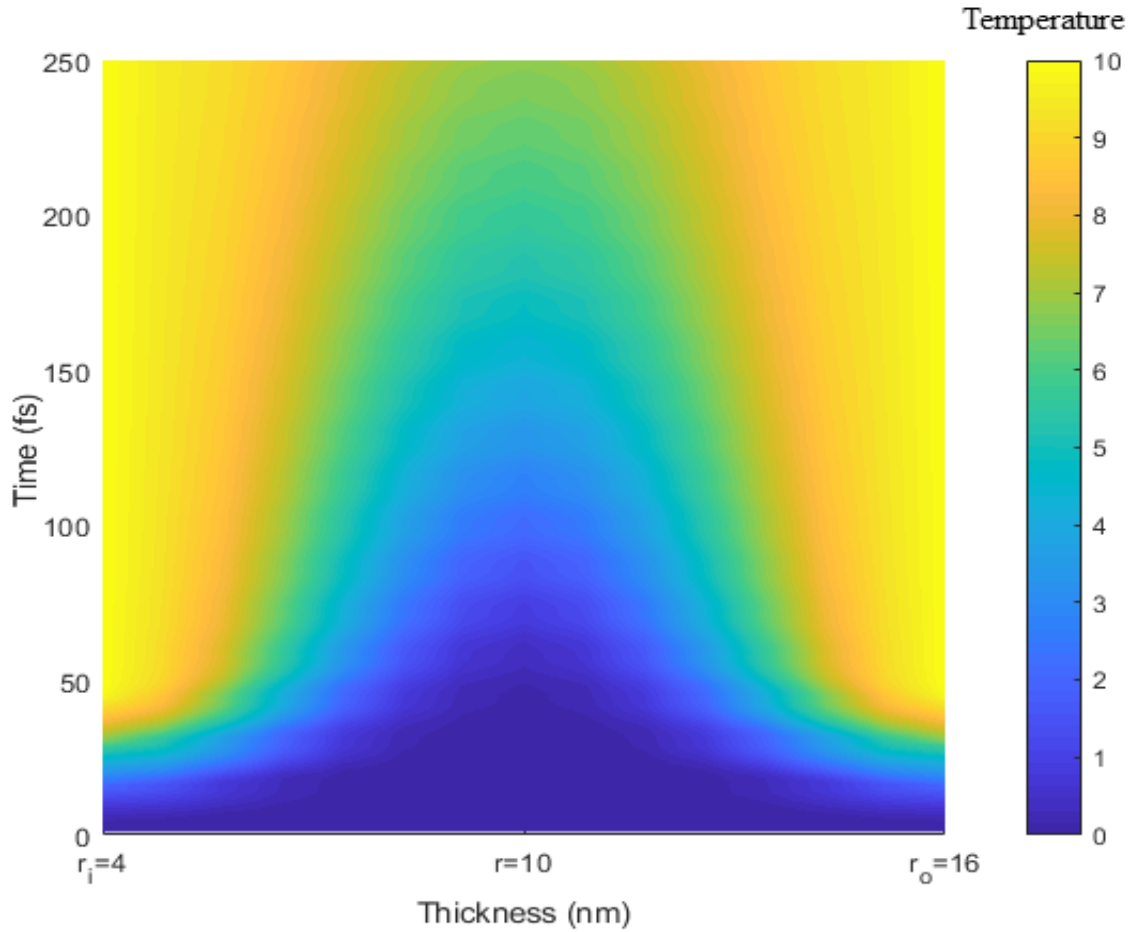


Figure 4. 3 Heat transfer simulation in Matlab (Heatmap)

distribution. As shown in Fig. 4.4 (a), $t^* = 0$ means temperature at the boundary is constant ($T=10$), and it gives the highest value of the temperature throughout the thickness of the nanobeam (Fig. 4.4 (b)). By increasing the value of t^* , and plotting the temperature pattern at $t = 20 \text{ fs}$, the lower temperature will be obtained, as shown in Fig. 4.4 (b). This means, for higher value of t^* , there is a smooth raise in temperature instead of having a thermal shock, so the speed of heat propagation in the medium decreases.

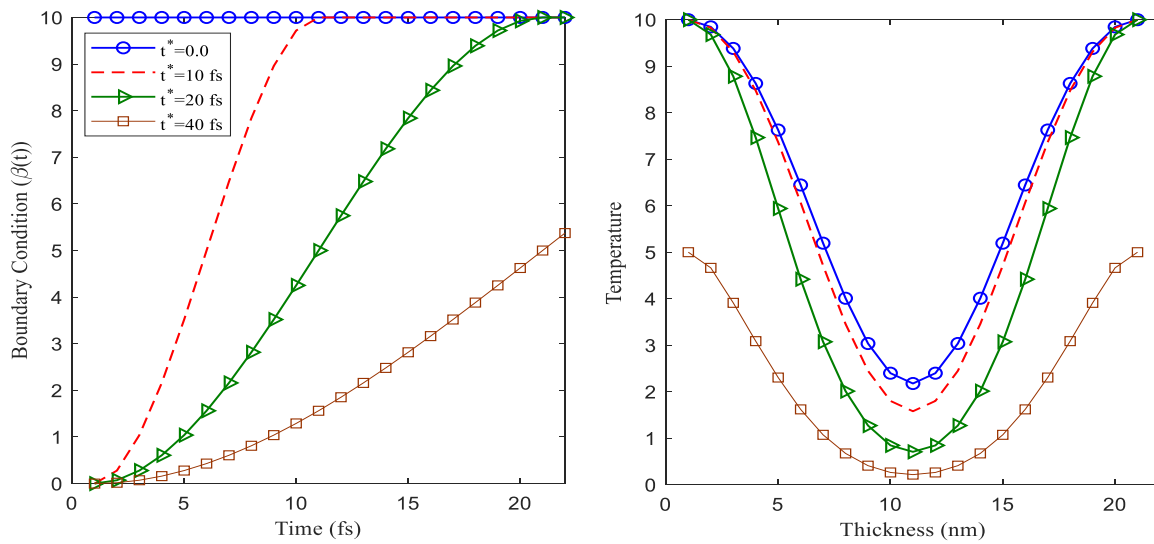


Figure 4. 4 Temperature distribution through the thickness by changing the time duration of the thermal shock (t^*) (a) Boundary conditions, (b) temperature distribution across the thickness of the carbon nanotube at $t=20$ fs.

Temperature distributions through the thickness of the cylinder are presented in Fig. 4.5 at different characteristic lengths. In Fig. 4.5, presence of the internal characteristic length prevents the temperature from exceeding the boundary temperatures, which also known as overshooting and may damage electrical devices if it is not handled correctly. Furthermore, the small value of the nonlocal length keeps the nonlocal effect within a physical domain contiguous to the imposed thermal shock at the boundary. As the characteristic length becomes conspicuous at a large value of the nonlocal length, the nonlocal effect escalates from the border and propagates within the medium.

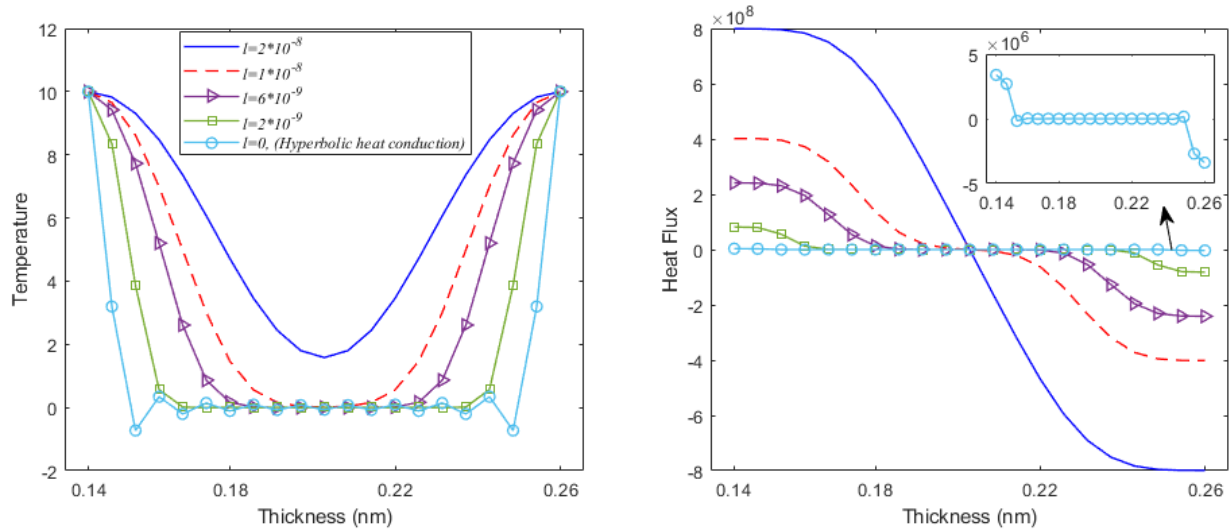


Figure 4. 5 Effects of the characteristic length (l) on the temperature distribution at $t=20$ fs.

Figure 4.6 depicts the temperature distribution at $t=20$ fs for different relaxation times. The increase in thermal relaxation time causes a decrease in thermal wave propagation speed and thereby decreases the change in temperature away from the imposed boundary. As shown in Fig. 4.6, for the highest value of the relaxation time, $\tau_0 = 12 * 10^{-4} s$, a large proportion of the thickness has not experienced the thermal shock and the temperature has remained zero. On the other hand, for $\tau_0 = 12 * 10^{-7} s$, which is the lowest value of relaxation time, the whole thickness domain has been affected by the thermal shock at the boundary. This is due to the faster heat propagation at smaller time delays. When the time delay is larger, heat needs more time to travel the whole domain and therefore lags behind.

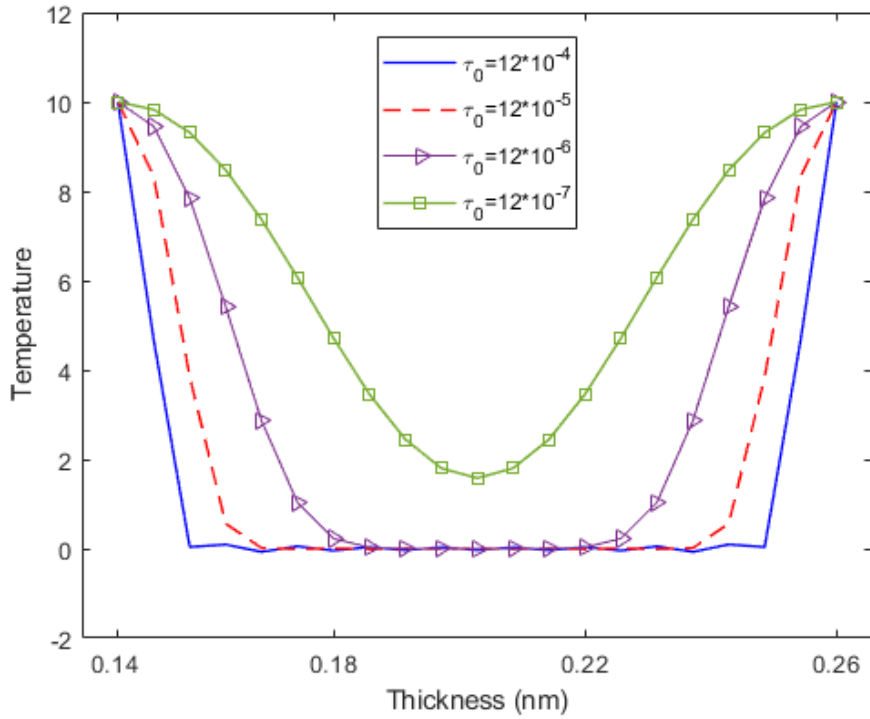


Figure 4. 6 Effects of the relaxation time on the temperature distribution at $t=20$ fs.

The temperature distribution through the thickness for the second type of boundary condition is presented in Fig. 4.7. Figures 4.7 and 4.8 show that the temperature in the area close to the inner (r_i) and outer (r_o) surfaces first increase very fast in the heating stage ($0 < t < 10$ fs). Then the heat source at the boundary disappears, and temperature becomes zero in these areas. Although we have removed the heat source from the boundary, the effects of thermal shock are still observed in the middle parts of the thickness. The heat transfer within the media can be seen in Fig. 4.8. It is illustrated that although the temperature at the boundary is set to zero after 50 fs, the heat transfer continues and tends to move toward the center of the media.

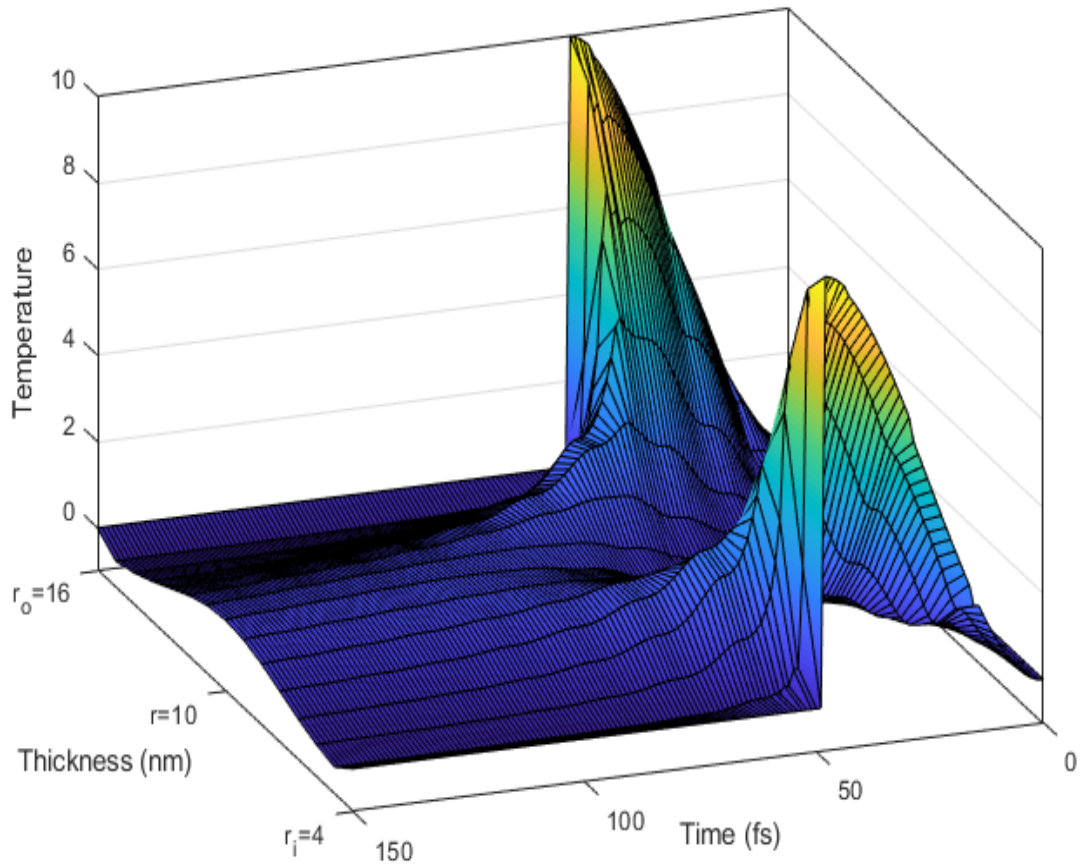


Figure 4. 7 Temperature history of the temperature, BC: II

Figure 4.9 is a comparison between the effects of two different boundary conditions on the temperature distribution within the nano-cylinder. In the case of $\tau_0 = 0.8fs$ and $1 fs$ there has been some exciting result. We observed that for two different boundary conditions, the temperature of some regions in the middle of the thickness is the same. We can justify it by considering the fact that temperature in the area away from the imposed boundary, at initial stages, depends more on the characteristic length and relaxation time. Boundary conditions determine the limits of the temperature, and characteristic length and relaxation time define how fast the medium can reach these limits. So, it is possible to design a system in which heat propagates based on the needs. For example, we can control the maximum temperature and the time duration to establish a certain temperature, and how to reach a certain temperature through different boundary conditions.

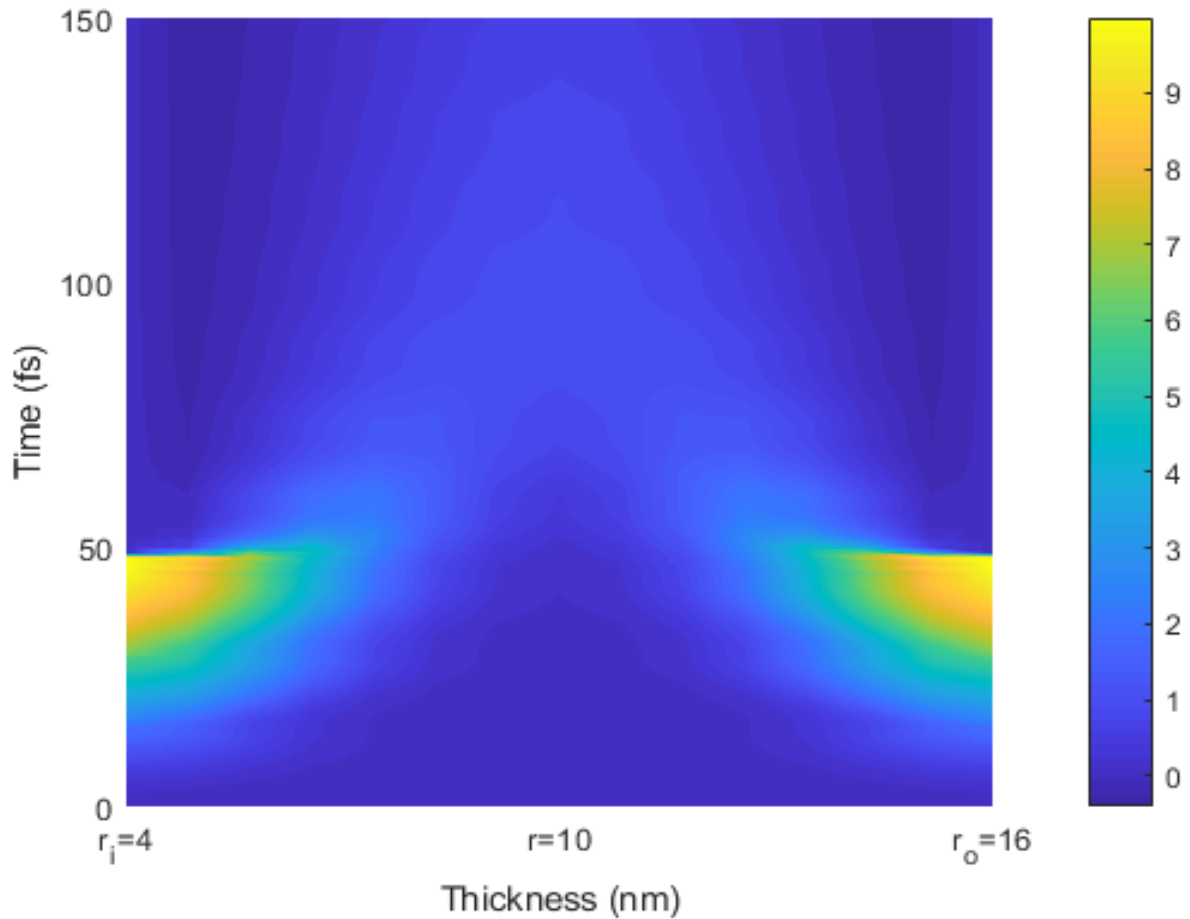


Figure 4. 8 Visualizing temperature with single heatmap, BC: II

Figure 4.10 plots the variation of temperature distribution at $t=20$ fs through the thickness of the beam for different thickness ratios ($\frac{r_o}{r_i}$). It shows that the temperature gradually decreases with increasing thickness ratio. For the shortest value of the thickness ratio, the whole thickness has experienced a change in temperature, but for the bigger value of the thickness ratio, the temperature at the area around the center ($r = r_i + \frac{r_o}{2}$) remains the same.

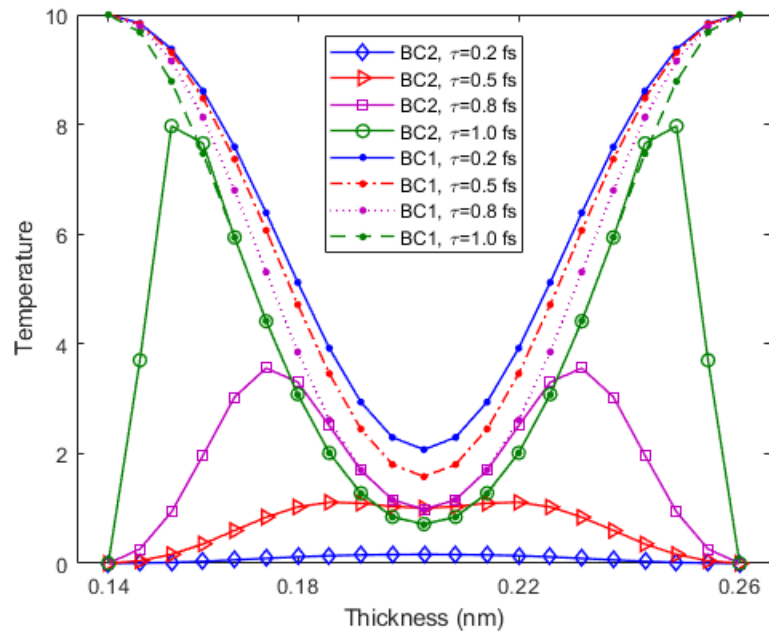


Figure 4. 9 Transition from non-Fourier heat conduction to Fourier heat conduction at $t=20$ fs.

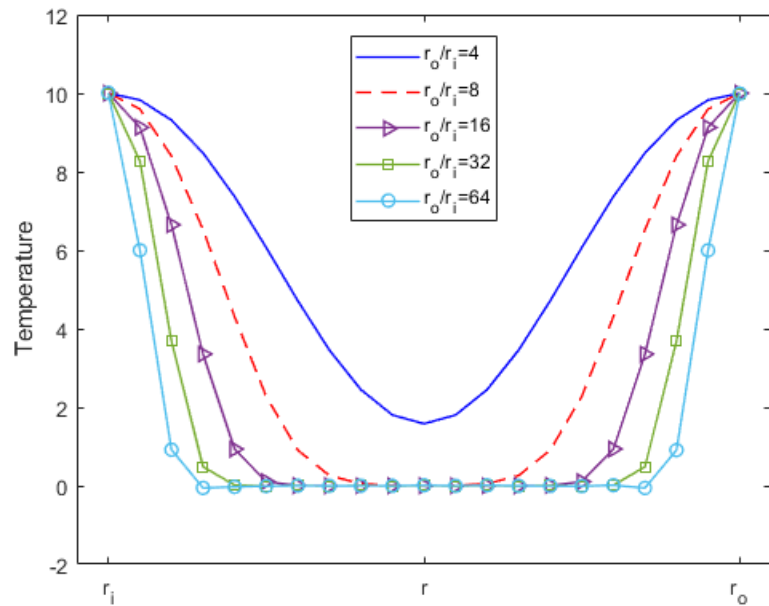


Figure 4. 10 Effects of the thickness ratio on the temperature distribution

4.6 Conclusion

A semi-analytical solution for the modified Guyer-Krumhansl equation is addressed for a nanobeam modelled as a cylindrical shell using the differential quadrature method. The differential quadrature approach is employed to develop a new solution method leading to a more straightforward solution, convenient to apply different boundary conditions or material properties, and even simple in two or three-dimensional problems. The linear effect of nonlocality was extended in space under the direct impact of thermal lagging in time. For the large values of relaxation time, the time delay effect is restricted to a physical domain close to the boundary. Decreasing the value of the time delay pushes the thermal waves forward. Furthermore, When the characteristic length is small, there is a sharp decline in temperature near the boundary, while the temperature in the center of the cylinder has no difference with that obtained from hyperbolic heat conduction. Accordingly, the same phenomenon happens for the heat flux. The small characteristic length confines the effects of the interactions between boundary and energy carriers within a physical domain near the boundary. The main contribution of this chapter was to prove to what extent heat transfer can differ at the nanoscale from that at the macroscale. The result of this chapter can be useful in designing the nanoscale devices such as nanocoolers which have an ever-increasing application in quantum computers.

Chapter 5:

Nonlinear vibration and modal analysis of FG nanocomposite sandwich beams reinforced by aggregated CNTs⁴

In the present work, by considering the aggregation effect of single-walled carbon nanotubes (SWCNT), the nonlinear vibration of functionally graded (FG) nanocomposite sandwich Timoshenko beams resting on Pasternak foundation are presented. The material properties of the FG nanocomposite sandwich beam are estimated using the Eshelby–Mori–Tanaka approach and differential quadrature method (DQM) is used to obtain natural frequency. The nonlinear governing equations and boundary conditions are derived using the Hamilton principle and von Kármán geometric nonlinearity. The higher-order nonlinear governing equations and boundary conditions are calculated using the Hamilton principle. A direct iterative method is employed to determine the nonlinear frequencies and mode shapes of the beams. It is shown that the mechanical properties and therefore vibration of functionally graded carbon nanotube reinforced (FG-CNTR) sandwich beams are severely affected by CNTs aggregation. A detailed parametric study is carried out to investigate the influences of Winkler foundation modulus, shear elastic foundation modulus, length to span ratio, thicknesses of face sheets on the nonlinear vibration of the structure.

5.1 Introduction

Over the past few years, there has been an ever-increasing interest in CNTs due to their

⁴ A version of this chapter is published in the journal of Polymer Engineering & Science 59 (7), 1362-1370, 2019.

outstanding and exceptional mechanical, electrical and thermal properties [104-107] have stimulated researchers to exploit them as a new generation of reinforcing agents for polymers. Numerous studies have been made to analytically and experimentally determine the mechanical properties of CNTR nanocomposites as molecular dynamics (MD) simulation [60,108,109], continuum mechanics [110,61,62] and multi-scale simulation [59,63] G.D. Seidel et al. [111] focused on the obtain effective elastic properties of composites consisting of aligned single or multi-walled carbon nanotubes embedded in a polymer matrix. They also investigated on the effect of an interphase layer between the nanotube and the polymer matrix as a result of functionalization. For the same reasons mentioned above, CNTs have received increased attention as reinforcements for polymer composites.

One of the characteristic features of CNT morphology is the formation of aggregation in the matrix. The macromechanical properties of nanocomposites are affected by the microstructure and volume fraction of CNTs. Several methods are used to evaluate the effective properties of nanocomposites, including those based on single inclusion theory [112], such as Mori–Tanaka method [113], the self-consistent scheme [114], and differential method [115], among others.

The Mori–Tanaka (MT) model is selected here to determine the effective material constants of the nanocomposite material accounting for the direction and aggregation of CNTs in the composites. Yang et al. [116] used the Mori-Tanaka approach to show the effect of CNT aggregation in the composite. They illustrated the degree of CNT aggregation dramatically influences the effective properties of the CNT/SMP composites. Barai [117] developed a two-scale micromechanical model to analyze the effect of CNT aggregation and interface condition on the plastic strength of CNT/matrix inclusions, and the small-scale addressed the property of the clustered inclusions.

The nonlinear and linear vibration of sandwich beams, plates and panels has been an object of many studies [118-125]. Nanocomposite FG sandwich structures are widely used in the field of transportation (helicopter blades, ship's hull, etc.) for their low weight and high in-plane and flexural stiffness. So, with the wide application of FG sandwich structures, understanding their responses becomes an essential task. Though there are research works reported on general sandwich structures, studies related to nonlinear vibration of FG nanocomposite sandwich structures are few in numbers.

Bending analysis of a sandwich beam with softcore and carbon nanotube reinforced composite face sheets in the literature is carried out by Jedari Salami [126] based on Extended High order Sandwich Panel Theory. In this theory, the face sheets follow the first order shear deformation theory. Xiang and Yang developed a two dimensional elasticity solution [127] to obtain the free and forced vibration characteristics of laminated FG Timoshenko beam of variable thickness, which consists of a homogeneous substrate and two inhomogeneous functionally graded layers, subjected to one-dimensional steady heat conduction in the thickness direction, employing the differential quadrature method.

Ke et al. [128,129] analyzed the nonlinear free vibrations of FG-CNTR Timoshenko beams with symmetric and unsymmetrical distributions of CNTs along the thickness direction using Ritz method and direct iterative technique. Also, they investigated [129] on the nonlinear free vibration of the FGM microbeams based on the modified couple stress theory and Timoshenko beam theory. Mori-Tanaka homogenization technique is employed to model the through-the-thickness variation of the material properties in a simple power law function. They used the differential quadrature method to discretize the nonlinear governing equations which are then solved by a direct iterative algorithm to obtain the nonlinear vibration frequencies of the FGM microbeams.

This paper is motivated by the lack of studies in the technical literature concerning the influence of graded agglomerated CNTs on nonlinear free vibration analysis of functionally graded sandwich carbon nanotube reinforced (FGS-CNTR) beams on Pasternak foundation. A numerical method that makes use of the differential quadrature method together with an iterative algorithm is employed to determine the nonlinear vibration frequencies of the FG nanocomposite beams with different boundary conditions. The face sheets are reinforced by CNT volume fraction graded according to a power-law distribution. Various material profiles through the thickness of face sheets can be illustrated by using the power-law distribution. Nonlinear free vibration analysis of FGS-CNTRS beams is studied based on Timoshenko beam theory and through MT model and DQ method which is found to be a simple and efficient numerical technique for solving partial differential equations [80,103,130,131]. The effects of the degree of CNT aggregation, CNT volume fraction, Pasternak foundation, geometric parameters, etc, on the nonlinear vibration of the structure are presented in this paper.

5.2 Material properties of CNT reinforced composites

5.2.1 Effect of CNT aggregation on the properties of the composite

To better predict material properties of FG nanocomposite sandwich beams, the Mori-Tanaka homogenization scheme is used in this study [77,132,133]. The CNTs were arranged within the matrix in such manner to introduce clustering. It has been observed that, due to large aspect ratio, the low bending rigidity of CNTs and van der Waals forces, CNTs tend to bundle or cluster together making it quite difficult to produce fully dispersed CNT reinforced composites. The effect of nanotube aggregation on the elastic properties of randomly oriented CNTRC is presented in this section. Two parameter micromechanics models are derived to determine the effect of nanotube aggregation on the elastic properties of randomly oriented CNTRC (Fig 5.1). It

is assumed that some CNTs are uniformly distributed throughout the matrix and that other CNTs appear in cluster form because of aggregation, as shown in Fig 5.1. The total volume of the CNTs in the representative volume element (RVE), denote by V_r , can be divided into the following two parts [112,113]:

$$V_r = V_r^{cluster} + V_r^m \quad (5.1)$$

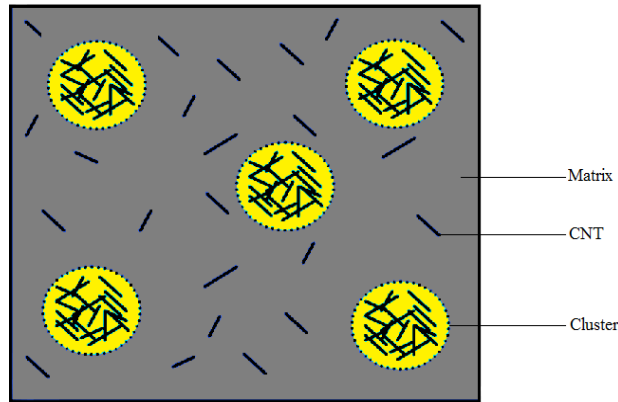


Figure 5. 1 RVE with Eshelby cluster model of aggregation of CNTs.

where $V_r^{cluster}$ denote the volumes of CNTs inside a cluster, and V_r^m is the volume of CNTs in the matrix and outside the clusters. The two parameters used to describe the aggregation are defined as:

$$\mu = \frac{V_{cluster}}{V} , \quad \eta = \frac{V_r^{cluster}}{V_r} \quad 0 \leq \eta, \mu \leq 1 \quad (5.2)$$

where V is the volume of RVE, $V_{cluster}$ volume of clusters in the RVE, μ is the volume fraction of clusters concerning the total volume V of the RVE, η is the volume ratio of the CNTs inside the clusters over the entire CNTs inside the RVE. The effective bulk modulus K and the effective shear modulus G of the composite are derived from the Mori-Tanaka method as follows [77]:

$$K = K_{out} \left[1 + \frac{\mu \left(\frac{K_{in}}{K_{out}} - 1 \right)}{1 + \alpha(1 - \mu) \left(\frac{K_{in}}{K_{out}} - 1 \right)} \right] \quad (5.3)$$

$$G = G_{out} \left[1 + \frac{\mu \left(\frac{G_{in}}{G_{out}} - 1 \right)}{1 + \beta(1 - \mu) \left(\frac{G_{in}}{G_{out}} - 1 \right)} \right] \quad (5.4)$$

with

$$\nu_{out} = \frac{(3K_{out} - 2G_{out})}{2(3K_{out} + G_{out})} \quad (5.5)$$

$$\alpha = \frac{(1 + \nu_{out})}{3(1 - \nu_{out})} \quad (5.6)$$

$$\beta = \frac{2(4 - 5\nu_{out})}{15(1 - \nu_{out})} \quad (5.7)$$

The effective Young's modulus E and Poisson's ratio ν of the composite can be calculated in terms of K and G by:

$$E = \frac{9KG}{3K + G} \quad (5.8)$$

$$\nu = \frac{3K - 2G}{6K + 2G} \quad (5.9)$$

Consider a functionally graded CNT reinforced beam resting on Pasternak foundations as shown in Fig 5.2. In the present work, V_{CN} and V_m are considered as the CNT and matrix volume fraction, respectively. We assume for FG beam, the volume fraction of the CNT is given by the

power-law-type function:

$$V_{CN}(z) = \begin{cases} V_{CN} = V_o + (V_i - V_o) \left(\frac{z + h/2}{h_f} \right)^q & , \frac{-h}{2} \leq z \leq \frac{-h}{2} + h_f \\ V_i & , \frac{-h}{2} + h_f \leq z \leq \frac{h}{2} - h_f \\ V_{CN} = V_o + (V_i - V_o) \left(\frac{-z + h/2}{h_f} \right)^q & , \frac{h}{2} - h_f \leq z \leq \frac{h}{2} \end{cases} \quad (5.10)$$

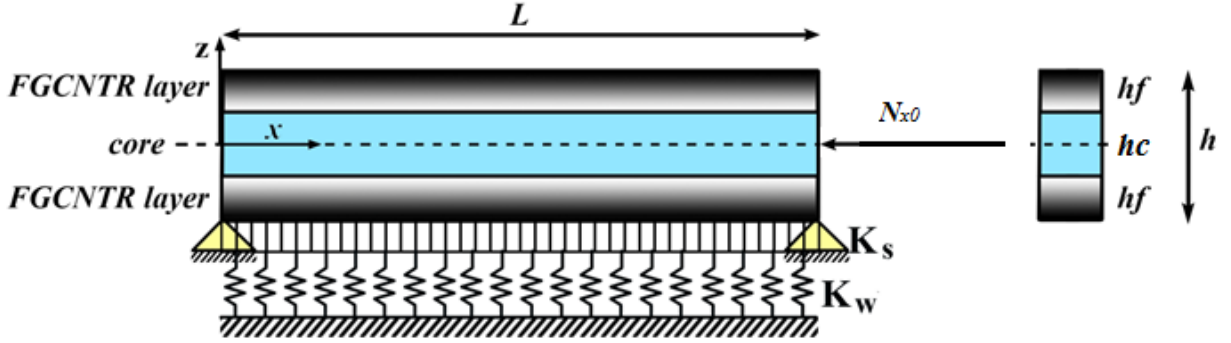


Figure 5. 2 Geometry of FGS-CNTR beam

where the volume fraction index q ($0 \leq q \leq \infty$), h and h_f are the thicknesses of beam and the face sheets respectively and V_o and V_i , which have values that range from 0 to 1, denote the maximum and minimum volume fraction of CNT that could exist in the thickness direction. According to relation (10), the amount of CNT in the core of the structure is constant and equal to V_i . Various material profiles through the thickness of face sheets can be illustrated by using the power-law distribution.

The through-thickness variations of CNT volume fraction for some profiles are illustrated in Fig 5.3. In Fig 5.3 the classic CNT volume fraction profiles are presented. As we can see, a sandwich beam made up of three discrete layers with a homogeneous core.

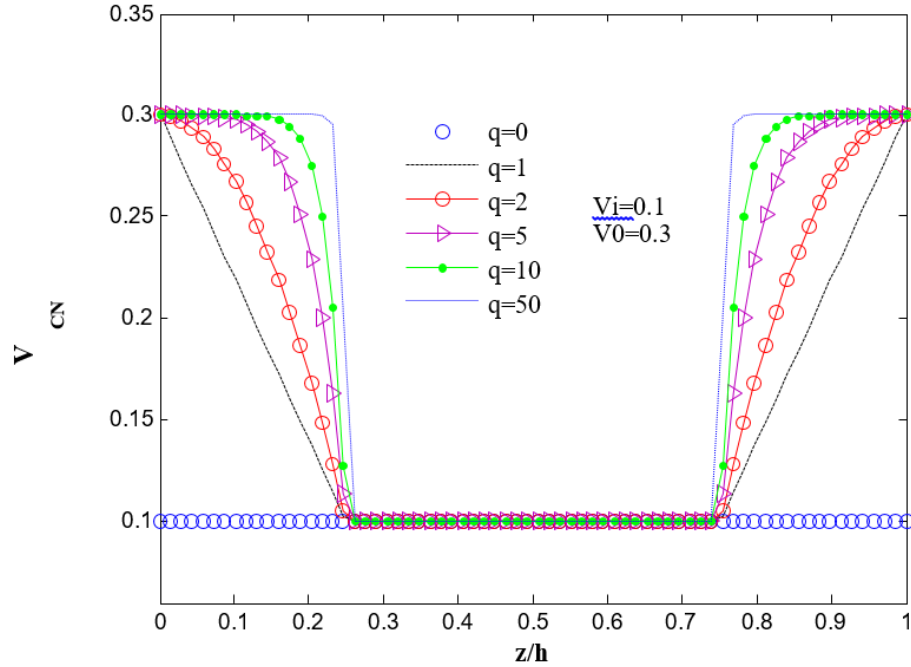


Figure 5. 3 Variation of the CNT volume fraction through the thickness of the beam (q is the volume fraction index)

5.3 Equations of motion

Timoshenko beam theory is employed in this paper with the following displacement field to account for the effect of transverse shear strain which is essential in the deformation of composite structures

$$U(x, y, z, t) = u_0(x, z, t) + z\psi(x, z, t) \quad (5.11a)$$

$$W(x, y, z, t) = w_0(x, z, t) \quad (5.11b)$$

in which u_0 and w_0 represent the components of displacement at $z=0$, ψ is the section normal vector rotations about the y -axes, and t is time.

Consider the FGS-CNTR beam shown in Fig 5.2. The beam is assumed to be rested on the two-parameter elastic (Pasternak) foundation whose supporting action is described by

$$P = K_w w - K_s \frac{\partial^2 w}{\partial x^2} \quad (5.12)$$

where P is the foundation reaction per unit area, w is the transverse deflection of the beam, and K_w , K_s are Winkler and shearing layer elastic coefficients of the foundation. It is worth noting that the Pasternak elastic foundation model is an extension of the well-known Winkler model ($K_s = 0$).

The normal linear strain ε_x and shear strain γ_{xz} are associated with the displacements as:

$$\varepsilon_x = \frac{\partial u_0}{\partial x} + z \frac{\partial \psi}{\partial x} + \frac{1}{2} \left(\frac{\partial w_0}{\partial x} \right)^2, \quad \gamma_{xz} = \frac{\partial w_0}{\partial x} + \psi \quad (5.13)$$

Using the linear elastic constitutive law, the normal stress σ_x and shear stress τ_{xz} are given by

$$\begin{aligned} \sigma_x(z) &= Q_{11}(z) \varepsilon_x \\ \tau_{xz}(z) &= Q_{55}(z) \gamma_{xz} \end{aligned} \quad (5.14)$$

in which

$$Q_{11}(z) = \frac{E(z)}{1-\nu^2}, \quad Q_{55}(z) = \frac{E(z)}{2(1+\nu)} \quad (5.15)$$

Employing Hamilton's principle, the equations of motion and the related boundary conditions can be derived. According to Hamilton's principle

$$\delta \int_0^t (T - \Pi + \gamma_p) dt = 0 \quad (5.16)$$

where δ , T and Π denote the variational symbol, the kinetic energy of the beam and potential energy composed of strain energy the beam together with the elastic potential energy of the elastic foundation respectively. It is worth noting that γ_p is the work done by an external force that is zero for free vibration analysis.

By setting the coefficients of δu , δw and $\delta \psi$ to zero leads to the equations of motion

as

$$\delta u : \frac{\partial N_x}{\partial x} = I_1 \frac{\partial^2 u_0}{\partial t^2} + I_2 \frac{\partial^2 \psi}{\partial t^2} \quad (5.17a)$$

$$\delta w : \frac{\partial Q_x}{\partial x} + \frac{\partial}{\partial x} \left(N_x \frac{\partial w}{\partial x} \right) - K_f w_0 + K_s \frac{\partial^2 w_0}{\partial x^2} = I_1 \frac{\partial^2 w}{\partial t^2} \quad (5.17b)$$

$$\delta \Psi : \frac{\partial M_x}{\partial x} - Q_x = I_2 \frac{\partial^2 u_0}{\partial t^2} + I_3 \frac{\partial^2 \psi}{\partial t^2} \quad (5.17c)$$

where the resultant normal force N_x , bending moment M_x , and transverse shear force Q_x are calculated from

$$\begin{Bmatrix} N_x \\ M_x \\ Q_x \end{Bmatrix} = \int_{-h/2}^{h/2} \begin{Bmatrix} \sigma_{xx} \\ z \sigma_{xx} \\ \tau_{xz} \end{Bmatrix} dz = \begin{Bmatrix} A_{11} \left[\frac{\partial u_0}{\partial x} + \frac{1}{2} \left(\frac{\partial w_0}{\partial x} \right)^2 \right] + B_{11} \frac{\partial \psi}{\partial x} \\ B_{11} \left[\frac{\partial u_0}{\partial x} + \frac{1}{2} \left(\frac{\partial w_0}{\partial x} \right)^2 \right] + D_{11} \frac{\partial \psi}{\partial x} \\ k^* A_{55} \left(\frac{\partial w_0}{\partial x} + \psi \right) \end{Bmatrix} \quad (5.18)$$

In this study, the shear correction factor $k^* = \frac{5}{6}$ is used, and the stiffness components A_{11} ,

B_{11} , D_{11} , A_{55} of the beam are defined as:

$$\begin{aligned} (A_{11}, B_{11}, D_{11}) &= \int_{-h/2}^{h/2} Q_{11}(z)(1, z, z^2) dz, & A_{55} &= \int_{-h/2}^{h/2} Q_{55}(z) dz \\ (I_1, I_2, I_3) &= \int_{-h/2}^{h/2} \rho(z)(1, z, z^2) dz \end{aligned} \quad (5.19)$$

Different boundary conditions of the beams such as hinged-hinged (H-H), clamped-hinged (C-H), clamped-clamped (C-C) and clamped-free (C-F) can be considered. These conditions are

described as:

$$\begin{aligned}
 \text{Clamped (C):} \quad u_0 = w_0 = \Psi = 0 \\
 \text{Hinged (H):} \quad u_0 = w_0 = M_x = 0
 \end{aligned}
 \tag{5.20}$$

Since we need to compare our results with the similar ones in the previous works, in the present study we used a beam with the hinged condition over simply supported beam. By using the following dimensionless quantities

$$\begin{aligned}
 \xi = \frac{x}{L}, \quad (\bar{U}, \bar{W}) &= \frac{(u_0, w_0)}{h}, \\
 (a_{11}, a_{55}, b_{11}, d_{11}) &= \left(\frac{A_{11}}{A_{110}}, \frac{A_{55}}{A_{110}}, \frac{B_{11}}{A_{110}h}, \frac{D_{11}}{A_{110}h^2} \right), \\
 \psi = \Psi, \quad \lambda = L/h, \quad (\bar{I}_1, \bar{I}_2, \bar{I}_3) &= \left(\frac{I_1}{I_{10}}, \frac{I_2}{I_{10}h}, \frac{I_3}{I_{10}h^2} \right) \\
 k_w = \frac{K_w L^2}{A_{110}}, \quad k_s = \frac{K_s}{A_{110}} \\
 \tau = \frac{t}{L} \sqrt{\frac{A_{110}}{I_{10}}}
 \end{aligned}
 \tag{5.21}$$

in which A_{110} and I_{10} are the values of A_{11} and I_1 of a homogeneous polymeric beam. , Eq. (5.21)

can be transformed into the following dimensionless form:

$$a_{11} \left(\frac{\partial^2 u}{\partial \xi^2} + \frac{1}{\lambda} \frac{\partial w}{\partial \xi} \frac{\partial^2 w}{\partial \xi^2} \right) + b_{11} \frac{\partial^2 \psi}{\partial \xi^2} = \bar{I}_1 \frac{\partial^2 u}{\partial \tau^2} + \bar{I}_2 \frac{\partial^2 w}{\partial \tau^2}
 \tag{5.22a}$$

$$k^* a_{55} \left(\frac{\partial^2 w}{\partial \xi^2} + \lambda \frac{\partial \psi}{\partial \xi} \right) + \frac{a_{11}}{\lambda} \left(\frac{\partial^2 u}{\partial \xi} \frac{\partial^2 w}{\partial \xi^2} + \frac{3}{2\lambda} \left(\frac{\partial w}{\partial \xi} \right)^2 \frac{\partial^2 w}{\partial \xi^2} + \frac{\partial^2 u}{\partial \xi^2} \frac{\partial w}{\partial \xi} \right) + \frac{b_{11}}{\lambda} \left(\frac{\partial^2 \psi}{\partial \xi^2} \frac{\partial w}{\partial \xi} + \frac{\partial \psi}{\partial \xi} \frac{\partial^2 w}{\partial \xi^2} \right) - k_w w + k_s \frac{\partial^2 w}{\partial \xi^2} = \bar{I}_1 \frac{\partial^2 w}{\partial \tau^2} \quad (5.22b)$$

$$b_{11} \left(\frac{\partial^2 u}{\partial \xi^2} + \frac{1}{\lambda} \frac{\partial w}{\partial \xi} \frac{\partial^2 w}{\partial \xi^2} \right) + d_{11} \frac{\partial^2 \psi}{\partial \xi^2} - k^* \lambda a_{55} \left(\frac{\partial w}{\partial \xi} + \eta \psi \right) + = \bar{I}_2 \frac{\partial^2 u}{\partial \tau^2} + \bar{I}_3 \frac{\partial^2 \psi}{\partial \tau^2} \quad (5.22c)$$

The associated boundary conditions can also be written in a dimensionless form as:

$$u = w = \psi = 0 \quad (5.23)$$

for a clamped-clamped (C-C) boundary condition

$$u = w = b_{11} \left(\frac{\partial u}{\partial \xi} + \frac{1}{2\lambda} \left(\frac{\partial w}{\partial \xi} \right)^2 \right) + d_{11} \frac{\partial \psi}{\partial \xi} = 0 \quad (5.24)$$

for a hinged-hinged (H-H) boundary condition

5.4 Solution method, DQM

The differential quadrature method (DQM) [134,135] is used to solve Eq. (5.25) and the associated boundary conditions to determine the nonlinear frequencies of FGS-CNTR beam resting on Pasternak foundation. The fundamental idea of the DQ method is to approximate the derivative of a function at a sample point as a linear weighted sum of the function values at all of the sample points in the problem domain. Hence, the n th order of a continuous function $f(x, z)$ concerning x at a given point x_i can be approximated as a linear sum of weighting values at all of the discrete points in the domain of x , i.e.

$$\frac{\partial^n f^{n(x_i, z)}}{\partial x^n} = \sum_{k=1}^N c_{ik}^n f(x_{ik}, z), \quad (i=1,2,\dots,N, n=1,2,\dots,N-1) \quad (5.25)$$

where N is the number of sampling points, and c_{ij}^n [134] is the x_i dependent weight coefficients.

The cosine pattern is used to generate the DQ point system

$$x_i = \frac{1}{2} \left(1 - \cos \left(\frac{i-1}{n-1} \pi \right) \right) \quad i = 1, 2, \dots, N \quad (5.26)$$

Applying Eq. (5.25) to Eq. (5.22), one obtains a set of ordinary differential equations

$$a_{11} \left(\sum_{j=1}^N C_{ij}^2 u_j + \frac{1}{\lambda} \sum_{j=1}^N C_{ij}^1 w_j \sum_{j=1}^N C_{ij}^2 w_j \right) + b_{11} \sum_{j=1}^N C_{ij}^2 \psi_j = \bar{I}_1 \ddot{u} + \bar{I}_2 \ddot{w} \quad (5.27a)$$

$$k^* a_{55} \left(\sum_{j=1}^N C_{ij}^2 w_j + \lambda \sum_{j=1}^N C_{ij}^1 \psi_j \right) + \frac{a_{11}}{\lambda} \left(\sum_{j=1}^N C_{ij}^1 u_j \sum_{j=1}^N C_{ij}^2 w_j + \frac{3}{2\lambda} \left(\sum_{j=1}^N C_{ij}^1 w_j \right)^2 \sum_{j=1}^N C_{ij}^2 w_j + \sum_{j=1}^N C_{ij}^2 u_j \sum_{j=1}^N C_{ij}^1 w_j \right) \quad (5.27b)$$

$$+ \frac{b_{11}}{\lambda} \left(\sum_{j=1}^N C_{ij}^2 \psi_j \sum_{j=1}^N C_{ij}^1 w_j + \sum_{j=1}^N C_{ij}^1 \psi_j \sum_{j=1}^N C_{ij}^2 w_j \right) - k_w w_i + k_s \sum_{j=1}^N C_{ij}^2 w_j = \bar{I}_1 \ddot{w}$$

$$b_{11} \left(\sum_{j=1}^N C_{ij}^2 u_j + \frac{1}{\lambda} \sum_{j=1}^N C_{ij}^1 w_j \sum_{j=1}^N C_{ij}^2 w_j \right) + d_{11} \sum_{j=1}^N C_{ij}^2 \psi_j - k^* a_{55} \lambda \left(\sum_{j=1}^N C_{ij}^1 w_j + \lambda \psi_i \right) \quad (5.27c)$$

$$= \bar{I}_2 \ddot{u} + \bar{I}_3 \ddot{\psi}$$

The associated boundary conditions can be handled in the same way. For example, the dimensionless boundary condition of clamped-Hinged (C-H) Supported beams is

$$u_1 = w_1 = \psi_1 = 0 \quad \text{at } \zeta = 0$$

$$\begin{cases} u_N = w_N = 0 \\ M_x = b_{11} \left(\sum_{j=1}^N c_{Nj}^1 u_j - \frac{1}{2\lambda} \left(\sum_{j=1}^N c_{Nj}^1 w_j \right)^2 \right) + d_{11} \sum_{j=1}^N c_{Nj}^1 \Psi_j = 0 \end{cases} \quad \text{at } \zeta = 1 \quad (5.28)$$

After implementation of the boundary conditions, Eq. (5.27) can be written in matrix form

as

$$\left(K_L + \frac{1}{2}K_{NL1} + \frac{1}{3}K_{NL2}\right)U_d + M\ddot{U}_d = 0 \quad (5.29)$$

where M is the mass matrix; K_L is the linear stiffness matrix; K_{NL1} and K_{NL2} are nonlinear stiffness matrices that are linear and quadratic functions in U_d , respectively.

Expanding the dynamic displacement vector U_d in the form of $U_d = U_d^* e^{i\omega t}$ where $\omega = \Omega L \sqrt{\sigma / E}$ represents the dimensionless frequency, Ω is the nonlinear vibration frequency of the FG nanocomposite sandwich beam, U_d^* is the vibration mode shape vector. Substituting U_d into Eq. (5.29) yields the nonlinear eigenvalue equations as follows

$$\left(K_L + \frac{1}{2}K_{NL1} + \frac{1}{3}K_{NL2}\right)U_d^* - M\omega^2 U_d^* = 0 \quad (5.30)$$

To solve the resulting system of nonlinear eigenvalue Eq. (5.30), an iterative procedure should be used. For this purpose, in the first step, the nonlinear terms due to the transverse displacement are neglected, and the resulting eigenvalue problem is solved in each case. In the second step, the eigenvector is appropriately scaled up such that the maximum transverse displacement is equal to the given vibration amplitude w_{max} . Then, the eigenvalue problems are solved again to obtain the new eigenvalues and eigenvectors. In the third step, the eigenvector is scaled up again and step 2 is repeated until the relative error between the eigenvalues obtained from two consecutive iterations is within 0.1%.

5.5 Results and discussion

5.5.1 Verification

In the numerical results, nonlinear free vibration analysis of the FGS-CNTR Timoshenko beam with different boundary conditions is investigated. Here, we consider PMMA, referred to Polymethyl methacrylate, as the matrix ($E_m=2.5 \text{ GPa}$, $\rho=1190 \text{ kg/m}^3$) and (10, 10) SWCNT as the

reinforcement (see table 5.1):

Table 5. 1 Material properties of equivalent fiber [136]

Mechanical properties	CNT
Longitudinal Young's modulus	5.456 (TPa)
Transverse Young's modulus	1.010 (TPa)
Longitudinal shear modulus	0.431 (TPa)
Poisson's ratio	0.175 (TPa)

Before starting numerical studies, to establish the accuracy of the present formulation and the computer program developed by the author, results obtained from the present study are compared with the available results in the literature. The nonlinear fundamental frequencies of CNTR beam ($\eta=L/h=1$, $h=0.1$) is compared with data presented in Ref. [129]. Table 5.2 shows that the present results are in good agreement with the results of Wang et al. [129]. The parameter used in this example are $E^m = 2.5 \text{ GPa}$, $\nu^m = 0.34$, $\rho^m = 1190 \text{ Kg/m}^3$ for matrix, and the armchair (10,10) SWCNTs are used as the reinforcements with $E_{11}^{cnt} = 600 \text{ GPa}$, $E_{22}^{cnt} = 10 \text{ GPa}$, $\nu^{cnt} = 0.19$ and $\rho^{cnt} = 1400 \text{ Kg/m}^3$.

Table 5. 2 Comparison of dimensionless nonlinear frequency ω_{nl} / ω_l for UD-CNTRC beams ($L/h=10$)

	V_{cnt}^*	Method	ω_l	W_{max}				
				0.1	0.2	0.3	0.4	0.5
C-C	0.12	[128]	1.6678	1.0154	1.0605	1.1318	1.2251	1.3381
		Present	1.6621	1.0142	1.0544	1.1143	1.1872	1.2748
	0.28	[128]	2.3634	1.0176	1.0687	1.1490	1.2544	1.3829
		Present	2.3420	1.0171	1.0646	1.1337	1.2157	1.3044
H-H	0.12	[128]	1.2576	1.0278	1.1070	1.2278	1.3791	1.5522
		Present	1.2551	1.0256	1.0952	1.1938	1.3083	1.4302
	0.28	[128]	1.8297	1.0299	1.1151	1.2439	1.4046	1.5874
		Present	1.8201	1.0299	1.1094	1.2065	1.3261	1.4525

5.5.2 Discussion

Before analyzing the vibration of FGS-CNTR beams, the effects of aggregation degree (μ and η) on the effective longitude Young's modulus of FG-CNTRC beam needs to be investigated Fig 5.4. Using the relations presented in previous sections, it is possible to observe the variations of the effective material properties through the thickness of the FGS-CNTR beam for different aggregation parameters. For this goal, a particular case of the FGS-CNTR beam is considered in which $h_f=0.35$, $h_c=0.3$ and $q=2$. The variations of Young's modulus of beams concerning the different aggregation parameters μ and $\eta=0.75$ are illustrated in Fig 5.4. As expected, at a constant value of z/h ratio, with the increase of parameter μ ($\mu < \eta$), the effective Young's modulus increases. Fig 5.4 represents the fact that the highest values of Young's modulus are attained for the aggregation state of $\eta=\mu=0.75$ (fully dispersed), where the volume fraction of CNTs in the cluster

and the matrix are equal. As it is observed, when μ is less than η ($\mu < \eta$), the effective Young's modulus increases with increasing the value of μ and has the maximum amount when the CNTs are uniformly dispersed in the composite, i.e., $\mu = \eta$. So, it is undeniable that the aggregation parameters have significant effects on the material properties. Therefore, one can come to this conclusion that CNTs aggregation plays an essential role in vibrational characteristics of FGS-CNTR beams.

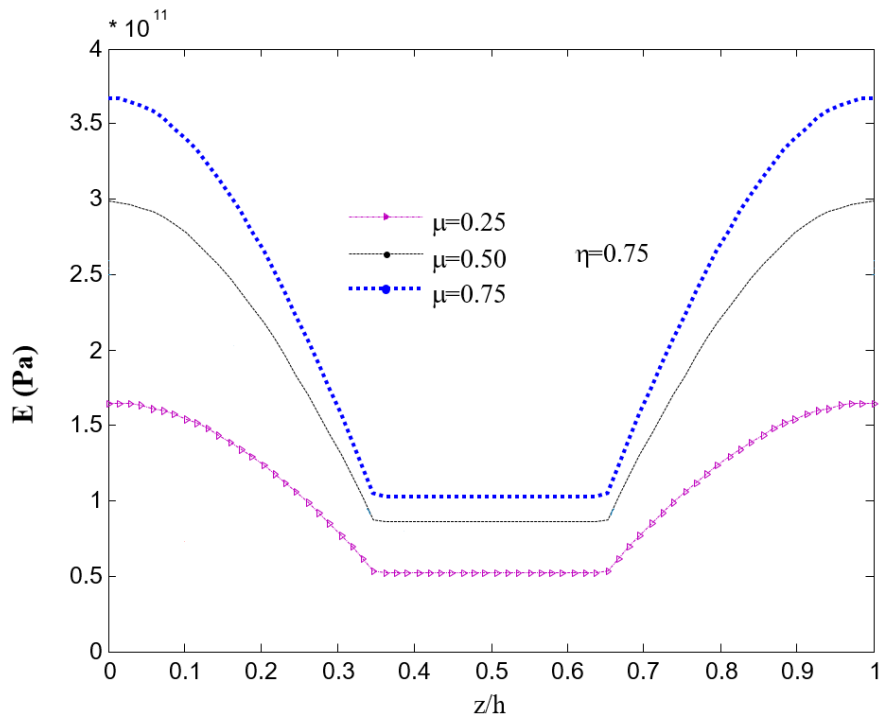


Figure 5. 4 The variation of Young's modulus and along the thickness of the FGS-CNTR beam with aggregation effect

Now, vibration analysis of FGS-CNTR beams rested on Pasternak foundation is studied using the MT approach. The thickness of the sandwich beam is 1 and kept unchanged in all numerical examples, whereas the thickness of core layer and face sheets change corresponding to the core-to-face sheet thickness ratio $h_c/h_f=2, 4, 8$. Also, to be close to the reality, the amount of q in most cases considered 1 and 50 which shows the linear and uniform distribution of CNT in the

face sheets respectively (Fig 5.3).

Tables 5.3-5.5 show effects of the elastic foundation coefficients and different values of core-to-face sheet thickness ratio ($h_c/h_f=2, 4$) on the dimensionless nonlinear and linear vibration of various types of CNTRC sandwich beams for different boundary conditions. By increasing q which leads to increasing the volume fraction of CNT on the face sheets, both linear and nonlinear frequencies of beam will increase. It can be seen that among the three boundary conditions considered, the clamped-clamped beam has the maximum values of linear and nonlinear frequencies. Also, it can be inferred that with increasing the h_c/h_f ratio, the frequency decreases. This justifies by the fact that reduces of the thickness of face sheets will result in decreases of CNT volume fraction value, so it becomes softer. It is also observed, the frequency (both linear and nonlinear) of the beams increases when resting on elastic foundations. It happens because the beam becomes stiffer with elastic foundations.

Table 5. 3 Nonlinear frequency ω_{nl} for C-C CNTRC sandwich beams ($L/h=10, q=1, V_i=0.05, V_o=0.1, \eta=0.4, \mu=0.4$)

(k_w, k_s)	h_c/h_f	ω_l	q=1			ω_l	q=100		
			$w_{max}=0.1$	0.3	0.5		$w_{max}=0.1$	0.3	0.5
(0,0)	2	2.2869	2.2928	2.3396	2.4293	2.5346	2.5411	2.5919	2.6894
	4	2.1863	2.1888	2.2457	2.3459	2.4139	2.4165	2.4756	2.5584
(0.1,0)	2	2.3083	2.3109	2.3316	2.3728	2.5539	2.5603	2.6108	2.7076
	4	2.2087	2.2112	2.2676	2.3668	2.4342	2.4368	2.4954	2.5989
(0.1,0.2)	2	2.7680	2.7728	2.8107	2.8840	2.9758	2.9784	2.9986	3.1071
	4	2.6856	2.6909	2.7326	2.8131	2.8737	2.8794	2.9243	3.0108

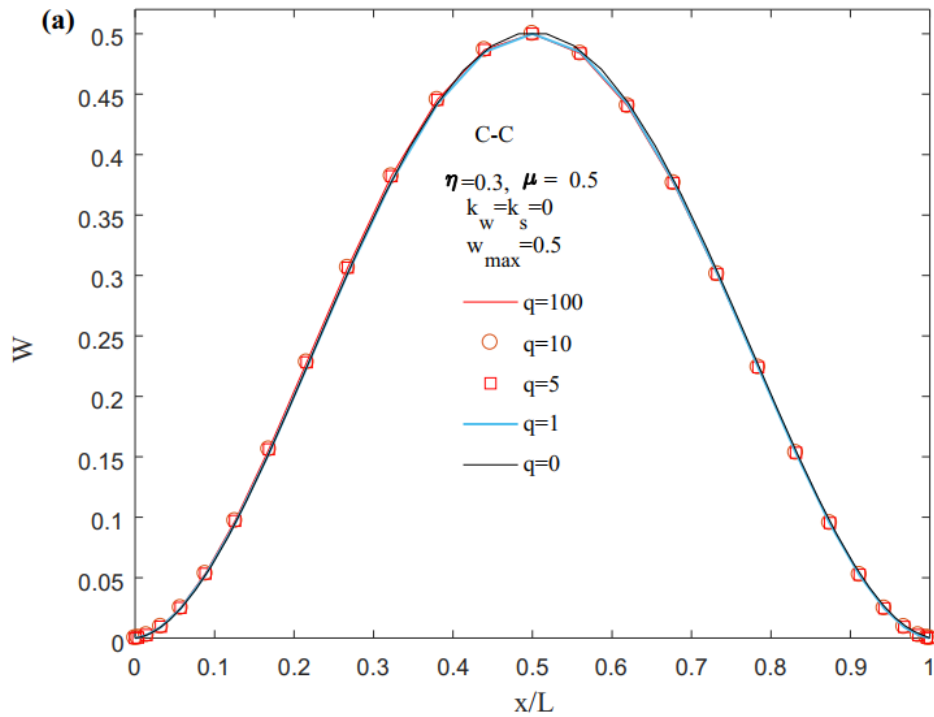
Table 5. 4 Nonlinear frequency ω_{nl} for H-H CNTRC sandwich beams ($L/h=10, q=1, V_i=0.05, V_o=0.1, \eta=0.4, \mu=0.4$)

(k_w, k_s)	h_c/h_f	ω_l	q=1			ω_l	q=100		
			$w_{max}=0.1$	0.3	0.5		$w_{max}=0.1$	0.3	0.5
(0,0)	2	1.0381	1.0497	1.1360	1.2934	1.1502	1.1641	1.2677	1.4424
	4	0.9918	1.0044	1.0974	1.2532	1.0958	1.1105	1.2083	1.3746
(0.1,0)	2	1.0845	1.0951	1.1798	1.3438	1.1921	1.2056	1.3059	1.4761
	4	1.0404	1.0524	1.1414	1.2920	1.1399	1.1540	1.2484	1.4100
(0.1,0.2)	2	1.7668	1.7744	1.8329	1.9396	1.8337	1.8425	1.9100	2.0324
	4	1.7404	1.7486	1.8086	1.9059	1.8009	1.8079	1.8702	1.9856

Table 5. 5 Nonlinear frequency ω_{nl} for C-H CNTRC sandwich beams ($L/h=10, q=1, V_i=0.05, V_o=0.1, \eta=0.4, \mu=0.4$)

(k_w, k_s)	h_c/h_f	ω_l	q=1			ω_l	q=100		
			$w_{max}=0.1$	0.3	0.5		$w_{max}=0.1$	0.3	0.5
(0,0)	2	1.9060	1.9207	2.0300	2.2142	2.1110	2.1247	2.2209	2.4575
	4	1.8218	1.8368	1.9475	2.1313	2.0106	2.0237	2.1354	2.3216
(0.1,0)	2	1.9316	1.9462	2.0542	2.2363	2.1342	2.1499	2.2674	2.4661
	4	1.8487	1.8634	1.9727	2.1544	2.0349	2.0497	2.1597	2.3458
(0.1,0.2)	2	2.4611	2.4708	2.5454	2.6791	2.6235	2.6351	2.7233	2.8797
	4	2.3963	2.4057	2.4780	2.6074	2.5431	2.5535	2.6329	2.7748

It is clear that when $V_i=0$ the amount of CNT volume fraction in the substrate is equal to zero, so we have sandwich beams with CNTRC face sheets with different CNT volume fractions V_{CN} and when $V_i \neq 0$ the substrate is consist of CNT. As mentioned before, when $q=0$ the CNT has a uniform distribution of volume fraction through the thickness of the beam in case of $V_i \neq 0$ and CNT volume fraction is equal to zero in case of $V_i=0$. So, it becomes possible to compare the CNTR sandwich beam with a regular CNTR beam and beam without CNT. Fig 5.5 presents nonlinear fundamental mode shapes for CNTRC beams with various q at $w_{max}=0.5$. It is found that



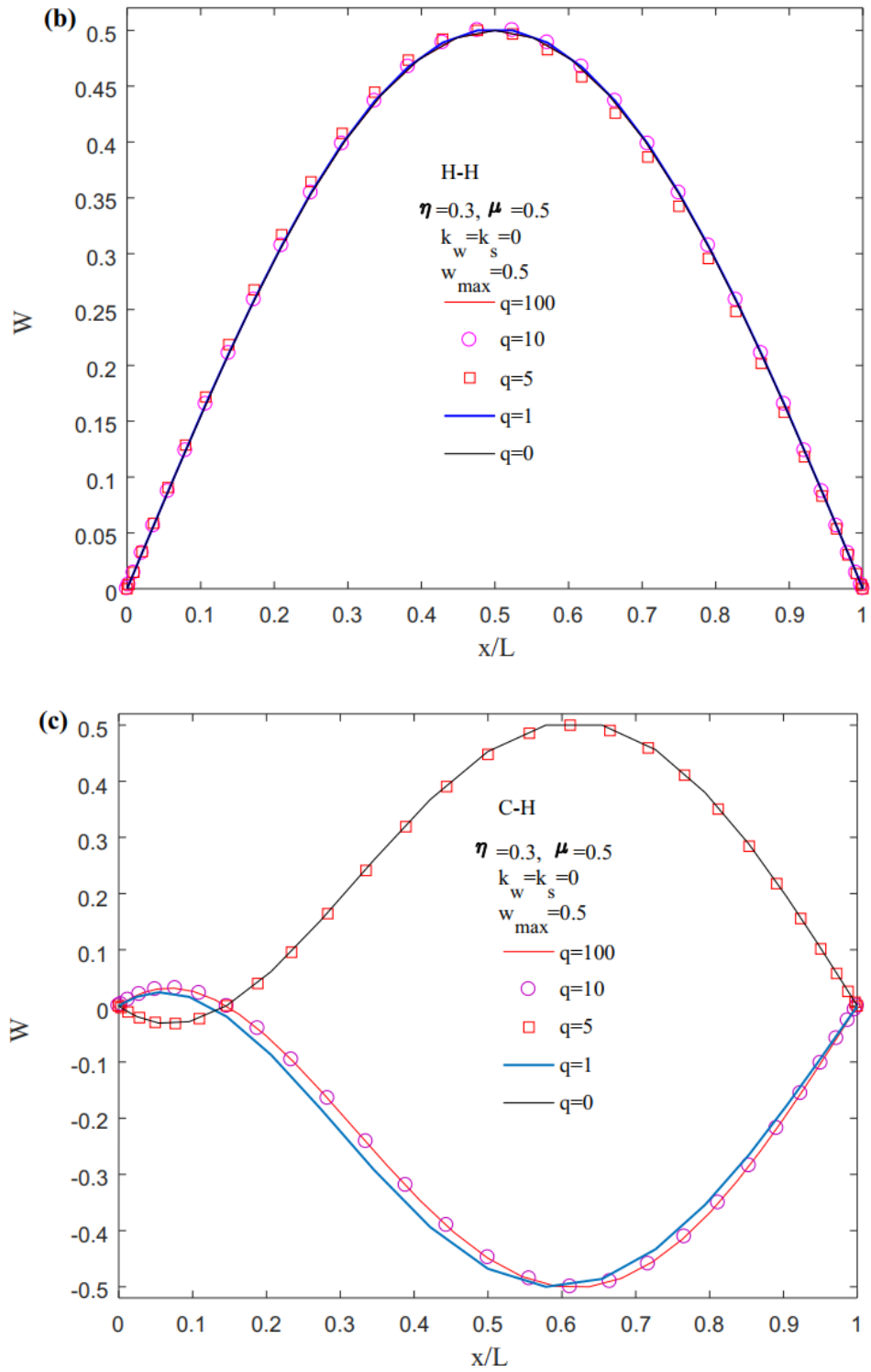


Figure 5. 5 Nonlinear mode shapes of CNTRC sandwich beams at $w_{max}=0.5$ and $L/h=15$: (a) C-C, (b) H-H and (c) C-H ($V_i=0.05, V_o=0.1$)

the nanotube volume fraction V_{cnt} has an insignificant effect on the nonlinear mode shape for all beams. The maximum amplitude occurs at the midpoint of the H–H and C–C beams but not for the C–H beam.

The nonlinear fundamental mode shapes for the displacement W , are plotted in Fig 5.6 with various elastic foundation parameter at $w_{max}=0.5$. Note that $V_i=0$ shows that there is no CNT in the substrate and $q=1$ corresponds to the linear distribution of CNT on the face sheets. The maximum displacement approaches the center of the beam as we increase the elastic foundation stiffness.

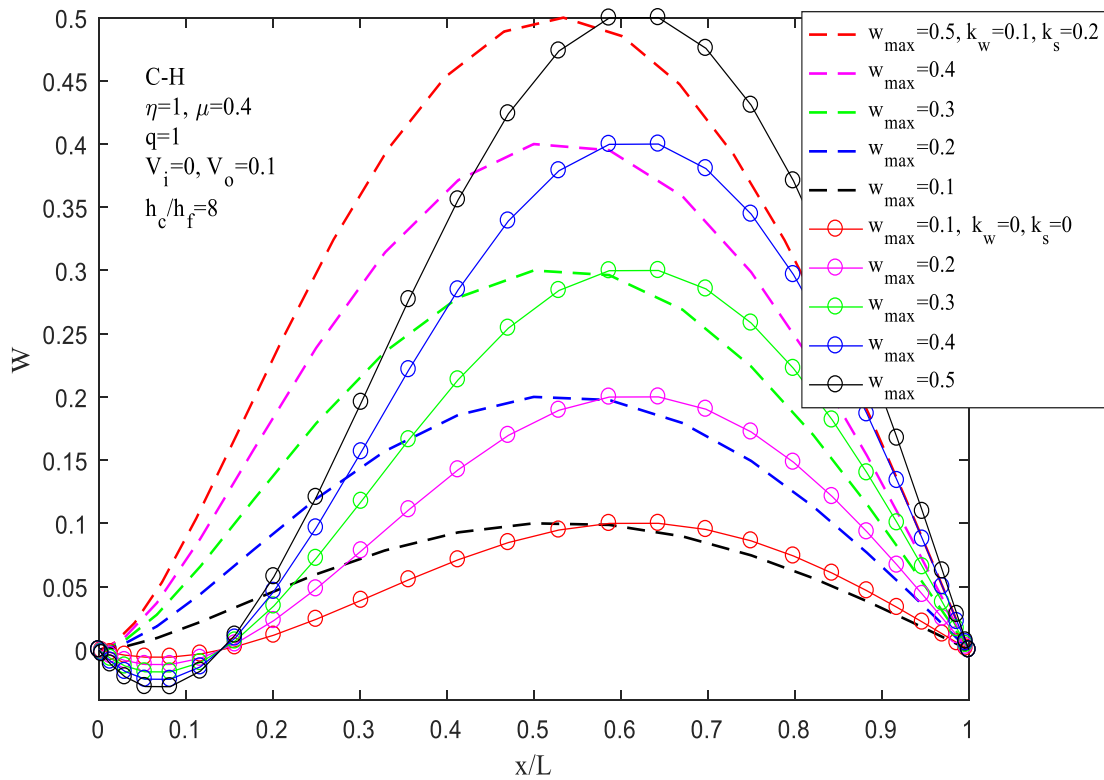


Figure 5. 6 Nonlinear mode shapes of CNTRC sandwich beams at $L/h=15$ for C–H boundary condition

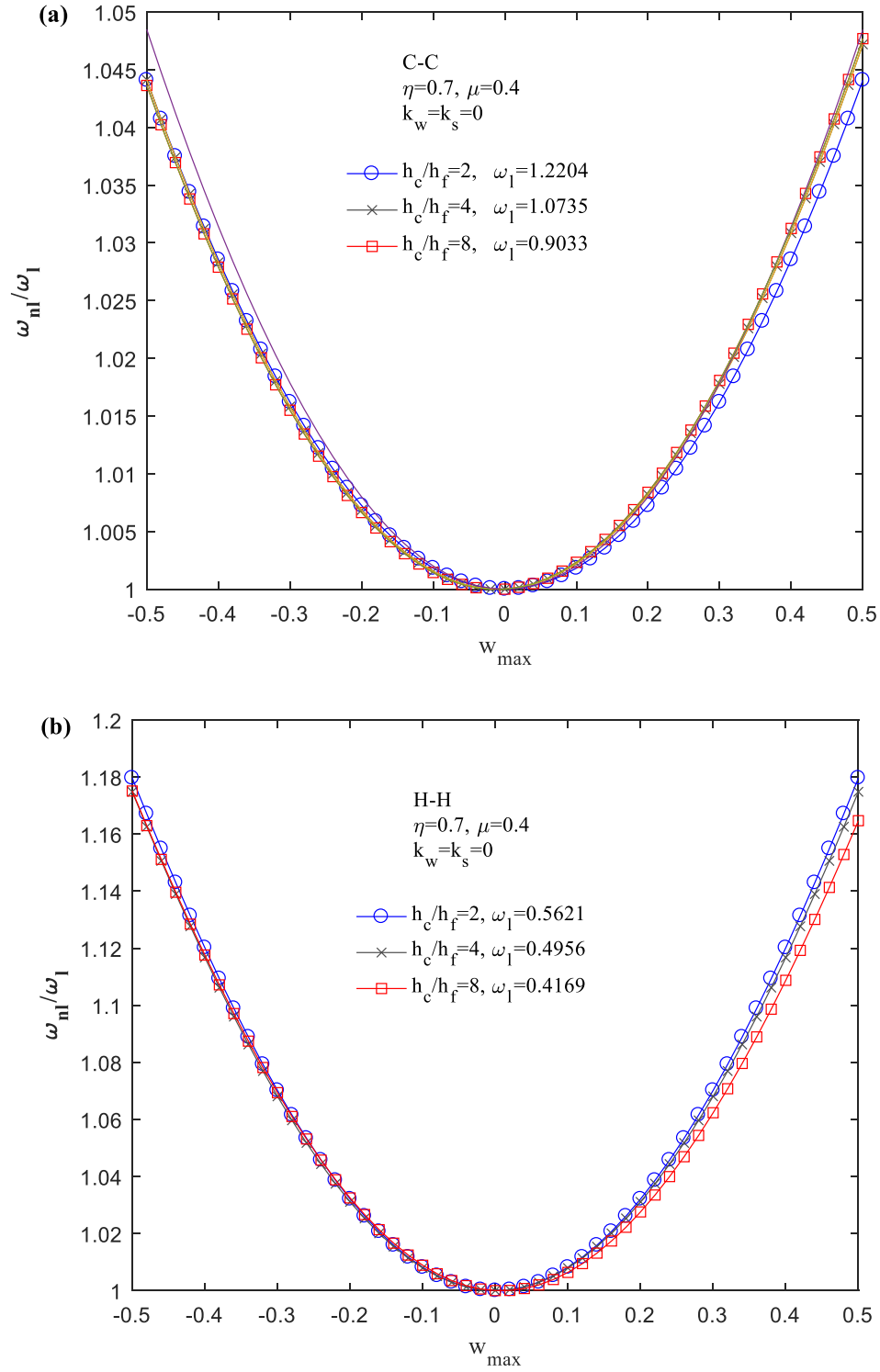


Figure 5. 7 Effect of core thickness on the nonlinear frequency ratio versus dimensionless amplitude curves of the CNTRC beams with $q=1$ $V_i=0$, $V_o=0.05$ and $L/h=15$ (a) C–C, (b) H–H

Figure 5.7 shows the effect of the different values of core-to-face sheet thickness ratio ($h_c/h_f = 2, 4, 8$) on the dimensionless nonlinear and linear vibration of various types of CNTRC sandwich beams when $V_i=0$, $V_o=0.05$, $q=1$ and $L/h=15$. Results show that an increase in the h_c/h_f significantly reduces the linear frequency for both boundary conditions (C-C and H-H) but slightly decrease the nonlinear frequency ratio for H-H boundary conditions and it has an opposite trend for C-C boundary condition.

In Fig 5.8, we find that fully dispersal of the randomly oriented CNTs (clustered, $\eta=\mu=0.4$ and $\eta=\mu=0.9$) results in the highest linear fundamental frequency, while an aggregated state would have a lower frequency ($\eta=0.4, \mu=0.1$ and $\eta=0.9, \mu=0.1$). That is because aggregates have lower modulus than individual dispersed CNTs and thus reduced reinforcing efficiency. But for dimensionless nonlinear frequency (ω_{nl} / ω_l), it is essential to consider both linear and nonlinear frequency. Fully dispersed CNT leads to both bigger linear and nonlinear frequencies but a lower nonlinear frequency ratio.

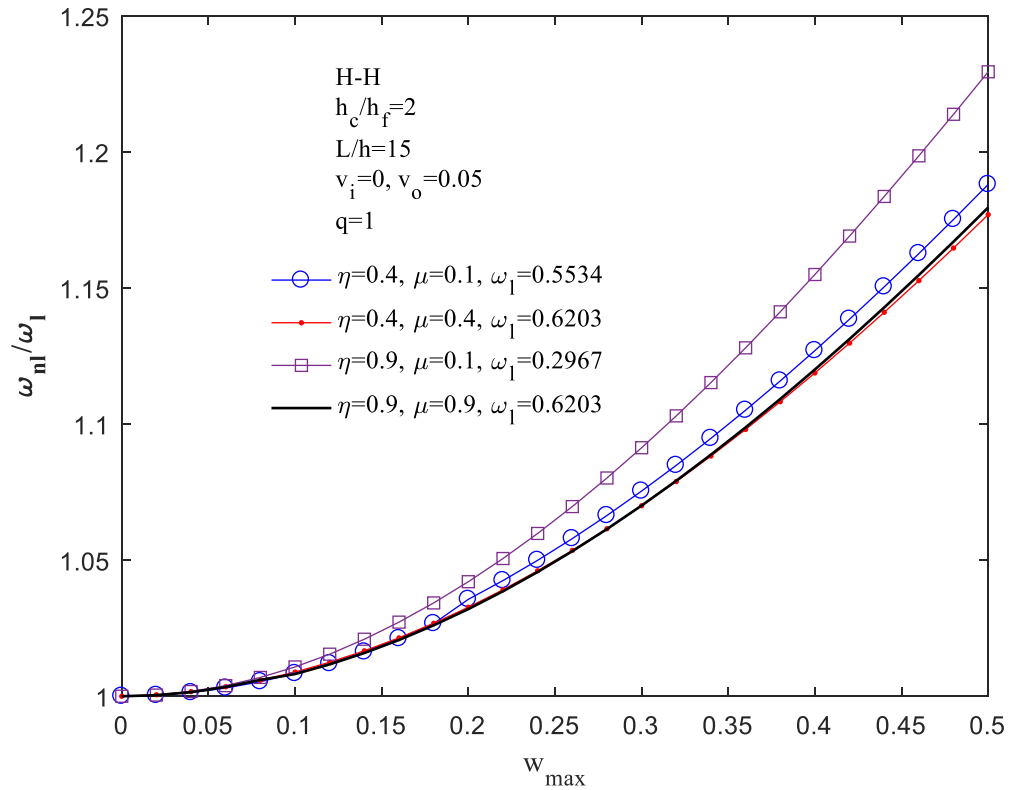


Figure 5. 8 Effect of state of aggregation on the nonlinear frequency ratio versus dimensionless amplitude curves of the CNTRC beams with $q=1$

5.6 Conclusion

The nonlinear free vibration of FG-CNTR sandwich beams rested on Pasternak foundation is studied based on Timoshenko beam theory and by applying von Kármán geometric nonlinearity. The effective material properties of the nanocomposite beam are assumed to be graded in the thickness direction and estimated by the Mori–Tanaka approach. The GDQ method and a direct iterative approach is employed to obtain the nonlinear vibration frequencies and mode shapes of FG-CNTRC beams with different boundary conditions. Results present this fact that mechanical properties and therefore vibration of FG-CNTR sandwich beams are severely affected by CNTs aggregation. It can be concluded from Numeric results that CNT volume fraction, aggregation

state, core-to-face sheet thickness ratio (h_c/h_f) and end supporting conditions play an important role on the nonlinear frequencies and mode shapes. Also, it is seen that both Winkler and Pasternak elastic coefficients play effective roles in both frequency and mode shape.

Chapter 6:

Effect of hyperbolic heat conduction on the linear and nonlinear vibration of CNT reinforced size-dependent functionally graded microbeams⁵

As a first attempt, the combined application of the differential quadrature method (DQM) and the Newton Raphson method is used to solve the hyperbolic (non-Fourier) heat conduction equations to obtain temperature, displacements and nonlinear frequency in the functionally graded (FG) nanocomposite Timoshenko microbeam. To do so, we need to follow two steps: (1): solving the hyperbolic heat conduction to obtain the temperature in the spatial and temporal domains by using DQM and Newton Raphson method; (2): implementation of the obtained temperature in thermoelastic equations of microbeam to obtain displacements and frequency at each time step by direct iterative method. The material length scale parameter is introduced in the non-classical Timoshenko beam model, to interpret the size effect in microstructures. The material properties of the FG nanocomposite beam are estimated using the Eshelby–Mori–Tanaka approach and carbon nanotubes (CNTs) are randomly distributed within the composite. The nonlinear governing equations and boundary conditions are derived using the Hamilton principle and von Kármán geometric nonlinearity. A direct iterative method is employed to determine the nonlinear frequencies and mode shapes of the beams. All material properties such as Young modulus (E),

⁵ A version of this chapter is published in International Journal of Engineering Science 137, 57-72, 2019.

heat capacity (C_p), relaxation time (τ), density (ρ) and thermal conductivity (K) are considered as a function of temperature and CNT volume fraction. The effects of temperature change, thermal conductivity, CNTs volume fraction, length to span ratio, heat wave speed, heat flux, and end support conditions on the nonlinear vibration of the beam are discussed in detail. Unlike all previous publications, the present results show that increasing thickness-to-length scale ratio (h/l) will increase the frequency.

6.1 Introduction

In recent years, CNTs have attracted more and more attention from researchers for their excellent mechanical properties. It is well known that the addition of CNTs in a matrix can improve the thermal and physical behaviors significantly. These outstanding properties of CNTs [53-55,107] have stimulated researchers to exploit them as a new generation of reinforcing agents for polymers. Numerous studies have been made to analytically and experimentally determined the mechanical properties of CNT reinforce nanocomposites via molecular dynamics (MD) simulation [60,108,109], continuum mechanics [61,62,110] and multi-scale simulation [59,63]. Seidel et al. [111] focused on the obtain effective elastic properties of composites consisting of aligned single or multi-walled carbon nanotubes embedded in a polymer matrix. They also investigated the effect of an interphase layer between the nanotube and the polymer matrix as a result of functionalization. For the same reasons mentioned above, CNTs have received increased attention as reinforcements for polymer composites.

Fourier heat conduction is not applicable to engineering problems with small spatial or temporal scale, as a result during the past few years, considerable attention has been paid to the non-Fourier heat conduction in problems with shallow temperatures, extremely short period, or very high heat flux; see, for example, [32,33]. Then a modified flux model for the heat transfer

processes with a finite speed thermal wave is suggested. The hyperbolic heat conduction equation based on the Cattaneo model for the heat flux incorporates a relaxation mechanism to adjust a change in the temperature gradient gradually. This model has been a satisfactory extension of classical diffusion theory and can yield the hyperbolic diffusion equation within the continuum assumption [137]. Rahideh et al. [10] used the layerwise-incremental differential quadrature method (LIDQM) to show the effect of heat wave speed on the thermal characteristics of a multi-layered domain made of functionally graded materials.

The macro-mechanical properties of nanocomposites are affected by the microstructure and volume fraction of CNTs. Several methods are used to evaluate the effective properties of nanocomposites [112-115].

The Mori–Tanaka (MT) model is one of the best known analytical approaches to determine the effective material constants of composite materials. Barai [117] developed a two-scale micromechanical model to analyze the effect of CNT aggregation and interface condition on the plastic strength of CNT/matrix inclusions, and the small-scale property of the clustered inclusions.

From the literature review, it is noted that the thermal effect on nonlinear and linear vibrations of microscale structures has been an object of many studies. However, the vibration properties of CNT-reinforced functionally graded composite microbeams under transient heat conduction along with considering the size effect have not been studied yet. In the present work, we have presented the vibration behaviors of CNT-reinforced functionally graded microbeam under the action of hyperbolic heat conduction.

Thai and Choi [138] presented size-dependent models for bending, buckling and vibration of FGM Kirchhoff and Mindlin plates using the modified couple stress theory. A two-dimensional elasticity approach was developed by Xiang and Yang [127], using the differential quadrature

method to obtain the free and forced vibration characteristics of laminated FG Timoshenko beam of variable thickness. The beam consists of a homogeneous substrate and two inhomogeneous functionally graded layers, subjected to one-dimensional steady heat conduction in the thickness direction. Ke et al. [128] analyzed the nonlinear vibrations of FG-CNTRC Timoshenko beams with symmetric and unsymmetrical distributions of CNTs along the thickness direction using Ritz method and direct iterative technique. Also, based on the modified couple stress theory, they [139] investigated the free vibration and buckling of microbeams with the effect of the temperature change and scale parameter. They showed that the thermal effect on the fundamental frequency is mild when the thickness of the microbeam has similar value to the material length scale parameter but becomes significant when the thickness of the microbeams becomes larger.

This paper is focused on the effect of hyperbolic heat conduction on the linear and nonlinear free vibration of FG-CNT reinforced beams. As a first attempt, non-Fourier heat conduction in the cylindrical panel with temperature-dependent material properties is studied. Then a mathematical model is developed for considering the effect of transient heat conduction on the vibration analysis of nanocomposite beam using DQM. Nonlinear free vibration analysis of FG-CNT reinforced composite structures is studied based on Timoshenko beam theory using Hamilton's principle, MT model, and GDQ method which is found to be a simple and efficient numerical technique for solving partial differential equations [80,89,130,131]. The effects of CNTs volume fraction and distribution on the frequency and vibration responses of the beam will be studied as well as hyperbolic heat conduction. Unlike all previously published papers, the present results show that increasing the thickness (h) will increase the frequency while the length scale parameter is constant (l). This is true since thermal force is a function of thickness, and the temperature is dependent on the thickness. In the thermal boundary condition considered in this

paper, increasing h will result in increasing thermal force, which in turn, leads to increasing linear and nonlinear frequency. The thermal force should be obtained all over again as we change the thickness of the beam.

6.2 Hyperbolic (Non-Fourier) heat conduction

The structure of the beam is shown in Fig 6.1.

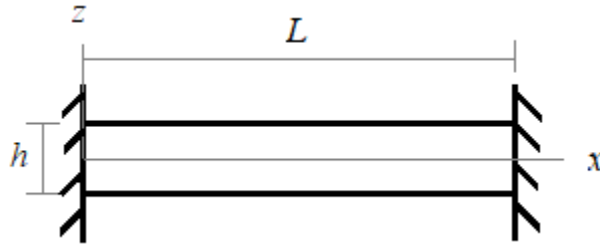


Figure 6. 1 Geometry of the microbeam

The hyperbolic constitutive relation governing the transient heat transfer is as follows.

$$\tau \frac{\partial q}{\partial t} + q = -k \frac{\partial T}{\partial x} \quad (6.1)$$

where τ is the relaxation time. The relaxation time depends on the mechanism of heat transport and represents the time lag needed to establish steady-state heat conduction in an element of volume when a temperature gradient is suddenly applied to that element. It is related to the thermal

wave speed and thermal diffusivity as $\tau = \frac{\alpha}{C^2}$. Moreover, the energy equation can be written as,

$$\rho C_p \frac{\partial T}{\partial t} + \frac{\partial q}{\partial x} = g(z, t) \quad (6.2)$$

The DQM is used to discretize the spatial derivatives. Also, the incremental DQM is employed to discretize the temporal domain. Based on this approach, the total temporal domain is divided into a set of time intervals where the DQ rule is employed to discretize the temporal

derivatives. At the end of each time interval, the temperature and heat flux is used as the initial condition for the next time interval.

The DQ method being applied to Eqs. (6.1, 6.2), the following equations at an arbitrary sampling point z_i and t_j are then obtained:

$$k_{ij} \left(\sum_{m=1}^{N_x} C_{im}^1 T_{mj} \right) + \tau_{ij} \left(\sum_{n=1}^{N_t} D_{jn}^1 q_{in} \right) + q_{ij} = 0 \quad (6.3)$$

$$\left(\sum_{m=1}^{N_x} C_{im}^1 q_{mj} \right) + \rho_{ij} (C_p)_{ij} \left(\sum_{n=1}^{N_t} D_{jn}^1 T_{in} \right) = g_{ij} \quad (6.4)$$

Finally one obtains a system of nonlinear algebraic equations in each time interval which is solved using the Newton–Raphson method, and the procedure is repeated for all time intervals.

Consider the beam is under a sudden temperature change on the lower surface. From Fig 6.1, the boundary conditions of the problem can be expressed as [49,50]

$$\begin{cases} T(z_i, t) = \begin{cases} \frac{1}{2} + \frac{3}{4} \left(\frac{2t}{t^*} - 1 \right) - \frac{1}{4} \left(\frac{2t}{t^*} - 1 \right)^3 & \text{if } 0 \leq t \leq t^* \\ 1 & \text{if } t \geq t^* \end{cases} \\ T(z, 0) = 0 \\ q(z_o, t) = 0 \\ q(z, 0) = 0 \end{cases} \quad (6.5)$$

A heating pulse is applied to the inner surface of the plate in which t^* is equal to 0.005 s unless otherwise mentioned. The main goal of this example is to predict the propagation of the thermal disturbance as it is shown in Fig 6.2. The convergence of the presented DQM is shown in this figure. The same value for the parameters as those in the work of Dorao [50] is considered here. The results for convergence behavior of the time history and spatial distribution of the nondimensional temperature and heat flux are presented here. It is clear that by increasing the number of sample points in both temporal and physical domains ($N=N_z=N_t$), followed by

decreasing the time interval, converged results are obtained. It should be noted that $N*dt =$ constant. The whole process is investigated in the same amount of time for all the tests.

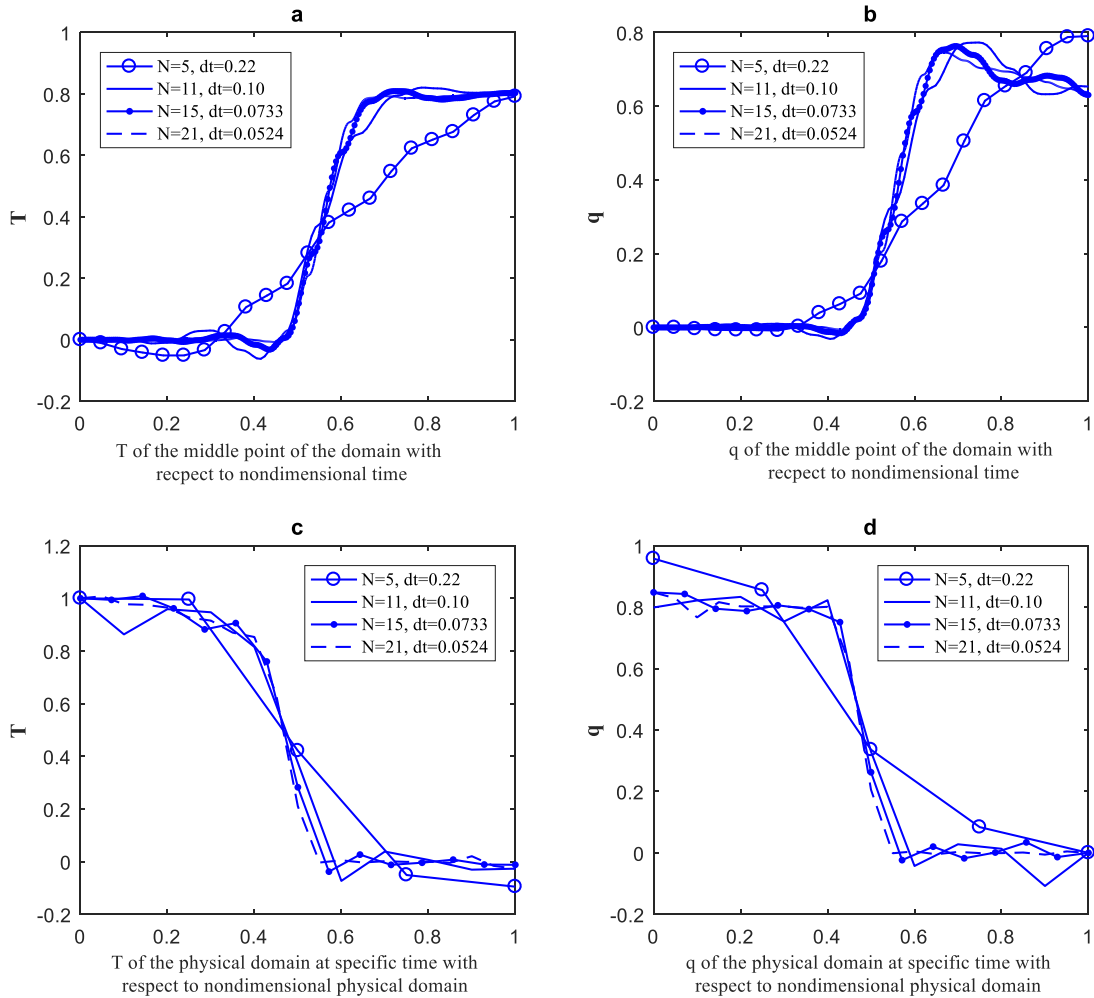


Figure 6. 2 Convergence study of the presented DQM ($t^* = 0.2$).

For further validation, the proposed method has been compared with the experimental results [139] as shown in Fig 6.3, with the parameters shown in Table 6.1. Fourier heat conduction cannot capture the time lag, so boundary conditions' affect the whole media constantly. Consequently, there will be no jump in the temperature history. On the other hand, hyperbolic heat conduction and experimental results are almost the same which approves using the hyperbolic heat

conduction in CNT reinforced composites.

Table 6. 1 Material properties of the specimen [139]

	Value	Unit
Thermal conductivity (K)	0.8 ± 0.04	$W/m.K$
Density (ρ)	1230 ± 10	Kg/m^3
Specific heat (C)	4.66 ± 0.20	$kJ/kg.K$
Thermal diffusivity (α)	$1.40 * 10^{-7} \pm 0.12 * 10^{-7}$	M^2/s
Time lag (τ)	15.24	S

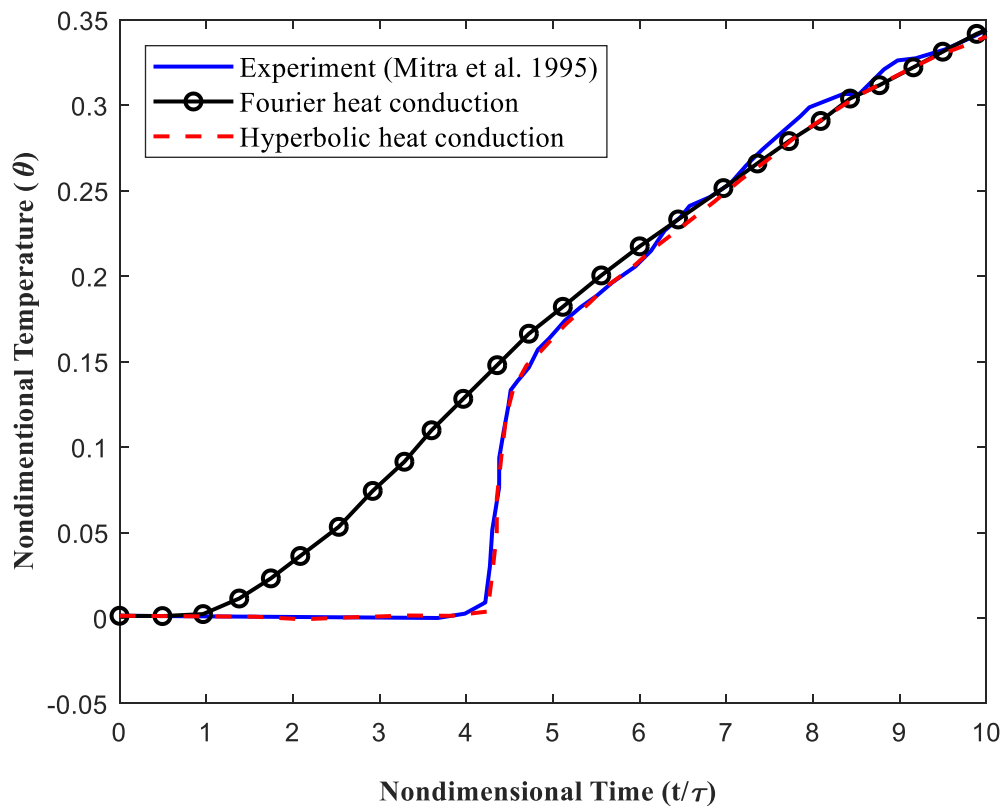


Figure 6. 3 Comparison of solving techniques with results available in the literature [139] (Fourier, hyperbolic and experimental data).

In the next part, a heating pulse is applied to the lower boundary of a parallel sided slab.

The initial and boundary conditions are

$$\begin{cases} q(z_i, t) = \begin{cases} -1 + \left(\frac{2t}{t^*} + 1\right)^{2/3} & \text{if } 0 \leq t \leq t^* \\ 0 & \text{if } t \geq t^* \end{cases} \Rightarrow \\ q(z, 0) = 0 \\ q(z_o, t) = 0 \\ T(z, 0) = 0 \end{cases} \quad (6.6)$$

6.3 Thermal conductivity (K), relaxation time (τ) and heat capacity (C_p) of CNT

Thermal conductivities of the random and aligned CNT reinforced composites are calculated as a function of the volume fraction of CNTs. Thermal conductivity is greatly improved as the volume fraction of CNTs increases in both random composites and aligned composites [140].

Second-order polynomial equations are used to obtain the thermal conductivity as follow:

$$K_R = 51.9V_{cn}^2 + 0.43V_{cn} + 0.64 \quad (6.7)$$

$$K_A = 90.9V_{cn}^2 + 4.35V_{cn} + 0.77 \quad (6.8)$$

in which K_R and K_A referred to the thermal conductivities of randomly distributed CNT and aligned CNT. Clearly, for a specific volume fraction of CNTs, K_A is bigger than K_R , which leads to the faster motion of heat waves in the media [75]. To approach the reality, just the composite with a random distribution of CNTs is considered.

Since the relaxation time of CNTs is hugely smaller than the relaxation time of the matrix, we can use case 1 as an example. The length of CNTs does not play an important role in heat conduction when the relaxation time of the matrix is relatively high.

The specific heat capacity (C_p) of a CNT as a function of temperature is stated in Hepplestone et al. [76]. They showed that increasing temperature would increase the specific heat capacity C_p by approximately a constant amount as follow:

$$C_p = aT + b \quad (6.9)$$

with $a = 2.5642$ ($J/(kg \cdot K)$) and $b = -61.7294$ ($J/(kg \cdot K)$).

6.4 Composites reinforced with randomly oriented, straight CNTs

The effective properties of composites with randomly oriented non-clustered CNTs, such as in Fig 6.4, are studied in this section. The resulting effective properties for the randomly oriented CNT composite are isotropic, despite the CNTs having transversely isotropic effective properties. Two Euler angles α and β characterizes the orientation of a straight CNT, as shown in Fig 6.3. When CNTs are entirely randomly oriented in the matrix, the composite is then isotropic, and its bulk modulus k and shear modulus G is derived as [77,78,133]

$$k(t) = k_m + \frac{f_r(\delta_r(t) - 3K_m\alpha_r(t))}{3(f_m + f_r\alpha_r(t))} \quad (6.10)$$

$$G(t) = G_m + \frac{f_r(n_r(t) - 2G_m\beta_r(t))}{2(f_m + f_r\beta_r(t))}$$

where

$$\alpha_r(t) = \frac{3(K_m + G_m) + k_r(t) - l_r(t)}{3(G_m + k_r(t))} \quad (6.11)$$

$$\beta_r(t) = \frac{1}{5} \left\{ \frac{4G_m + 2k_r(t) + l_r(t)}{3(G_m + k_r(t))} + \frac{4G_m}{G_m + p_r(t)} + \frac{2[G_m(3K_m + G_m) + G_m(3K_m + 7G_m)]}{G_m(3K_m + G_m) + m_r(3K_m + 7G_m)} \right\} \quad (6.12)$$

$$\delta_r(t) = \frac{1}{3} \left[n_r(t) + 2l_r(t) + \frac{(2k_r(t) + l_r(t))(3K_m + 2G_m - l_r(t))}{G_m + k_r(t)} \right] \quad (6.13)$$

$$\eta_r(t) = \frac{1}{5} \left[\frac{2}{3} (n_r(t) - l_r(t)) + \frac{8G_m p_r(t)}{G_m + p_r(t)} + \frac{8m_r G_m (3K_m + 4G_m)}{3K_m (m_r(t) + G_m) + G_m (7m_r(t) + G_m)} + \frac{2(k_r(t) - l_r(t))(2G_m + l_r(t))}{3(G_m + k_r(t))} \right] \quad (6.14)$$

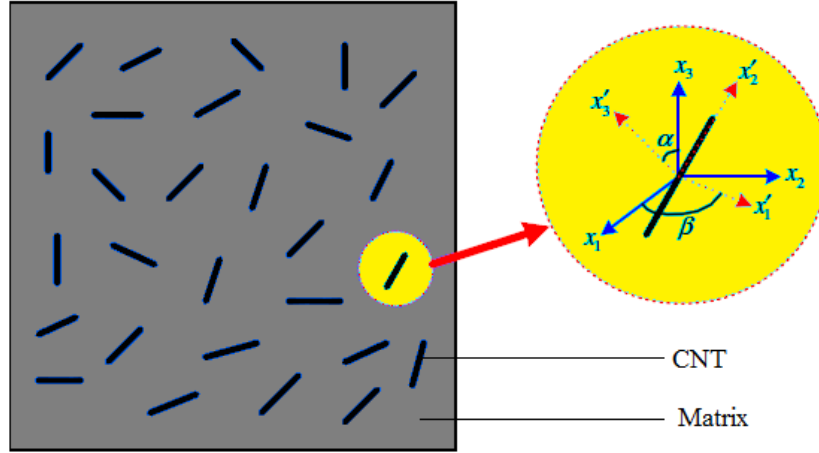


Figure 6. 4 Representative volume element (RVE) with randomly oriented, straight CNTs

The effective Young's modulus E and Poisson's ratio ν of the composite, which are related to time, are given by:

$$E(t) = \frac{9K(t)G(t)}{3K(t) + G(t)} \quad (6.15)$$

$$\nu(t) = \frac{3K(t) - 2G(t)}{6K(t) + 2G(t)} \quad (6.16)$$

Consider an FG-CNT reinforced beam as shown in Fig 6.1. In the present work, V_{CN} and V_m are considered as the CNT and matrix volume fraction, respectively. We assume for the FG beam, the volume fraction of the CNT is given by the power-law-type function:

$$V_{CN}(z) = V_i + (V_o - V_i) \left(\frac{z}{h} \right)^q \quad (6.17)$$

where q is the volume fraction index ($0 \leq q \leq \infty$), h is the thicknesses of the microbeam and V_o

and V_i , which have values ranging from 0 to 1, denote the maximum and minimum volume fractions of CNT that could exist in the thickness direction of the beam.

6.5 Equations of motion

Timoshenko beam theory is employed in this paper with the following displacement field to account for the effect of transverse shear strain which is important in the deformation of composite structures

$$U(x, y, z, t) = u_0(x, z, t) + z\psi(x, z, t) \quad (6.18a)$$

$$W(x, y, z, t) = w_0(x, z, t) \quad (6.18b)$$

in which u_0 and w_0 represent the components of displacement at section $z=0$, ψ is the rotational angle of the normal vector of the section about the y -axes, and t is time.

The nonlinear normal strain ε_x and shear strain γ_{xz} are associated with the displacements as:

$$\varepsilon_x = \frac{\partial u_0}{\partial x} + z \frac{\partial \psi}{\partial x} + \frac{1}{2} \left(\frac{\partial w_0}{\partial x} \right)^2, \quad \gamma_{xz} = \frac{\partial w_0}{\partial x} + \psi \quad (6.19)$$

Using the linear thermal elastic constitutive law, the normal stress σ_x and shear stress τ_{xz} are given by

$$\begin{aligned} \sigma_x(z) &= Q_{11}(z, T) \varepsilon_x \\ \tau_{xz}(z) &= Q_{55}(z, T) \gamma_{xz} \end{aligned} \quad (6.20)$$

in which

$$Q_{11}(z, T) = \frac{E(z, T)}{1 - \nu^2}, \quad Q_{55}(z, T) = \frac{E(z, T)}{2(1 + \nu)} \quad (6.21)$$

Employing Hamilton's principle, the equations of motion and the related boundary

conditions can be derived. According to Hamilton's principle

$$\delta \int_0^t (T - \Pi + \gamma_p) dt = 0 \quad (6.22)$$

where δ , T and Π denote variational symbol, the kinetic energy of the beam and potential energy composed of strain energy of the beam and the elastic potential energy of the elastic foundation respectively. It is worth noting that γ_p is the work done by external forces that are taken to be zero for free vibration analysis.

By setting the coefficients of δu , δw and $\delta \psi$ to zero leads to the equations of motion as

$$\delta u : \frac{\partial N_x}{\partial x} = I_1 \frac{\partial^2 u_0}{\partial t^2} + I_2 \frac{\partial^2 \psi}{\partial t^2} \quad (6.23a)$$

$$\delta w : \frac{\partial Q_x}{\partial x} + \frac{\partial}{\partial x} \left(N_x \frac{\partial w}{\partial x} \right) - K_f w_0 + K_s \frac{\partial^2 w_0}{\partial x^2} = I_1 \frac{\partial^2 w}{\partial t^2} \quad (6.23b)$$

$$\delta \Psi : \frac{\partial M_x}{\partial x} - Q_x = I_2 \frac{\partial^2 u_0}{\partial t^2} + I_3 \frac{\partial^2 \psi}{\partial t^2} \quad (6.23c)$$

where the resultant normal force N_x , bending moment M_x , and transverse shear force Q_x are calculated from

$$\begin{Bmatrix} N_x \\ M_x \\ Q_x \end{Bmatrix} = \int_{-h/2}^{h/2} \begin{Bmatrix} \sigma_{xx} \\ z \sigma_{xx} \\ \tau_{xz} \end{Bmatrix} dz = \begin{Bmatrix} A_{11} \left[\frac{\partial u_0}{\partial x} + \frac{1}{2} \left(\frac{\partial w_0}{\partial x} \right)^2 \right] + B_{11} \frac{\partial \psi}{\partial x} \\ B_{11} \left[\frac{\partial u_0}{\partial x} + \frac{1}{2} \left(\frac{\partial w_0}{\partial x} \right)^2 \right] + D_{11} \frac{\partial \psi}{\partial x} \\ k^* A_{55} \left(\frac{\partial w_0}{\partial x} + \psi \right) \end{Bmatrix} \quad (6.24)$$

In this study, the shear correction factor $k^* = \frac{5}{6}$ is used, and the stiffness components A_{11} ,

B_{11} , D_{11} , A_{55} of the beam are defined as:

$$\begin{aligned} (A_{11}, B_{11}, D_{11}) &= \int_{-h/2}^{h/2} Q_{11}(z)(1, z, z^2) dz, & A_{55} &= \int_{-h/2}^{h/2} Q_{55}(z) dz \\ (I_1, I_2, I_3) &= \int_{-h/2}^{h/2} \rho(z)(1, z, z^2) dz \end{aligned} \quad (6.25)$$

The work done by the force due to the influence of temperature change is $N_T(t) = -A_{11} \alpha \Delta T$

Different boundary conditions of the beams such as hinged-hinged (H-H), clamped-hinged (C-H), clamped-clamped (C-C), and clamped-free (C-F), can be considered. These conditions are described as:

$$\text{Clamped (C):} \quad u_0 = w_0 = \Psi = 0 \quad (6.26)$$

$$\text{Hinged (H):} \quad u_0 = w_0 = M_x = 0$$

Since we need to compare our results with the similar ones in the previous works, in the present study we used a beam with the hinged condition rather than simply supported beams. By using the following dimensionless quantities

$$\begin{aligned} \xi &= \frac{x}{L}, & (\bar{U}, \bar{W}) &= \frac{(u_0, w_0)}{h}, \\ (a_{11}, a_{55}, b_{11}, d_{11}) &= \left(\frac{A_{11}}{A_{110}}, \frac{A_{55}}{A_{110}}, \frac{B_{11}}{A_{110}h}, \frac{D_{11}}{A_{110}h^2} \right), \\ \psi &= \Psi, \quad \lambda = L/h, \quad l_0 = l/h, & (\bar{I}_1, \bar{I}_2, \bar{I}_3) &= \left(\frac{I_1}{I_{10}}, \frac{I_2}{I_{10}h}, \frac{I_3}{I_{10}h^2} \right) \end{aligned} \quad (6.27)$$

$$\tau = \frac{t}{L} \sqrt{\frac{A_{110}}{I_{10}}} \quad N_T^*(\tau) = N_T(t) \frac{A_{11}}{A_{110}}$$

$$a_{11} \left(\frac{\partial^2 u}{\partial \xi^2} + \frac{1}{\lambda} \frac{\partial w}{\partial \xi} \frac{\partial^2 w}{\partial \xi^2} \right) + b_{11} \frac{\partial^2 \psi}{\partial \xi^2} = \bar{I}_1 \frac{\partial^2 u}{\partial \tau^2} + \bar{I}_2 \frac{\partial^2 w}{\partial \tau^2} \quad (6.28a)$$

$$k^* a_{55} \left(\frac{\partial^2 w}{\partial \xi^2} + \lambda \frac{\partial \psi}{\partial \xi} \right) + \frac{a_{11}}{\lambda} \left(\frac{\partial^2 u}{\partial \xi} \frac{\partial^2 w}{\partial \xi^2} + \frac{3}{2\lambda} \left(\frac{\partial w}{\partial \xi} \right)^2 \frac{\partial^2 w}{\partial \xi^2} + \frac{\partial^2 u}{\partial \xi^2} \frac{\partial w}{\partial \xi} \right) + \frac{b_{11}}{\lambda} \left(\frac{\partial^2 \psi}{\partial \xi^2} \frac{\partial w}{\partial \xi} + \frac{\partial \psi}{\partial \xi} \frac{\partial^2 w}{\partial \xi^2} \right) + N_T^*(\tau) \frac{\partial^2 w}{\partial \xi^2} + S_1 = \bar{I}_1 \frac{\partial^2 w}{\partial \tau^2} \quad (6.28b)$$

$$b_{11} \left(\frac{\partial^2 u}{\partial \xi^2} + \frac{1}{\lambda} \frac{\partial w}{\partial \xi} \frac{\partial^2 w}{\partial \xi^2} \right) + d_{11} \frac{\partial^2 \psi}{\partial \xi^2} - k^* \lambda a_{55} \left(\frac{\partial w}{\partial \xi} + \eta \psi \right) + S_2 = \bar{I}_2 \frac{\partial^2 u}{\partial \tau^2} + \bar{I}_3 \frac{\partial^2 \psi}{\partial \tau^2} \quad (6.28c)$$

$$\text{Where } S_1 = \frac{l_0^2}{4\lambda} a_{55} \left(-\frac{1}{\lambda} \frac{\partial^4 w}{\partial \xi^4} + \frac{\partial^3 \psi}{\partial \xi^3} \right) \quad \text{and} \quad S_2 = \frac{l_0^2}{4} a_{55} \left(-\frac{1}{\lambda} \frac{\partial^3 w}{\partial \xi^3} + \frac{\partial^2 \psi}{\partial \xi^2} \right).$$

The associated boundary conditions can also be written in a dimensionless form as follows:

$$u = w = \psi = 0 \quad (6.29)$$

for a clamped-clamped (C-C) boundary condition,

and

$$u = w = b_{11} \left(\frac{\partial u}{\partial \xi} + \frac{1}{2\lambda} \left(\frac{\partial w}{\partial \xi} \right)^2 \right) + d_{11} \frac{\partial \psi}{\partial \xi} = 0 \quad (6.30)$$

for a hinged-hinged (H-H) boundary condition.

6.6 GDQ method

The differential quadrature (DQ) method [134,135] is used to solve Eq. (6.28) and the associated boundary conditions to determine the nonlinear frequencies of FGS-CNTR. The fundamental idea of the DQ method is to approximate the derivative of a function at a sample point as a linearly weighted sum of its values at all the sample points in the problem domain. Hence, the n th order derivative of a continuous function $f(x, z)$ with respect to x at a given point x_i can be

approximated as a linear sum of weighted values at all of the discrete points in the domain of x as follows:

$$\frac{\partial f^{n(x_i, z)}}{\partial x^n} = \sum_{k=1}^N c_{ik}^n f(x_{ik}, z), \quad (i=1,2,\dots,N, n=1,2,\dots,N) \quad (6.31)$$

1)

where N is the number of sampling points, and c_{ij}^n [49] is the x_i dependent weight coefficients.

Applying Eq. (6.31) to Eq. (6.28), one obtains a set of ordinary differential equations

$$a_{11} \left(\sum_{j=1}^N C_{ij}^2 u_j + \frac{1}{\lambda} \sum_{j=1}^N C_{ij}^1 w_j \sum_{j=1}^N C_{ij}^2 w_j \right) + b_{11} \sum_{j=1}^N C_{ij}^2 \psi_j = \bar{I}_1 \ddot{u} + \bar{I}_2 \ddot{w} \quad (6.32a)$$

$$k^* a_{55} \left(\sum_{j=1}^N C_{ij}^2 w_j + \lambda \sum_{j=1}^N C_{ij}^1 \psi_j \right) + \frac{a_{11}}{\lambda} \left(\sum_{j=1}^N C_{ij}^1 u_j \sum_{j=1}^N C_{ij}^2 w_j + \frac{3}{2\lambda} \left(\sum_{j=1}^N C_{ij}^1 w_j \right)^2 \sum_{j=1}^N C_{ij}^2 w_j + \sum_{j=1}^N C_{ij}^2 u_j \sum_{j=1}^N C_{ij}^1 w_j \right) \quad (6.32b)$$

$$+ \frac{b_{11}}{\lambda} \left(\sum_{j=1}^N C_{ij}^2 \psi_j \sum_{j=1}^N C_{ij}^1 w_j + \sum_{j=1}^N C_{ij}^1 \psi_j \sum_{j=1}^N C_{ij}^2 w_j \right) - k_w w_i +$$

$$k_s \sum_{j=1}^N C_{ij}^2 w_j = \bar{I}_1 \ddot{w}$$

$$b_{11} \left(\sum_{j=1}^N C_{ij}^2 u_j + \frac{1}{\lambda} \sum_{j=1}^N C_{ij}^1 w_j \sum_{j=1}^N C_{ij}^2 w_j \right) + d_{11} \sum_{j=1}^N C_{ij}^2 \psi_j - k^* a_{55} \lambda \left(\sum_{j=1}^N C_{ij}^1 w_j + \lambda \psi_i \right) \quad (6.32c)$$

$$= \bar{I}_2 \ddot{u} + \bar{I}_3 \ddot{\psi}$$

where $S_1 = \frac{l_0^2}{4\lambda} a_{55} \left(-\frac{1}{\lambda} \sum_{j=1}^N C_{ij}^4 w_j + \sum_{j=1}^N C_{ij}^3 \psi_j \right)$ and $S_2 = \frac{l_0^2}{4} a_{55} \left(-\frac{1}{\lambda} \sum_{j=1}^N C_{ij}^3 w_j + \sum_{j=1}^N C_{ij}^2 \psi_j \right)$.

The cosine pattern is used to generate the DQ point system

$$x_i = \frac{1}{2} \left(1 - \cos \left(\frac{i-1}{n-1} \pi \right) \right) \quad i = 1, 2, \dots, N \quad (6.33)$$

The associated boundary conditions can be handled in the same way. For example, the

dimensionless boundary condition of clamped-Hinged (C-H) Supported beams is

$$\begin{aligned}
 u_1 = w_1 = \psi_1 = 0 & \quad \text{at } \zeta = 0 \\
 \left\{ \begin{aligned}
 u_N = w_N = 0 \\
 M_x = b_{11} \left(\sum_{j=1}^N c_{Nj}^1 u_j \frac{1}{2\lambda} \left(\sum_{j=1}^N c_{Nj}^1 w_j \right)^2 \right) + d_{11} \sum_{j=1}^N c_{Nj}^1 \Psi_j = 0
 \end{aligned} \right. & \quad \text{at } \zeta = 1
 \end{aligned} \tag{6.33}$$

After implementation of the boundary conditions, Eq. (6.32) can be written in matrix form as

$$\left(K_L + \frac{1}{2} K_{NL1} + \frac{1}{3} K_{NL2} \right) U_d + M \ddot{U}_d = 0 \tag{6.34}$$

where M is the mass matrix; K_L is the linear stiffness matrix; K_{NL1} and K_{NL2} are nonlinear stiffness matrices that are linear and quadratic functions of the displacement vector, U_d , respectively.

Expanding the dynamic displacement vector U_d in the form of $U_d = U_d^* e^{i\omega t}$ where $\omega = \Omega L \sqrt{\sigma/E}$ represents the dimensionless frequency, Ω is the nonlinear vibration frequency of the FG nanocomposite microbeam, U_d^* is the vibration mode shape vector. Substituting U_d into Eq. (6.34) yields the nonlinear eigenvalue equations as follows

$$\left(K_L + \frac{1}{2} K_{NL1} + \frac{1}{3} K_{NL2} \right) U_d^* - M \omega^2 U_d^* = 0 \tag{6.35}$$

To solve the resulting system of nonlinear eigenvalue Eq. (6.35), an iterative procedure should be used. For this purpose, in the first step, the nonlinear terms due to the transverse displacement are neglected, and the resulting eigenvalue problem is solved in each case. In the second step, the eigenvector is appropriately scaled up such that the maximum transverse displacement is equal to the given vibration amplitude w_{max} . Then, the eigenvalue problems are solved again to obtain the new eigenvalues and eigenvectors. In the third step, the eigenvector is scaled up again and step 2 is repeated until the discrepancy between the eigenvalues obtained from

the two consecutive iterations is within 0.1%.

6.7 Results and discussion

6.7.1 Verification

PMMA is selected as the material of the microbeam, with its properties well studied [140]: $K = 0.197 \text{ W/(m K)}$, $c = 550 \text{ J/(kg K)}$, $\rho = 1188 \pm 0.5 \text{ kg/m}^3$, and $\alpha = 3.015 \times 10^{-7} \text{ m}^2/\text{s}$ and $\tau = 2.4 \text{ S}$. Also, $\alpha_m = 45(1 + 0.0005\Delta T) 10^{-6}/\text{K}$ and $E_m = (3.52 - 0.0034T) \text{ GPa}$. In such a way, $\alpha_m = 45.0 \times 10^{-6}/\text{K}$ and $E_m = 2.5 \text{ GPa}$ at $T = 300 \text{ K}$.

Before starting numerical studies, to establish the accuracy of the present formulation and the computer program developed, results obtained from the present study are compared with the available results in the literature. The accuracy of the MT model in estimating the effective mechanical properties of CNT reinforced composites has been shown in the previous paper [77]. For further verification of the solution, the dimensionless nonlinear fundamental frequencies of the CNTR beam ($\eta = L/h = 1$, $h = 0.1$) is compared with the data presented in Ref. [128]. Table 6.2 shows that the present results are in good agreement with the results of Ke et al. [128]. The parameters used in this example are $E^m = 2.5 \text{ GPa}$, $\nu^m = 0.34$, $\rho^m = 1190 \text{ Kg/m}^3$ for the matrix, and the armchair (10,10) SWCNTs are used as the reinforcements with $E_{11}^{cnt} = 600 \text{ GPa}$, $E_{22}^{cnt} = 10 \text{ GPa}$, $\nu^{cnt} = 0.19$, and $\rho^{cnt} = 1400 \text{ Kg/m}^3$.

Furthermore, the numerical solutions of the temperature change ΔT on the free vibration of microbeams given by [139] are also provided in Table 6.3 for a direct comparison. In The parameters used in this example are $\rho = 1220 \text{ kg/m}^3$, $E = 1.44 \text{ GPa}$, $l = 17.6 \text{ }\mu\text{m}$ and $\alpha = 54 \times 10^{-6}/^\circ\text{C}$. It should be noticed that they did not consider temperature variation through the thickness and just assumed some values for the temperature difference. Again, excellent agreement is achieved between the present results and semi-analytical solutions given by [139]. It should be noted that

they just considered the effect of the temperature difference on the linear vibration of the microbeam.

Now, the vibration analysis of FG-CNT reinforces microbeams is studied using the MT approach. The relevant parameters that have been used in the calculation are: $V_i=0.01$, $V_o=0.05$, $q=1$, $h=30 \mu\text{m}$ and $dt=0.0001$. These parameters are kept unchanged unless it is mentioned.

Table 6. 2 Comparison of dimensionless nonlinear frequency ω_{nl} / ω_l for UD-CNTRC beams ($L/h=10$)

	V_{cnt}^*	Method	ω_l	W_{max}				
				0.1	0.2	0.3	0.4	0.5
C-C	0.12	[128]	1.6678	1.0154	1.0605	1.1318	1.2251	1.3381
		Present	1.6621	1.0142	1.0544	1.1143	1.1872	1.2748
	0.28	[128]	2.3634	1.0176	1.0687	1.1490	1.2544	1.3829
		Present	2.3420	1.0171	1.0646	1.1337	1.2157	1.3044
H-H	0.12	[128]	1.2576	1.0278	1.1070	1.2278	1.3791	1.5522
		Present	1.2551	1.0256	1.0952	1.1938	1.3083	1.4302
	0.28	[128]	1.8297	1.0299	1.1151	1.2439	1.4046	1.5874
		Present	1.8201	1.0299	1.1094	1.2065	1.3261	1.4525

Table 6. 3 Thermal effect on the dimensionless natural frequencies for the microbeams with $L/h=10$ and $h/l=2$

Boundary conditions	$\Delta T = 0$	$\Delta T = 20$	$\Delta T = 40$	$\Delta T = 60$	$\Delta T = 80$	$\Delta T = 100$
H-H [139]	0.3478	0.3322	0.3159	0.2986	0.2804	0.2608
Present method	0.3470	0.3318	0.3142	0.2979	0.2800	0.2603
C-C [139]	0.7248	0.7160	0.7071	0.6981	0.6890	0.6798
Present method	0.7242	0.7153	0.7060	0.6977	0.6883	0.6791

Fig 6.5 shows the variation in temperature concerning time for four different points in the thickness direction of the microbeam when there is a thermal shock at $t=0$ and $z=-h/2$. Here, $N_x=N_t=21$ and $dt=0.0001$. So, this figure shows the results in 60000 time steps. We can see that thermal waves travel inside the domain as a result of the time delay and will reach its steady state finally which has not been shown in this figure due to the space limitation.

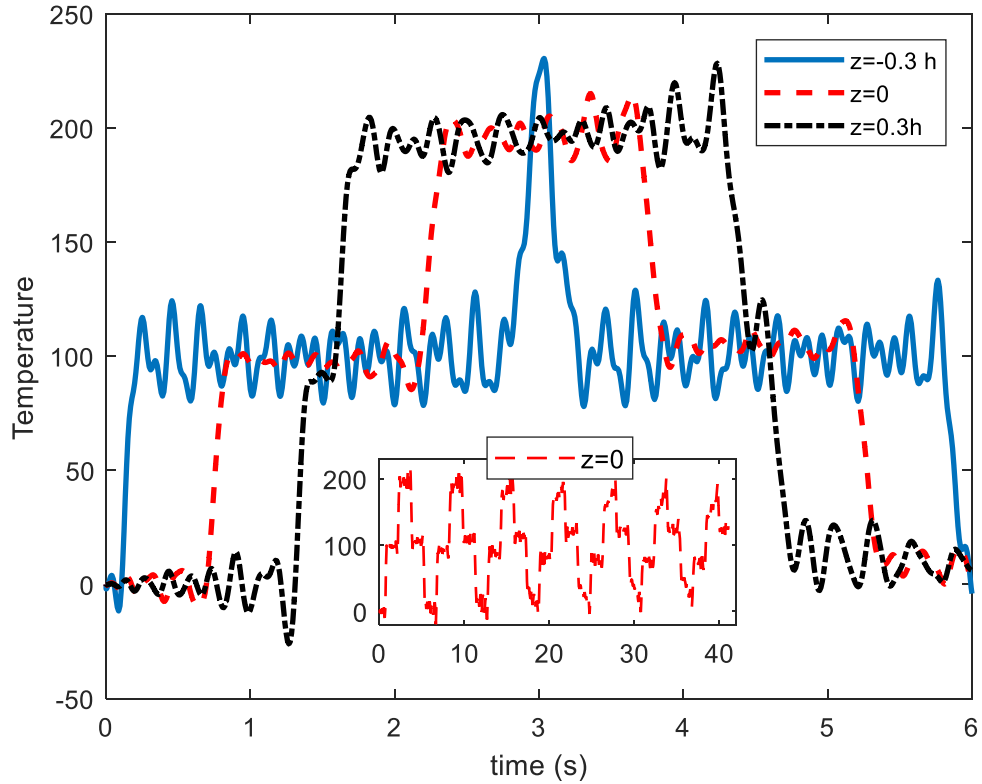


Figure 6. 5 Time evolution of the temperature at different points along the thickness of the beam.

The effects of material length scale parameter as a function of time on the nonlinear frequency and thermal force is depicted in Fig 6.6 when the CNT volume fraction is 0.01 in the lower surface and linearly increases to 0.05 at the outer surface. It can be seen that the nonlinear frequency will take the shape of thermal force, so an increase in thermal force which can be obtained by increasing the thickness of the beam, will increase the nonlinear frequency.

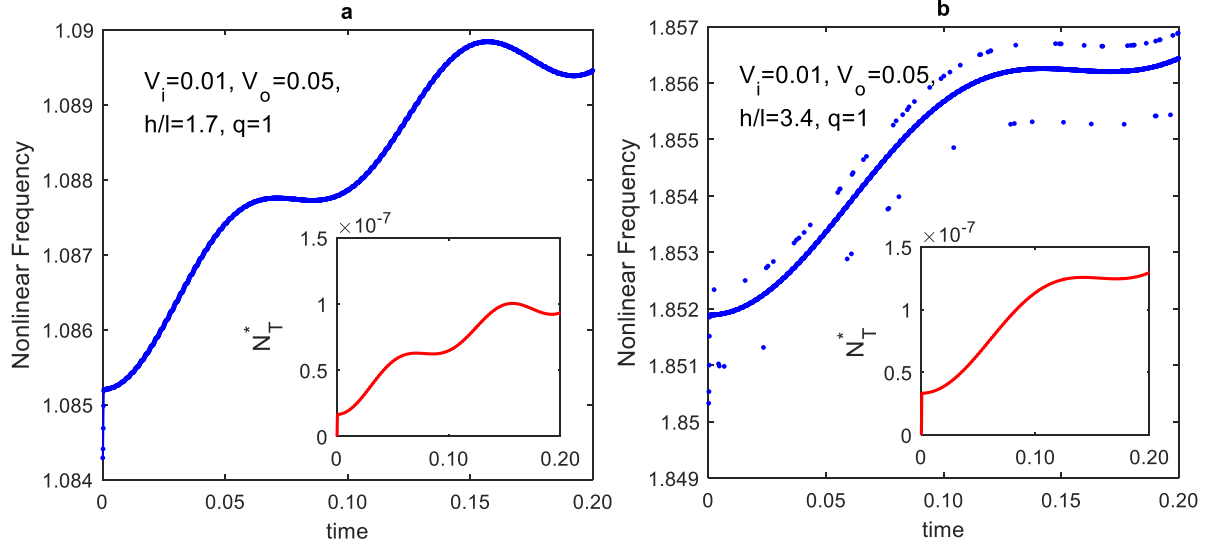


Figure 6. 6 Time evolution of nonlinear frequency and thermal force (N_T^*) $L/h=12$ and BC=C-C, a: $h/l=1.7$ b: $h/l=3.4$

The thermal effect on the dimensionless nonlinear natural frequencies of the FGM microbeams as a function of time corresponding to different CNT volume fractions is listed in Table 6.4. Also, it should be noticed that the time step is equal to 0.0001 S, so $T_s=1000$ shows 0.1 seconds. It can be seen that for a given value of $L/h=12$, the linear and nonlinear frequencies increase with the increase of CNT volume fraction (from $V_o=0.03$ to $V_o=0.05$). This is intuitively correct since with increasing the volume fraction of CNT the microbeam becomes stiffer, so the resultant frequencies increase. The most important result is that unlike all previously published papers which have shown increasing the h/l will decrease frequency, we have reached such a conclusion that when the temperature is taken into account, the result would be different. This happens because when the thickness of the beam (h) increases, we need to solve the heat conduction equation all over again and the thermal force will completely change (Fig 6.5). Then we can solve the eigenvalue problem (vibration problem). As it is seen in this table, increasing the h/l ratio from 1.7 to 3.4 will increase both linear and nonlinear frequency which happens as a result

of the increase in thermal force (The result for the case that thermal force is constant is shown in Fig 6.9). When the time step equals to 1, it shows the results of the structure at its initial conditions with no thermal force. That is why increasing thermal conductivity does not affect frequencies. Furthermore, increasing the thermal conductivity at other time steps will increase both linear and nonlinear frequencies. This happens because the increase in thermal conductivity means faster movement of thermal wave and results in a more significant difference between two different points in the thickness direction at the same time, which in turn, leads to a higher thermal force.

Table 6. 4 Dimensionless linear and nonlinear frequencies of FGM microbeams with various length scale parameters and CNT volume fraction at different time steps ($L/h=12$, $BC=C-C$, $q=1$)

h/l	K	V_i	V_o	ω_{NL}			ω_L		
				$T_s=1$	$T_s=1000$	$T_s=2000$	$T_s=1$	$T_s=1000$	$T_s=2000$
1.7	K_{FGM}	0.01	0.03	0.9607	0.9634	0.9646	0.9137	0.9163	0.9174
	$2*K_{FGM}$	0.01	0.03	0.9607	0.9646	0.9656	0.9137	0.9175	0.9184
	$5*K_{FGM}$	0.01	0.03	0.9607	0.9659	0.9690	0.9137	0.9186	0.9217
	K_{FGM}	0.01	0.05	1.0843	1.0879	1.0895	1.0313	1.0347	1.0363
	$2*K_{FGM}$	0.01	0.05	1.0843	1.0896	1.0909	1.0313	1.0364	1.0377
	$5*K_{FGM}$	0.01	0.05	1.0843	1.0911	1.0953	1.0313	1.0378	1.0418
3.4	K_{FGM}	0.01	0.03	1.6387	1.6427	1.6432	1.5388	1.5425	1.5431
	$2*K_{FGM}$	0.01	0.03	1.6387	1.6431	1.6455	1.5388	1.5429	1.5452
	$5*K_{FGM}$	0.01	0.03	1.6387	1.6457	1.6475	1.5388	1.5454	1.5471
	K_{FGM}	0.01	0.05	1.8503	1.8557	1.8564	1.7378	1.7428	1.7435
	$2*K_{FGM}$	0.01	0.05	1.8503	1.8562	1.8594	1.7377	1.7433	1.7463
	$5*K_{FGM}$	0.01	0.05	1.8503	1.8598	1.8619	1.7378	1.7467	1.7487

Figure 6.7 shows the temperature distribution through the thickness after 0.05 second (500 time steps) from the initial thermal distribution. The effect of the temperature (internal force) on the nonlinear frequency of microbeam has been shown in Figures 6.8 and 6.9.

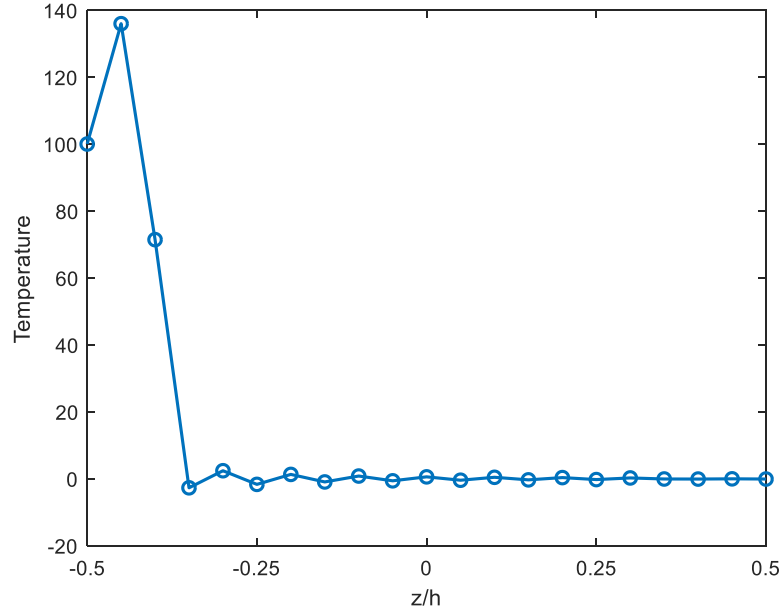


Figure 6. 7 Temperature along the thickness of the microbeam after 0.05 Second (dt=0.0001, h=30 μ m)

Figure 6.8 shows the effects of the amplitude of displacement on the dimensionless, fundamental nonlinear frequency ω_{NL} for the microbeam as a function of L/h with $h/l=2$. It is found that the frequencies for all boundary conditions of the microbeam decrease rapidly with increasing L/h , because a higher L/h indicates a lower stiffness of the microbeam. Also, it is observed that for a small amount of displacement ($W_{max}=0.1$), the nonlinear frequency and linear frequency are almost the same. The effect of the amplitude of displacement on the nonlinear frequencies is considerable for the microbeam with a small slenderness ratio, while it is mild for the microbeam with a large slenderness ratio. In other words, the shorter the beam, the bigger the effects of amplitude curve.

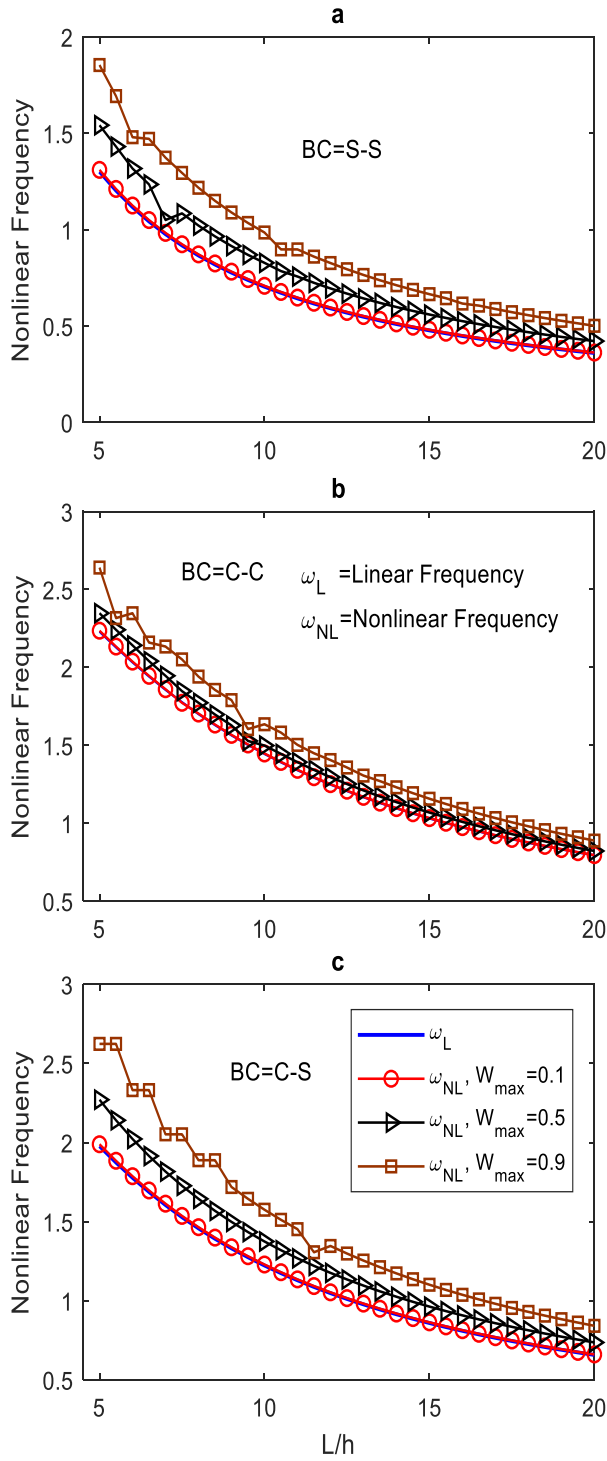


Figure 6. 8 Effects of amplitude curves W_{max} on nonlinear frequency for the microbeam as a function of L/h with $h/l=2$: (a) S-S, (b) C-C and (C) C-S

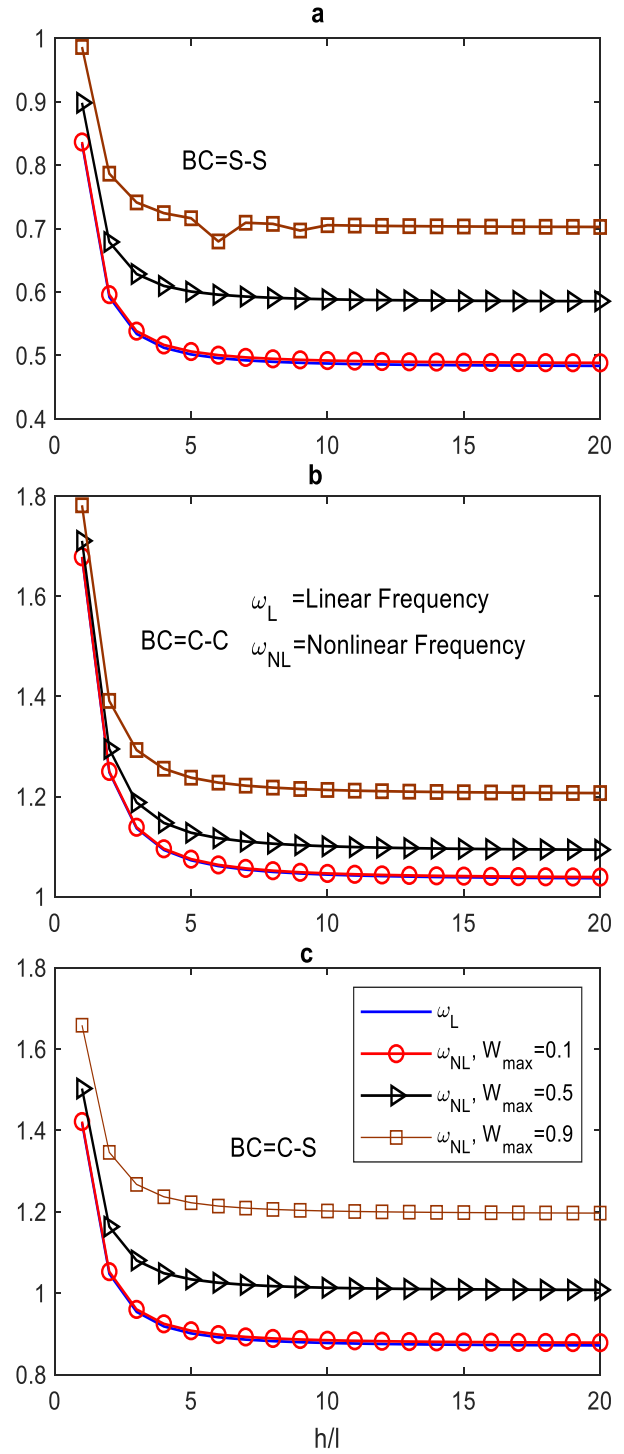


Figure 6. 9 Effects of amplitude curves W_{max} on nonlinear frequency for the microbeam as a function of h/l with $L/h=12$: (a) S-S, (b) C-C and (c) C-S

Figure 6.9 shows the effects of displacement amplitude on the dimensionless, fundamental nonlinear frequency ω_{NL} for the microbeam as a function of h/l with $L/h=12$. It should be noted that since the length scale parameter (l) is used in the formula as $l_0=l/h$, it is possible to consider either l or h as a variable. Because by changing h , different temperature distributions through the thickness will be obtained, and as a result, leading to different thermal forces, we have considered the length scale parameter (l) as a variable. In the calculation, it is also possible to consider h as a variable by assuming that changing h does not change the thermal force. For a given value of h/l , the fundamental frequency increases with the increase of displacement amplitude. It can be seen that the effects of displacement amplitude on ω_{NL} are insignificant when the thickness of the microbeam is close to the material length scale parameter ($h/l=1$ or 2), but becomes significant when the thickness of the microbeams becomes larger (h/l). For a large value of h/l ($h/l>5$), the size effect on the fundamental frequency is not apparent.

Plotted in Fig 6.10 is the variation of dimensionless, nonlinear natural frequencies of the clamped-clamped FG microbeam with time corresponding to various values of material property gradient index q under a heat pulse. Since this thermal shock will become equal to zero after 0.005 seconds and not permanent, the thermal force will become zero after a few time steps. Thus, the resultant nonlinear frequency will become zero after a few time steps as well. Furthermore, it is observed that when $q=0$, which corresponds to a uniform distribution of CNT through the thickness ($V_{CN}=V_i=0.01$) the microbeam has the lowest frequency and $q=1000$ corresponds to the maximum uniform CNT volume fraction ($V_{CN}=V_o=0.05$), and the microbeam has the maximum nonlinear frequency. So, as we increase the CNT volume fraction by increasing q , the nonlinear frequency increases, and also thermal force increases.

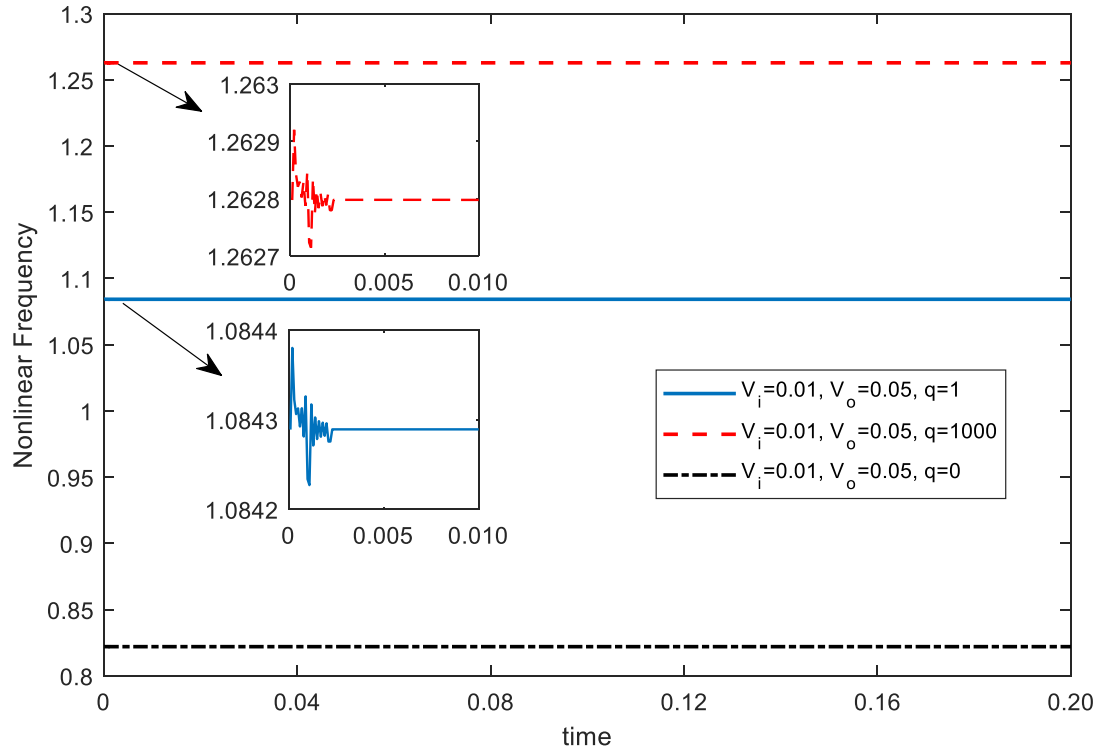


Figure 6. 10 Effect of temperature at different time steps on the non-dimensional nonlinear frequency for the microbeam $h/l=1.7$, $L/h=12$, BC=C-C

6.8 Conclusion

The linear and nonlinear free vibrations of the FG carbon nanotube reinforce microbeams have been investigated based on hyperbolic heat conduction using Timoshenko beam theory. The Mori-Tanaka homogenization technique has been employed to obtain the mechanical properties of the microbeam. Unlike the classical beam theory, the present non-classical beam model takes the internal material length scale parameters into consideration for the microstructural effect. The DQM has been used to discretize the spatial derivatives, then the obtained nonlinear system of ordinary differential equations is solved using the Newton-Raphson method in the temporal domain to obtain temperature distribution in the thickness direction. Then the derived temperature is used to get the thermal force.

It is found that

- The effect of the length scale parameter is significant when the ratio of thickness to the length scale parameter (h/l) is large enough, and thermal force is constant.
- By considering thermal force as a function of the thickness of the microbeam, it is proved that increasing the thickness to the length scale ratio will increase linear and nonlinear frequencies.
- Nonlinear frequency varies in the same spectrum as the thermal force.
- Both linear and nonlinear frequency will increase by increases of the volume fraction of CNTs.
- For an initial heat pulse, the microbeam will approach steady state condition after a few seconds, and thermal force will diminish, and as a result, no change in frequency will be observed.
- For a sudden rise in temperature, the microbeam will reach steady state condition after a more extended period, so the thermal force and vibration stand longer.
- Increasing the thermal conductivity of the material increases the linear and nonlinear frequencies.

Chapter 7:

Thermally induced vibration in nanocomposites cylindrical panel subjected to heat pulse⁶

As a first attempt, the combined application of the differential quadrature method (DQM) and the Newton Raphson method is used to solve the non-Fourier heat conduction equations to obtain temperature, displacements, and stresses in a cylindrical panel made of functionally graded, carbon nanotubes (CNTs) reinforced composite. The heat conduction of a domain made of nanocomposites subjected to heat generation is simulated with a finite heat wave speed. Furthermore, based on the three-dimensional elasticity theory, the thermoelastic analysis of the nanocomposite cylindrical panel subjected to the transient heat conduction is presented. The dynamic Young's modulus of Single-Walled Carbon Nanotubes (SWCNT) can be expressed as a function of loading rate and environmental temperature. All material properties such as heat capacity (C_p), thermal relaxation time (τ), density (ρ) and thermal conductivity (K) are considered as a function of both temperature and CNT volume fraction. The hyperbolic heat conduction is solved to obtain temperature in the spatial and temporal domains. Then by implementing the obtained temperature in thermoelastic equations of the cylindrical panel, the displacements and stresses will be obtained at each time step. The proposed method marches in the time direction

⁶ A version of this chapter is published in International Journal of Solids and Structures 163, 117-129, 2019.

block by block. In each block, there are several time levels, and the numerical results at these time levels are obtained simultaneously. Through this way, the numerical solution at the $(n+1)$ th time level depends on the solutions at its previous levels from the 1st to the n th levels. The final results in the temporal domain are obtained using the Newton-Raphson method. Accuracy of the present solution is confirmed by comparing with some available results in the literature. A detailed numerical study is conducted to examine the effects of heat wave speed and heat flux, CNT volume fraction and the geometrical parameters on the deflection of the cylindrical panel.

7.1 Introduction

The heat- and mass-transfer equations play an important role in various thermal and diffusion processes. In anisotropic media, the thermal diffusivity depends on the direction of heat conduction, while it may depend on coordinates or even on the temperature itself in an inhomogeneous medium [141]. Thus, in modelling many problems in engineering and science, one often faces with the nonlinear heat conduction problems [142]. Also, during the past few years, considerable attention has been concerned with using the non-Fourier heat conduction in problems with very low temperatures, extremely short period of time, or very high heat flux; see, for example, [32,143]. Then a modified flux model for the heat transfer processes with a finite speed wave is suggested. The hyperbolic heat conduction equation based on the Cattaneo model for the heat flux incorporates a relaxation mechanism in order to gradually adjust to a change in the temperature gradient. This model has been a satisfactory extension of classical diffusion theory and can yield the hyperbolic heat conduction equation within the continuum assumption [137]. Rahideh et al. [10] used the layerwise-incremental differential quadrature method (LIDQM) to show the effect of heat wave speed on the thermal characteristics of a multi-layered domain made of functionally graded materials.

CNTs are very attractive as fillers because they offer high strength, stiffness, and exceptional electrical and thermal conductivities of graphite. These significant specification of CNTs, stimulates researchers to investigate the behavior of CNT reinforced composite beam, plate and shell structures subjected to mechanical and or thermal load. The exceptional properties leads the CNT to be designed as significant reinforcement materials and to be the building blocks for a new generation of composite materials to satisfy the need for high performance composite structures [144-148]. Gou et al. [149] studied the interfacial bonding of single walled carbon nanotube (SWCNT) reinforced epoxy composites using molecular dynamics (MD) simulations and experimental method. The unusually high thermal conductivity of CNTs has motivated many researchers using them two the thermal properties of polymeric matrix materials. Therefore it has been extensively investigated experimentally, analytically and numerically. Theoretical prediction showed an extremely high thermal conductivity of an isolated Single Walled Carbon NanoTube (SWCNT) [150]. High thermal conductivity of the CNTs may provide the solution of thermal management for the advanced electronic devices with narrow line width. Liu and Wang [151] studied the nanoscale finite element simulations of the dynamic Young's modulus of SWCNTs under different strain rates and environmental temperatures. They showed that the dynamic Young's modulus of the SWCNTs increases with the increase of strain rate, and decreases dramatically with the increase of environment temperature. Hong and Tai [152] indicated the enhancement of thermal conductivities over ten times and near fifteen times higher than Poly methyl methacrylate (PMMA) for SWCNTs/PMMA and multi walled carbon nanotubes/PMMA composites, respectively. Han and Elliott [108] presented classical Molecular Dynamics (MD) simulations of model polymer/CNT composites constructed by embedding a single wall (10, 10) CNT into PMMA with different volume fractions.

Shells of various geometries and materials have been widely used in many fields of engineering, where they give rise to optimum conditions for dynamical behavior, strength and stability. Pressure vessels, cooling towers, water tanks, dams, turbine engine components and so forth, perform particular functions over different branches of structural engineering. The static and thermoelastic solutions of shells of various shapes have been obtained under different thermomechanical loading conditions by Pourasghar et al. [77,81,153]. Pourasghar and Chen [154] studied thermoelastic behavior of nanocomposite cylindrical panels reinforced by SWCNTs in different thermal environments. They used the extended rule of mixture to investigate the material properties of the shell. Moreover, Shen [155] indicated that the interfacial bonding strength can be improved through the use of a graded distribution of CNTs in the matrix and examined the postbuckling of FG nanocomposite cylindrical panels resting on elastic foundations in thermal environment. Finally, Alibeigloo [156] carried out thermoelastic analyses of cylindrical panel reinforced by SWCNTs. In his work, thermoelastic constants of carbon nanotubes (CNT) and polymer matrix are assumed to be temperature independent.

Thermoelasticity is often used to refer to various phenomena associated with the interaction between deformation and heat exchange occurring in a medium. There are a number of researches related to the development of theories and computational approaches for analyzing thermoelastic behavior of cylindrical panels [157-160]. However, it is found that the studies on mechanical and thermoelastic behavior of nanocomposite structures under transient heat conduction are very rare and all of which have considered thermoelastic constants of carbon nanotube (CNT) temperature independent.

Based on the above review, as a first attempt, non-Fourier heat conduction in a CNT reinforced composite cylindrical panel of temperature-dependent material properties is studied.

The objective of this study is to develop the mathematical models for considering the effect of temperature on the mechanical properties of CNT and static analysis of CNT reinforced cylindrical panel using the differential quadrature method (DQM). Parametric studies such as CNT volume fraction, temperature difference, elastic foundations, are investigated to illustrate their impact on the thermoelastic response of the cylindrical panel.

7.2 Generalized differential quadrature solution of governing equations

The differential quadrature (DQ) approach is used to solve the governing equations of cylindrical panels and heat transfer in the present work. The generalized DQ approach was developed by Shu et al [49] based on the DQ technique. In GDQ method the n th order partial derivative of a continuous function $f(x, z)$ with respect to x at a given point x^i can be approximated as a linear summation of weighted function values at all of the discrete points in the domain of x , *i.e.*

$$\left. \frac{\partial f^p(x, t_j)}{\partial x^p} \right|_{x=x_i} = \sum_{k=1}^N C_{ik}^p f(x_{ik}, t_j), \quad (i = 1, 2, \dots, N_x, j = 1, 2, \dots, N_t, p = 1, 2, \dots, N_x - 1) \quad (7.1)$$

$$\left. \frac{\partial f^p(x, t_j)}{\partial t^p} \right|_{t=t_j} = \sum_{k=1}^N D_{jk}^p f(x_{ik}, t_j), \quad (i = 1, 2, \dots, N_x, j = 1, 2, \dots, N_t, p = 1, 2, \dots, N_t - 1) \quad (7.2)$$

where N_x and N_t are the number of sampling points along x and t direction respectively, also C_{ik}^p and D_{jk}^p are the x_i and t_j dependent weight coefficients. Details of this procedure can be found in the literature [77,153]. In this work, the Chebyshev–Gauss–Lobatto quadrature points are used [49],

$$x_i = \frac{1}{2} \left(1 - \cos \left(\frac{i-1}{N-1} \pi \right) \right) \quad i = 1, 2, \dots, N \quad (7.3)$$

7.3 Problem description

7.3.1 Non-Fourier heat conduction

The structure of the cylindrical panel is shown in Fig 7.1. The global coordinate system r, θ and z for the panel is cylindrical, and has its origin at the center of the curvature $\left(R = \frac{r_i + r_o}{2} \right)$

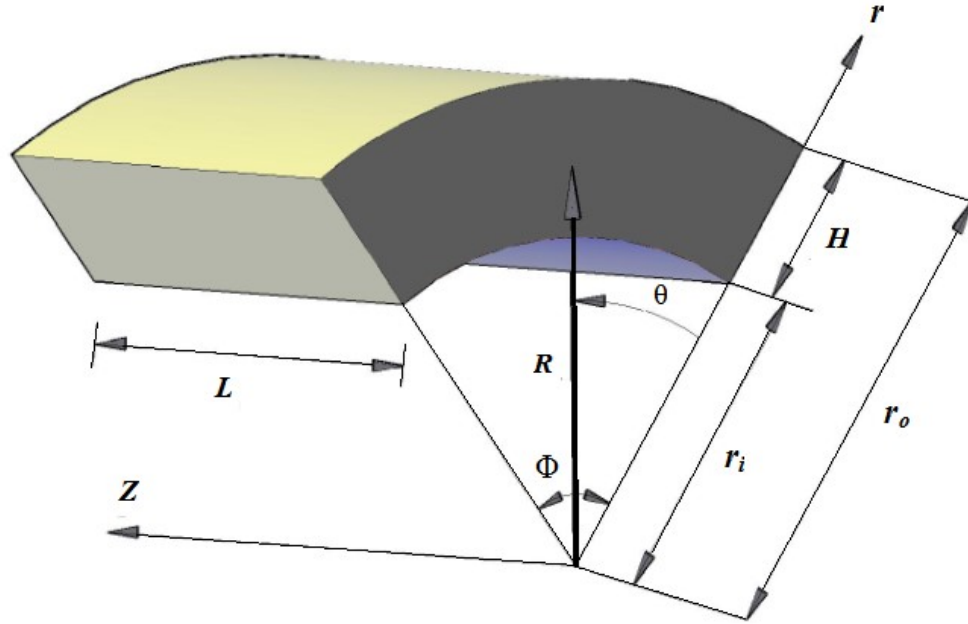


Figure 7. 1 Geometry of cylindrical panel.

The hyperbolic constitutive relation governing the transient heat transfer is as follows

$$\tau \frac{\partial q}{\partial t} + q = -k \frac{\partial T}{\partial x} \quad (7.4)$$

where τ is the relaxation time. q is heat flux, k is thermal conductivity and T is temperature. t and x are the time and spatial coordinate which the thermal wave travels. The relaxation time depends on the mechanism of heat transport, and represents the time lag needed to establish steady-state

heat conduction in an element of volume when a temperature gradient is suddenly applied to that element. It is related to the thermal wave speed and thermal diffusivity as $\tau = \frac{\alpha}{C^2}$. α is thermal diffusivity and C is heat wave speed. Moreover, the energy equation can be written as,

$$\rho C_p \frac{\partial T}{\partial t} + \frac{\partial q}{\partial r} = g(r, t) \quad (7.5)$$

where C_p is heat capacity. The DQM is used to discretize the spatial derivatives, and the incremental DQM is employed to discretize the temporal domain. Based on this approach, the total temporal domain is divided into a set of time intervals where the DQ rule is employed to discretize the temporal derivatives. At the end of each time interval, the temperature and heat flux are used as the initial condition for the next time interval.

DQ method being applied to Eqs. (7.4,7.5), the following equations at an arbitrary sampling point x_i and t_j are then obtained:

$$k_{ij} \left(\sum_{m=1}^{N_x} C_{im}^1 T_{mj} \right) + \tau_{ij} \left(\sum_{n=1}^{N_t} D_{jn}^1 q_{in} \right) + q_{ij} = 0 \quad (7.6)$$

$$\left(\sum_{m=1}^{N_x} C_{im}^1 q_{mj} \right) + \rho_{ij} (C_p)_{ij} \left(\sum_{n=1}^{N_t} D_{jn}^1 T_{in} \right) = g_{ij} \quad (7.7)$$

Finally, one obtains a system of nonlinear algebraic equations in each time interval which is solved using the Newton–Raphson method and the procedure is repeated for all time intervals.

Let's consider the hollow cylinder under a sudden temperature change on the inner and outer surface. From Fig 7.1, the boundary conditions of the problem can be expressed as [49,50]

$$\begin{cases} T(r_i, t) = \begin{cases} \frac{1}{2} + \frac{3}{4} \left(\frac{2t}{t^*} - 1 \right) - \frac{1}{4} \left(\frac{2t}{t^*} - 1 \right)^3 & \text{if } 0 \leq t \leq t^* \\ 1 & \text{if } t \geq t^* \end{cases} \Rightarrow \\ T(x, 0) = 0 \\ q(r_o, t) = 0 \\ q(x, 0) = 0 \end{cases} \quad (7.8)$$

First, let's consider heating pulse is applied to the inner surface of the plate. The main goal of this example is to predict the propagation of the thermal disturbance as shown in Fig 2.2. The convergence of the presented DQM is shown in this figure. The same parameters as those in the work of Dorao [50] are considered. Now, let's consider heating pulse applied to the left boundary of a parallel sided slab, which can be taken as the extreme case when the radius of curvature of the panel tends to infinity. The initial and boundary conditions are

$$\begin{cases} q(r_i, t) = \begin{cases} -1 + \left(\frac{2t}{t^*} + 1 \right)^{2/3} & \text{if } 0 \leq t \leq t^* \\ 0 & \text{if } t \geq t^* \end{cases} \Rightarrow \\ q(r, 0) = 0 \\ q(r_o, t) = 0 \\ T(r, 0) = 0 \end{cases} \quad (7.9)$$

7.3.2 Thermal conductivity (K), relaxation time (τ) and heat capacity (C_p) of CNT

Thermal conductivities of the random and aligned CNT reinforced composites are calculated as function of the volume fraction of CNT. Thermal conductivity is greatly improved as the volume fraction of CNTs increases in both random composites and aligned composites [75].

Second-order polynomial equations are used to obtain the thermal conductivity as follow:

$$K_R = 51.9V_{cn}^2 + 0.43V_{cn} + 0.64 \quad (7.10)$$

$$K_A = 90.9V_{cn}^2 + 4.35V_{cn} + 0.77 \quad (7.11)$$

where K_R and K_A refer to the thermal conductivities of randomly distributed CNT and aligned CNT in the composite. Clearly for specific volume fraction of CNT, K_A is bigger than K_R , which leads to faster motion of heat waves in the media [75]. To approach reality, only CNTs with random distributions are considered. Table 3.2 shows the time delay for SWCNTs.

Since the thermal relaxation time of CNTs is remarkably smaller than that of the matrix, we have just used case 1 as an example. In fact, the length of CNTs does not play an important role in heat conduction when the relaxation time of the matrix is relatively high.

The specific heat capacity (C_p) of a CNT as a function of temperature is stated in Hepplestone et al. [26]. They showed that the effect of increasing temperature is to increase the specific heat capacity C_p by approximately a constant amount as follow:

$$C_p = aT + b \quad (7.12)$$

with $a = 2.5642$ ($J/(kg \cdot K)$) and $b = -61.7294$ ($J/(kg \cdot K)$).

7.3.3 CNT-reinforced composite

First, the effective material properties of CNT reinforce cylindrical panels should be determined. The properties of CNTs depend on temperature and geometrical parameters, therefore, various values and diagrams of properties of CNTs were reported in the literatures. This indicates the complexity of CNTs behavior and, moreover, diversity of the methods and models adopted for their performance analyses. Here, the (3,3) SWCNTs are selected as reinforcements. The dynamic Young's modulus of the SWCNTs can be expressed as a function of loading rate and environmental temperature as follows [151,154]:

$$E^{cn}(T, \dot{\varepsilon}) = (E_0 + AT + BT^2 + CT^3)(1 + \dot{\varepsilon}10^{-6})^D \quad (7.13)$$

where A , B , C and D are constants which are independent of loading rate and environmental

temperature, and $\dot{\epsilon}$ is the strain rate. For the zigzag nanotubes (3,3), the constant coefficients are $E_0 = 1.15, A = -2.8 \times 10^{-4}, B = -3.98 \times 10^{-8}, C = 3.74 \times 10^{-11}, D = 0.27, \dot{\epsilon} = 100$. The mechanical properties of polymer nanotube composites in thermal environment are studied and discussed here. For the implementation of CNT reinforce polymers in structural applications, accurate property-microstructure relations are required in the form of micromechanics models. Several good micromechanics models have been developed for the purpose of estimating the homogenized properties of CNT reinforced composite materials, for example, the Mori–Tanaka scheme [152] and the extended rule of mixture [81,153,154]. In this paper, the homogenized properties of the CNT reinforced composite materials are evaluated using the extended rule of mixture as follows,

$$E_{11}(T) = \eta_1 V_{cn} E_{11}^{cn}(T, \dot{\epsilon}) + V_m E^m \quad (7.14)$$

$$\frac{\eta_2}{E_{ii}(T)} = \frac{V_{cn}}{E_{ii}^{cn}(T, \dot{\epsilon})} + \frac{V_m}{E^m} \quad (i = 2,3) \quad (7.15)$$

$$\frac{\eta_3}{G_{ij}(T)} = \frac{V_{cn}}{G_{ij}^{cn}(T, \dot{\epsilon})} + \frac{V_m}{G^m} \quad (ij = 12,13 \text{ and } 23) \quad (7.16)$$

$$v_{ij} = V_{cn} v^{cn} + V_m v^m \quad (ij = 12,13 \text{ and } 23) \quad (7.17)$$

$$\rho = V_{cn} \rho^{cn} + V_m \rho^m \quad (7.18)$$

$$\alpha_{11}(T) = \frac{V_f E_{11}^{cn}(T, \dot{\epsilon}) \alpha_{11}^{cn} + V_m E^m \alpha_{11}^m}{V_f E_{11}^{cn}(T, \dot{\epsilon}) + V_m E^m} \quad (7.19)$$

$$\alpha_{ii}(T) = (1 + v^{cn}) V_{cn} \alpha_{ii}^{cn}(T) + (1 + v^m) V_m \alpha_{ii}^m - v_{1i} \alpha_{11} \quad i = 2,3 \quad (7.20)$$

$$k_{11} = \frac{k_{11}^{cn}}{1 + \frac{2a_k}{d} \frac{k_{11}^{cn}}{k_{11}^m}} \quad (7.21)$$

$$k_{ii} = \frac{k_{ii}^{cn}}{1 + \frac{2a_k}{L} \frac{k_{ii}^{cn}}{k_{ii}^m}} \quad i = 2,3 \quad (7.22)$$

where E_{ii}^{cn}, G_{ij}^{cn} , v^{cn} , $\rho^{cn}, \alpha_{ii}^{cn}$ and k_{ii}^{cn} are the elastic modulus, shear modulus, Poisson's

ratio, density, thermal expansion coefficient and thermal conductivity, respectively, of the carbon nanotube; and $E^m, G^m \left(G^m = \frac{E^m}{2(1+\nu^m)} \right), \nu^m$, corresponding properties for are k_{ii}^m and α_{ii}^m, ρ^m the matrix; $\eta_j (j = 1, 2, 3)$ are the CNT efficiency parameters. Also, d and L are the diameter and length of the nanotubes, respectively; and $a_k = R_k k_m$ is a so-called Kapitza radius in which $R_k = 8 * 10^{-8} m^2 \frac{K}{W}$ [28]. It should be noted that the effective material properties of CNT reinforced cylindrical panels, such as Young's modulus, shear modulus and thermal expansion coefficients, are functions of temperature and geometrical coordinate. In this paper, the SWCNT reinforcement is Uniformly Distributed (UD) in the thickness direction. It is assumed that the CNT reinforced cylindrical panel is made from a mixture of SWCNT and matrix which is assumed to be isotropic. For isotropic cylindrical panel, the variation of the carbon nanotube volume fraction is assumed as follows:

$$V_{cn} = V_{cn}^* \quad (7.23)$$

where

$$R = \left(\frac{r_i + r_o}{2} \right) \quad \text{and} \quad V_{cn}^* = \frac{\rho^m}{\rho^m + \rho^{cn} (w^{cn})^{-1} - \rho^{cn}} \quad (7.24)$$

where V_{cn} and V_m are the CNT and matrix volume fractions related by $V_{cn} + V_m = 1$.

7.4 Thermoelastic solution of the cylindrical panel

The thermo-elastic constitutive relations of a typical CNT reinforce cylindrical panel can be found in the previous work of Pourasghar and Chen [154]:

$$\sigma = C\varepsilon - \beta T \quad (7.25)$$

where T is the change in temperature of a material particle from that in the stress-free reference configuration obtained in the previous parts (Non-Fourier and non-linear heat conduction). Also,

$$\sigma = \{\sigma_z, \sigma_\theta, \sigma_r, \tau_{\theta r}, \tau_{zr}, \tau_{z\theta}\} \quad , \quad \varepsilon = \{\varepsilon_z, \varepsilon_\theta, \varepsilon_r, \gamma_{\theta r}, \gamma_{zr}, \gamma_{z\theta}\}$$

$$C = \begin{bmatrix} C_{11} & C_{12} & C_{13} & 0 & 0 & 0 \\ C_{12} & C_{22} & C_{23} & 0 & 0 & 0 \\ C_{13} & C_{23} & C_{33} & 0 & 0 & 0 \\ 0 & 0 & 0 & C_{44} & 0 & 0 \\ 0 & 0 & 0 & 0 & C_{55} & 0 \\ 0 & 0 & 0 & 0 & 0 & C_{66} \end{bmatrix} \quad , \quad (7.26)$$

$$\begin{bmatrix} \beta_{11} \\ \beta_{22} \\ \beta_{33} \end{bmatrix} = \begin{bmatrix} C_{11}\alpha_{11} + C_{12}\alpha_{22} + C_{13}\alpha_{33} \\ C_{12}\alpha_{11} + C_{22}\alpha_{22} + C_{23}\alpha_{33} \\ C_{13}\alpha_{11} + C_{23}\alpha_{22} + C_{33}\alpha_{33} \end{bmatrix}$$

In the absence of body forces, the governing equations are as follows:

$$\frac{\partial \sigma_z}{\partial z} + \frac{\partial \tau_{z\theta}}{r \partial \theta} + \frac{\partial \tau_{rz}}{\partial r} + \frac{\tau_{rz}}{r} = 0$$

$$\frac{\partial \tau_{\theta z}}{\partial z} + \frac{\partial \sigma_\theta}{r \partial \theta} + \frac{\partial \tau_{r\theta}}{\partial r} + \frac{2\tau_{r\theta}}{r} = 0 \quad (7.27)$$

$$\frac{\partial \tau_{zr}}{\partial z} + \frac{1}{r} \frac{\partial \tau_{\theta r}}{\partial \theta} + \frac{\partial \sigma_r}{\partial r} + \frac{\sigma_r - \sigma_\theta}{r} = 0$$

The following simply supported conditions are imposed at the edges of the cylindrical panel:

$$u_r = \sigma_\theta = \tau_{\theta z} = 0, T = 0 \quad \text{at} \quad \theta = 0, \phi \quad z = 0, L \quad (7.28)$$

Moreover, the boundary conditions at the concave and convex surfaces, $r = r_i, r_o$, respectively, can be described as follows:

$$\tau_{rz} = \tau_{r\theta} = \sigma_r = 0, \quad \text{at} \quad r = r_i \quad (7.29)$$

$$\tau_{rz} = \tau_{r\theta} = \sigma_r = 0, \quad \text{at} \quad r = r_o \quad (7.30)$$

The boundary and initial conditions for temperature is like what we had for nonlinear and

non-Fourier heat conduction. We seek a semi-inverse solution for the displacement and heat conduction field by assuming that:

$$\begin{aligned}
u_r(r, \theta, z) &= U_r(r) \sin(\beta_m \theta) \sin(p_n z) \\
u_\theta(r, \theta, z) &= U_\theta(r) \cos(\beta_m \theta) \sin(p_n z) \\
u_z(r, \theta, z) &= U_z(r) \sin(\beta_m \theta) \cos(p_n z)
\end{aligned} \tag{7.31}$$

$$\beta_m = \frac{m\pi}{\Phi}, \quad p_n = \frac{n\pi}{L} \quad (m, n = 1, 2, \dots)$$

$$T(r, \theta, z) = T(r) \sin(\beta_m \theta) \sin(p_n z) \tag{7.32}$$

where "m" and "n" are circumferential and axial wave numbers. The simply supported opposite edges at $z = 0, L$ are identically satisfied by the assumed displacement field.

Upon substituting Eq.(7.31) and (7.32) into the governing Eq.(7.25), the coupled partial differential equations reduce to a set of coupled ordinary differential equations (ODE) as follows:

$$-\bar{C}_{55} p_n \frac{\partial U_z}{\partial r} - \bar{C}_{55} p_n^2 U_r + \bar{C}_{44} \frac{1}{r^2} \beta_m U_\theta - \bar{C}_{44} \frac{1}{r} \beta_m \frac{\partial U_\theta}{\partial r} - \bar{C}_{44} \frac{1}{r^2} \beta_m^2 U_r - \frac{\partial \bar{C}_{13}}{\partial r} p_n U_z - \bar{C}_{13} p_n \frac{\partial U_z}{\partial r} \tag{7.33}$$

$$+ \frac{\partial \bar{C}_{23}}{\partial r} \frac{1}{r} U_r - \frac{\partial \bar{C}_{23}}{\partial r} \frac{1}{r} \beta_m U_\theta - \bar{C}_{23} \frac{1}{r} \beta_m \frac{\partial U_\theta}{\partial r} + \frac{\partial \bar{C}_{33}}{\partial r} \frac{\partial U_r}{\partial r} + \bar{C}_{33} \frac{\partial^2 U_r}{\partial r^2} - \bar{C}_{13} \frac{1}{r} p_n U_z + \bar{C}_{33} \frac{1}{r} \frac{\partial U_r}{\partial r}$$

$$+ \bar{C}_{12} \frac{1}{r} p_n U_z - \bar{C}_{22} \frac{1}{r^2} U_r + \bar{C}_{22} \frac{1}{r^2} \beta_m U_\theta - \beta_3 \frac{\partial T}{\partial r} \left[\frac{\partial \beta_3}{\partial r} - \frac{1}{r} \beta_3 + \beta_2 \frac{1}{r} \right] T = 0$$

$$-\bar{C}_{66} p_n^2 U_\theta - \bar{C}_{66} \frac{1}{r} p_n \beta_m U_z - \bar{C}_{12} \frac{1}{r} \beta_m p_n U_z + \bar{C}_{22} \frac{1}{r^2} \beta_m U_r - \bar{C}_{22} \frac{1}{r^2} \beta_m^2 U_\theta + \bar{C}_{23} \frac{1}{r} \beta_m \frac{\partial U}{\partial r}$$

$$- \frac{\partial \bar{C}_{44}}{\partial r} \frac{1}{r} U_\theta + \frac{\partial \bar{C}_{44}}{\partial r} \frac{\partial U_\theta}{\partial r} + \frac{\partial \bar{C}_{44}}{\partial r} \frac{1}{r} \beta_m U_r + \bar{C}_{44} \frac{\partial^2 U_\theta}{\partial r^2} + \bar{C}_{44} \frac{1}{r} \beta_m \frac{\partial U_r}{\partial r} - \bar{C}_{44} \frac{1}{r^2} U$$

$$+ \bar{C}_{44} \frac{1}{r} \frac{\partial U_\theta}{\partial r} + \bar{C}_{44} \frac{1}{r^2} \beta_m U_r - \frac{1}{r} \beta_2 \beta_m T = 0$$

$$\begin{aligned}
& -\bar{C}_{11} p_n^2 U_z + \bar{C}_{12} \frac{1}{r} p_n U_r - \bar{C}_{12} \frac{1}{r} \beta_m p_n U_\theta + \bar{C}_{13} p_n \frac{\partial U_r}{\partial r} - \bar{C}_{66} \frac{1}{r} \beta_m p_n U_\theta - \bar{C}_{66} \frac{1}{r^2} \beta_m^2 U_z \\
& + \frac{\partial \bar{C}_{55}}{\partial r} \frac{\partial U_z}{\partial r} + \frac{\partial \bar{C}_{55}}{\partial r} p_n U_r + \bar{C}_{55} \frac{\partial^2 U_z}{\partial r^2} + \bar{C}_{55} p_n \frac{\partial U_r}{\partial r} + \bar{C}_{55} \frac{1}{r} \frac{\partial U_z}{\partial r} + \bar{C}_{55} \frac{1}{r} p_n U_r - \beta_1 p_n T = 0
\end{aligned} \tag{7.35}$$

Here, the transversely discretized governing differential equations and the related boundary conditions are transformed into algebraic equations via the DM. The DQM being applied to Eq. 7.33, the following equation at an arbitrary sampling point r^i is then obtained:

$$\begin{aligned}
& -\bar{C}_{55} p_n \sum_{k=1}^N c_{ik}^{(1)} U_{zk} - \bar{C}_{55} p_n^2 U_{ri} + \bar{C}_{44} \frac{1}{r^2} \beta_m U_{\theta i} - \bar{C}_{44} \frac{1}{r} \beta_m \sum_{k=1}^N c_{ik}^{(1)} U_{\theta k} - \bar{C}_{44} \frac{1}{r^2} \beta_m^2 U_{ri} - \frac{\partial \bar{C}_{44}}{\partial r} p_n U_{zi} \\
& - \bar{C}_{13} p_n \sum_{k=1}^N c_{ik}^{(1)} U_{zk} + \frac{\partial \bar{C}_{23}}{\partial r} \frac{1}{r} U_{ri} - \frac{\partial \bar{C}_{23}}{\partial r} \frac{1}{r} \beta_m U_{\theta i} - \bar{C}_{23} \frac{1}{r} \beta_m \sum_{k=1}^N c_{ik}^{(1)} U_{\theta k} + \frac{\partial \bar{C}_{33}}{\partial r} \sum_{k=1}^N c_{ik}^{(1)} U_{rk} - \bar{C}_{13} \frac{1}{r} p_n U_{zi} + \bar{C}_{12} \frac{1}{r} p_n U_{zi} \\
& + \bar{C}_{33} \sum_{k=1}^N c_{ik}^{(2)} U_{rk} + \bar{C}_{33} \frac{1}{r_n} \sum_{k=1}^N c_{ik}^{(1)} U_{rk} - \bar{C}_{22} \frac{1}{r^2} U_{ri} + \bar{C}_{22} \frac{1}{r^2} \beta_m U_{\theta i} - \beta_3 \sum_{k=1}^N \bar{C}_{ik}^{(1)} T_k + \left[-\frac{\partial \beta_3}{\partial r} - \frac{1}{r} \beta_3 + \beta_2 \frac{1}{r} \right] T_i = 0
\end{aligned} \tag{7.36}$$

Similarly, the other equations of motion and boundary conditions can also be discretized, however, for brevity they are not presented here [154]. The critical point is that now it is possible to plug in the value of T (temperature) at each sample point obtained in the previous parts. After implementation of T in the discretized form of Eqs. (7.36), we have:

$$A_{db} U_b + A_{dd} U_d = -RD \tag{7.37}$$

where A_{db} and A_{dd} are the stiffness matrices and RD is the constant value that will be obtained after implementation of temperature in the discretized equations. Also, as temperature at each time step is now obtained, we can have the displacements and stresses at each time step. In a similar manner, the discretized form of the boundary conditions becomes:

$$A_{bb} U_b + A_{bd} U_d = -RB \tag{7.38}$$

where A_{bb} and A_{bd} are the stiffness matrices and RB is a constant value that will be obtained after

implementation of temperature in discretized form of boundary conditions. Using Eq. (7.38) to eliminate the boundary degrees of freedom b from Eq. (7.37), one obtains:

$$\left(A_{dd} - A_{db} A_{bb}^{-1} A_{bd} \right) U_d = -RD + A_{db} A_{bb}^{-1} RB \quad (7.39)$$

The above system of equations can be solved to find the displacement (U), and then stresses of the CNT reinforced orthotropic cylindrical panel.

7.5 Results and discussion

7.5.1 Validation and comparison studies

The present method is validated in the previous publication of the author [154] by studying its convergence behavior and by comparing the results with those available in the literature. To validate the thermal analyses, the results are presented for an FG orthotropic cylindrical panel under uniform thermal load and compared with published results [161] as shown in Fig 7.2. The orthotropic panel consists of continuous tungsten reinforcement fibers in a copper matrix (W/Cu). Fig 7.2 shows the variation of the non-dimensional displacement in the radial and circumferential directions through the thickness $\left(\eta = \frac{r-R}{H} \right)$ at the middle length of the cylinder due to the uniform internal pressure and uniform thermal loading, respectively. It is noticed the present results agree well with the literature.

Here, some new results on thermoelastic behavior of CNTR cylindrical panel with temperature-dependent material properties are presented. In particular, the results are presented for an FGM orthotropic cylindrical panel under thermal loading. The orthotropic panel consists of CNT reinforcement particles and PMMA as the matrix. The mechanical properties of the considered material are as follows:

For PMMA:

$K = 0.197 \text{ W/(m K)}$, $c = 550 \text{ J/(kg K)}$, $\rho = 1188 \pm 0.5 \text{ kg/m}^3$, and $\alpha = 3.015 \times 10^{-7} \text{ m}^2/\text{s}$ and $\tau = 2.4$

S. Also, $\alpha_m = 45(1 + 0.0005\Delta T) 10^{-6}/\text{K}$ and $E_m = (3.52 - 0.0034T) \text{ GPa}$.

The mechanical properties of CNT can be found in the previous sections.

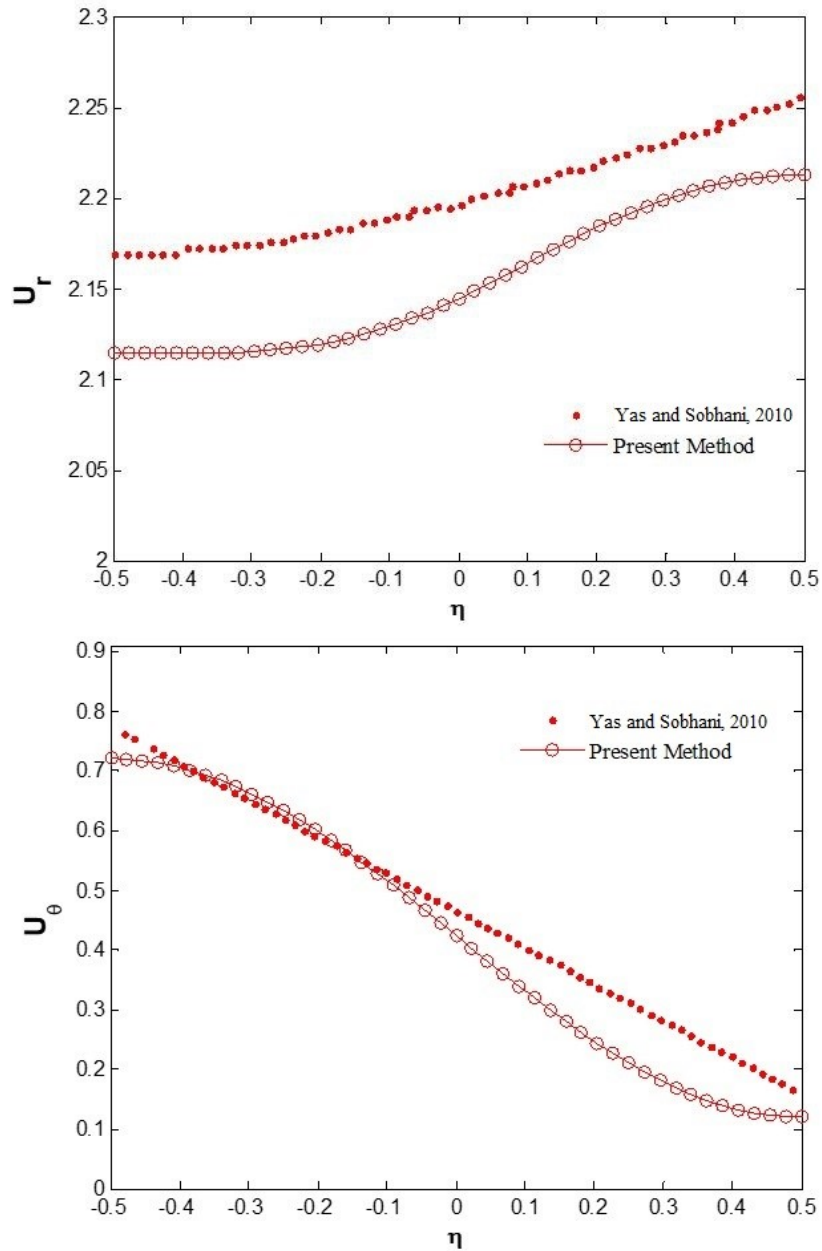


Figure 7. 2 Comparison of the non-dimensional radial and circumferential displacement under uniform Thermal load [161]

7.5.2 CNT reinforced cylindrical panel

In this section, the response of orthotropic cylindrical panels is characterized by graded CNT volume fractions under thermal loading. Temperature, displacements and stresses are as follows:

$$\bar{U} = \frac{U}{\alpha_m T_1}, \bar{\sigma} = \frac{\sigma}{\alpha_m E_m T_1}, \bar{T} = \frac{T}{T_1}$$

where $T_1 = 1$ K.

The cylindrical panel has geometrical parameters as: $L=10$ m, $r_i=0.49$, $r_o=0.51$ and $\theta = \pi/3$.

Figure 7.3 shows the variation of temperature concerning time for three different points in the radial direction of the cylindrical panel. As expected, the temperature will drastically decrease near the outer surface of the cylindrical panel. Because of the imposed boundary condition in the inner surface, a higher temperature will be experienced in that area, and because of the low thermal conductivity of the polymer, this heat cannot easily pass through the thickness. Heat waves will fade almost after 20 seconds corresponding to the beginning of the steady state.

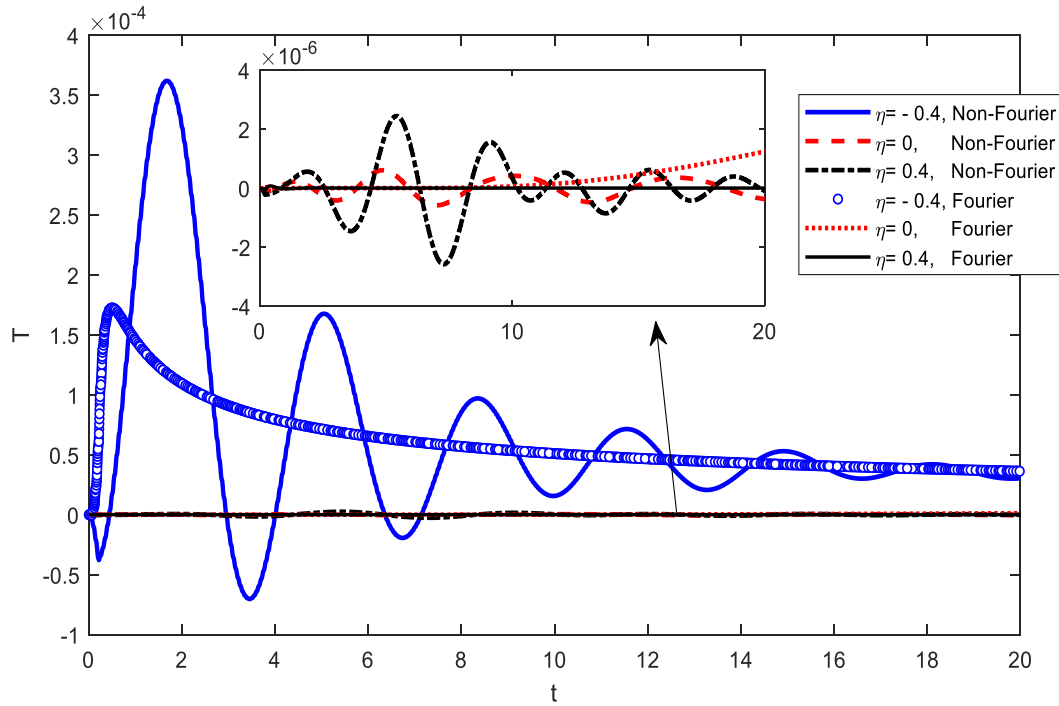


Figure 7.3 Time evolution of the temperature ($p=1$)

Figure 7.4a shows the solution of non-Fourier (hyperbolic) heat conduction at each time step. To accurately solve the governing equations, the physical and temporal domains are divided into 21 layers ($Nx=Nt=21$). The total temporal domain is divided into a set of time intervals, and in each of them, the DQ rule is employed to discretize the temporal derivatives. At the end of each time interval, the temperature and heat flux are used as the initial condition for the next time interval. The total number of subdomains of the temporal domain is equal to 21, and $dt = 0.05$ is the magnitude of each time interval in the subdomain. So, the magnitude of each time step (TS) in the temporal domain is equal to $Dt=1$ second. The temperature distributions through the thickness at time $S= 1, 2, 10, 20$ are depicted in Fig 7.4a. After the temperature is obtained at each time step, the displacements and stresses can be obtained by plugging in the temperature in thermoelastic

equations of the cylindrical panel. Figs. 7.4b-h show the nondimensional radial, circumferential

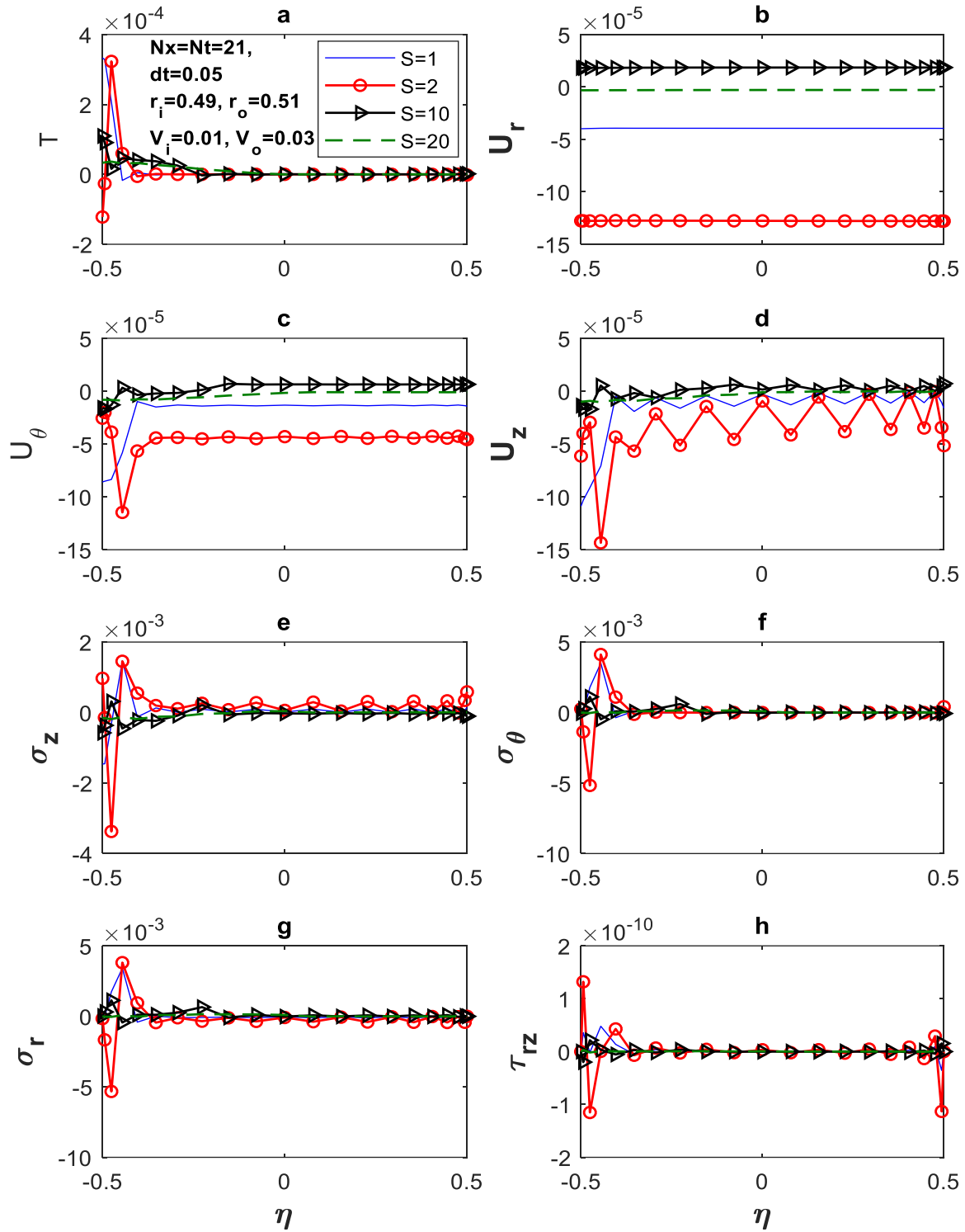


Figure 7. 4 Effect of temperature at different time steps on the non-dimensional displacements and stresses of cylindrical panels when $q(r_i, t)$ is imposed ($p=1$)

and axial displacements and stresses within the thickness of the cylindrical panel. After 20 seconds, heat conduction reaches its steady state, so the smooth variation of stresses will be obtained as shown in Figs. 7.4e-h.

Figure. 7.5 shows the variation of temperature concerning time for three different points in the radial direction of the cylindrical panel. For $\eta = -0.4$ the temperature reaches its maximum after four seconds and stays almost constant as a result of the prescribed boundary conditions. Here, $N_x = N_t = 21$ and $dt = 0.05$. The final steady state for non-Fourier's law is reached after $t > 18$ for $t^* = 0.2$ instead of $t > 8$ as in the case of using the Fourier's law ($\tau = 0$) when $\eta = -0.4$. We can see that thermal waves travel inside the domain until reaching the steady state. In case of the mild increase of temperature at the boundary which is associated with the increase in the time duration of applying it (t^*), the results are getting close to the Fourier heat conduction since. In fact, the thermal shock will phase out, and Fourier heat conduction will take the place of non-Fourier heat conduction. Thus, the temperature would not exceed the temperature of the boundary in the absence of heat generation, and there would be no sign of the thermal wave.

Also, this figure shows that by using the hyperbolic heat conduction, the media will experience a wave-like temperature history with amplitudes beyond the imposed temperature at the boundary in the absence of heat generation. This phenomenon is known as dynamic overshooting, which may lead to the damage of electronic or mechanical devices if it is not appropriately handled.

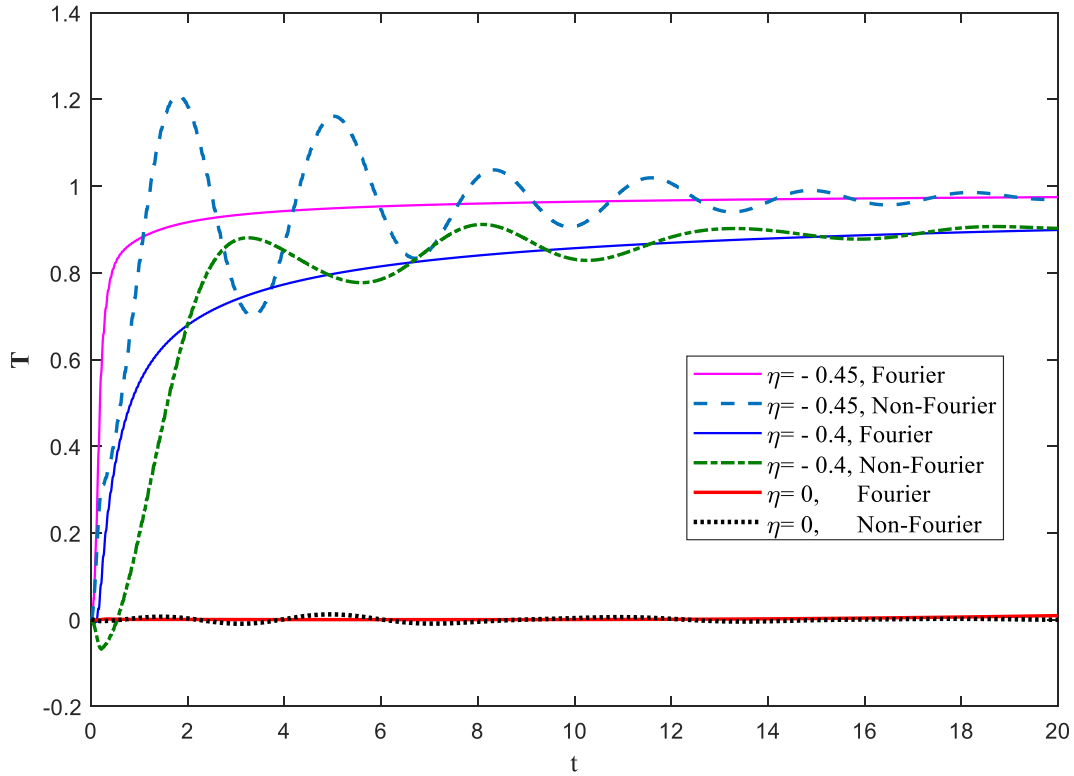


Figure 7. 5 Time evolution of the temperature ($p=1$)

Figure 7.6a shows the solution of non-Fourier (hyperbolic) heat conduction at each time step and the resultant displacements and stresses. Temperature distributions through the thickness after 1, 2, 10, 20 seconds are depicted in Fig 7.6a. Figs 7.6 (b-h) show the nondimensional radial, circumferential and axial displacements and stresses within the thickness of the cylindrical panel. Displacements and stresses have a bigger range of variation since the thermal shock is bigger when the boundary condition is directly imposed on the inner surface. Again, there is no change in the second half ($0 < \eta < 0.5$) of CNT reinforced cylindrical panel since the variation of temperature is almost zero for this part as shown in Fig 7.6. Also, the peaks of the non-dimensional stresses decrease and tend to zero at the stress-free, outer surface which explains the slow motion of transition from transient heat conduction to steady heat conduction.

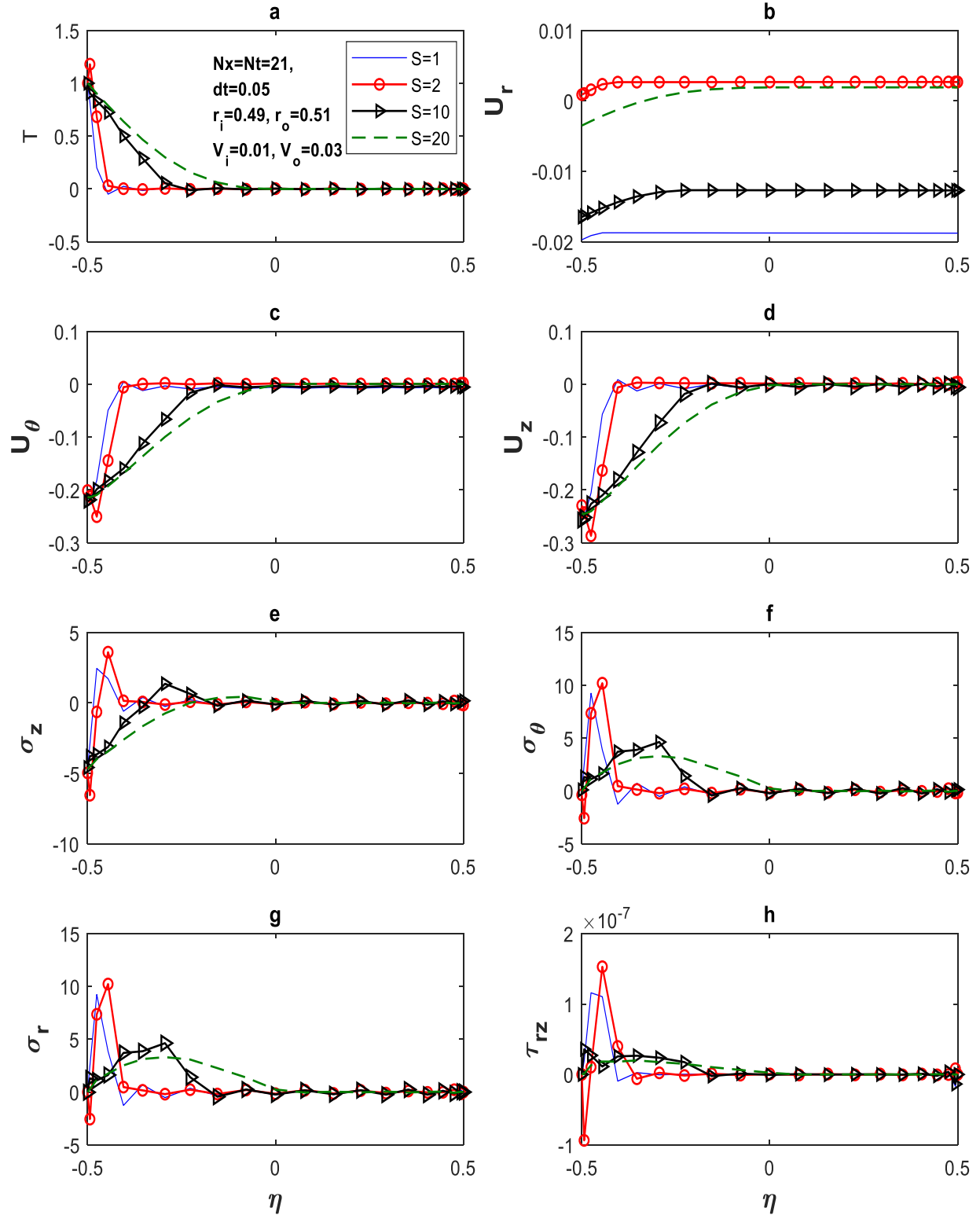


Figure 7. 6 Effect of temperature at different time steps on the non-dimensional displacements and stresses of cylindrical panels when $T(r_i, t)$ is imposed ($p=1$)

Normalized displacements and stress of the CNT reinforced cylindrical panel for $\theta=\pi/6, \pi$ and 2π are calculated and plotted in Fig 7.7, with each figure individually representing two different instants, $S=2$ and $S=20$. As aforementioned, after 20 seconds the structure reaches its steady state, so the variation of displacements and stresses will become smoother when $S=20$.

It can be noticed that changing θ has a negligible impact on the stresses, but the influence on radial and circumferential displacements is considerable. Also, for the variation of stress curve near the inner surface, it can be seen that the stress at $S=2$ is much higher than that at $S=20$, as a result of the direct impact of imposed boundary condition as time elapses, the effect of thermal shock decreases and the stress approaches its steady-state value. By comparing Figs 7.6 and 7.7, the effect of CNT volume fraction is evident. When CNTs are distributed uniformly ($V_i=V_o=0.3$, Fig 7.7), the stress is higher than that when CNTs distributed linearly from the inner surface ($V_i=0.01$) to the outer surface ($V_o=0.03$, Fig 7.6). This is reasonable and intuitively correct since thermal conductivity increases as the volume fraction of CNTs increases, so the effect of thermal shock was felt more by the FG nanocomposite panel.

Figure 7.8 shows the effects of different patterns of CNT distribution through the thickness, while $p=0$ means that $V_{cn}=V_i=0$, $p=1$ means the linear variation of CNT through the thickness from $V_i=0$ to $V_o=0.03$, and $p=10$ means we have the maximum volume fraction of CNT within the thickness. As it can be seen, this variation in CNT volume fraction does not affect the temperature distribution, but it manifests its effect in displacements and stresses. Since these effects are shown for the first second after the implication of the thermal shock, most of these effects are seen in the area close to the inner surface, and the outer surface stays intact. Also, as mentioned, the more CNT volume fraction, the stiffer the cylindrical panel becomes. The stiffer beam, in turn, leads to a smaller displacements and stresses like while $p=10$.

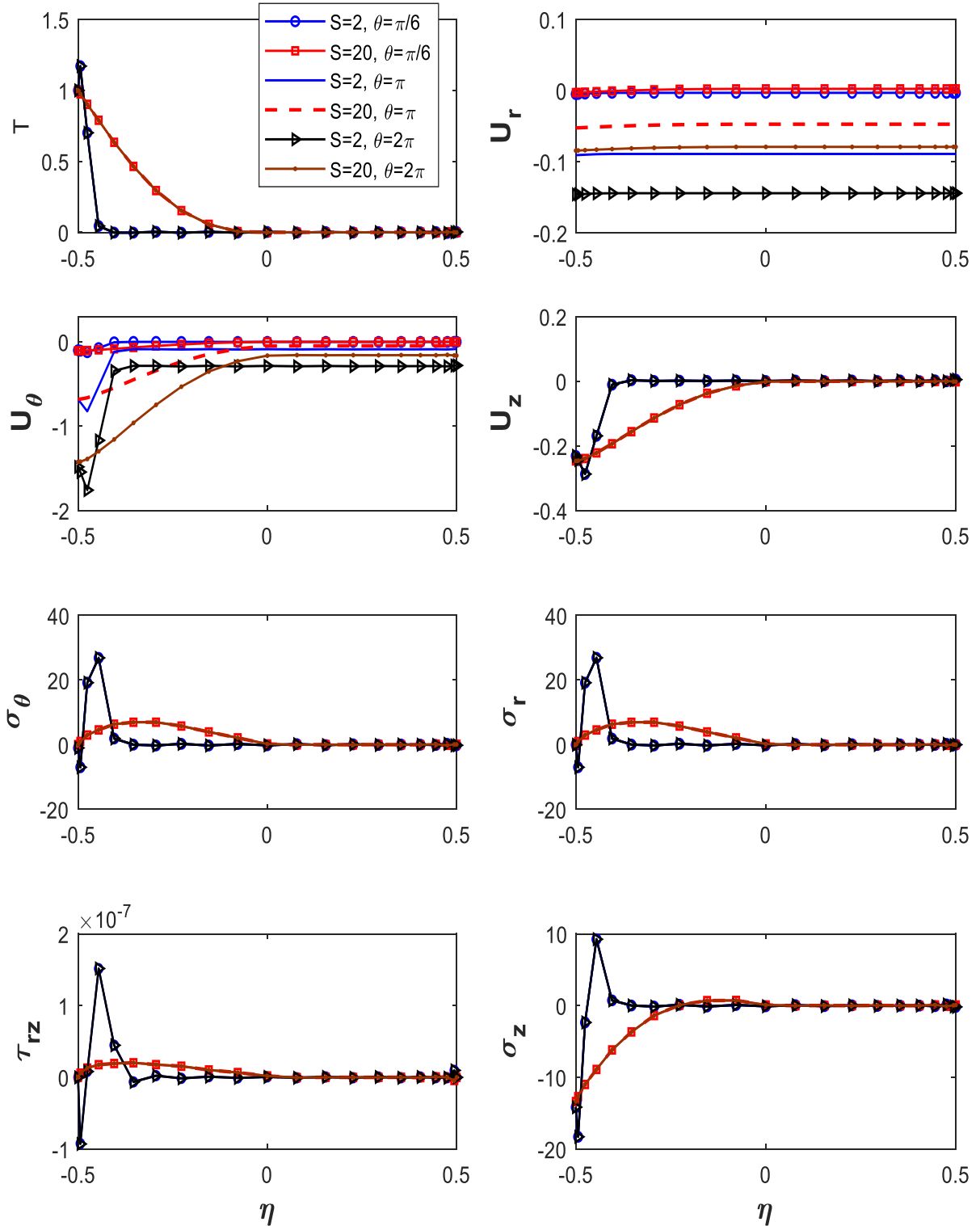


Figure 7.7 Effect of temperature at different time steps on the non-dimensional displacements and stresses of cylindrical panels when $T(r_i, t)$ is imposed ($V_i=V_o=0.03$)

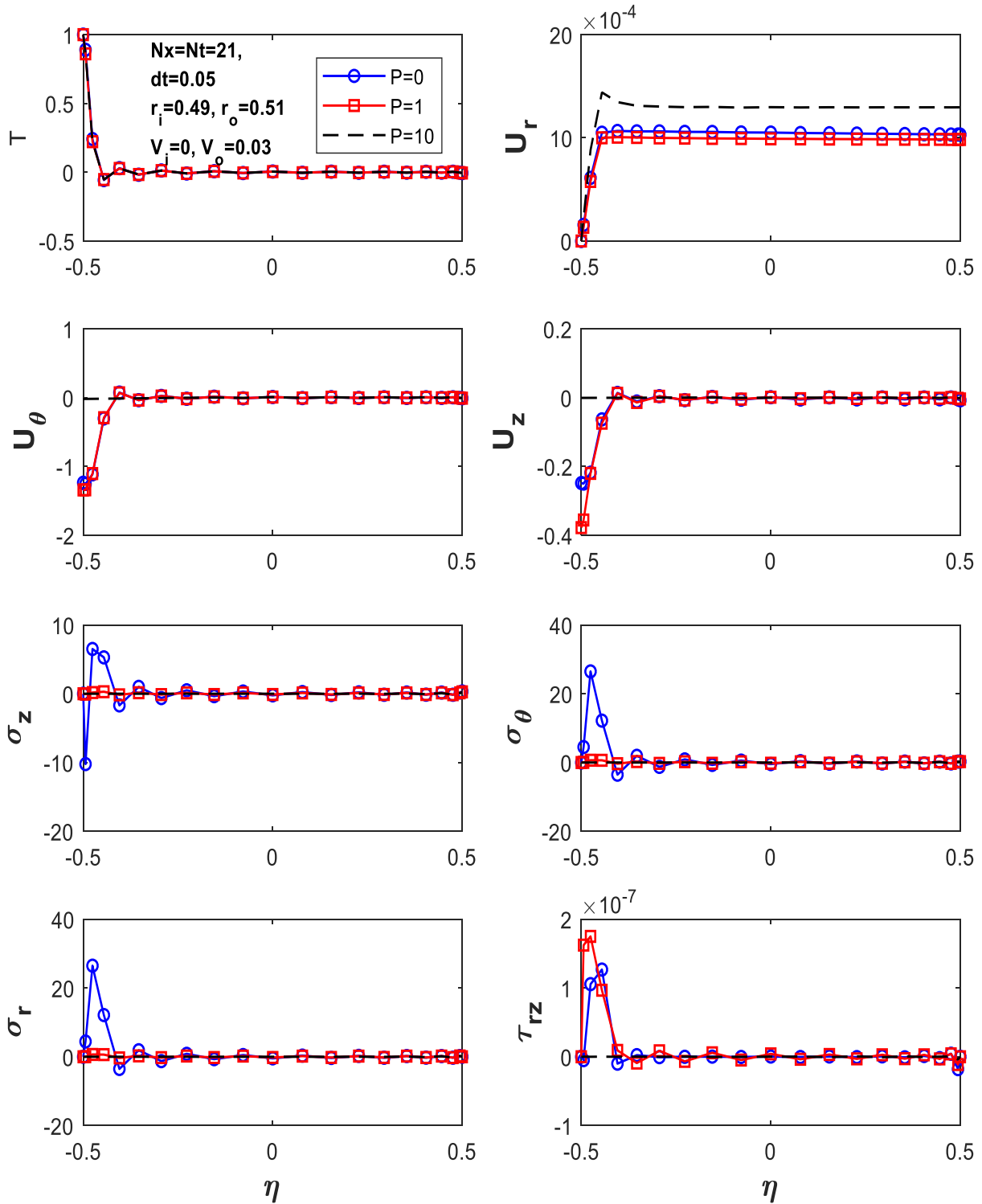


Figure 7. 8 Effect of different pattern of CNT distribution at first second on the non-dimensional radial displacement and stresses of cylindrical panels when $T(r_i, t)$ is imposed

7.6 Conclusions

In this paper, the combined application of the DQM and the Newton Raphson method is used to solve the non-Fourier heat conduction equations to obtain temperature, displacements and stresses in the CNT reinforced, nanocomposite cylindrical panel. All material properties are considered temperature-dependent. The DQM is used to discretize the spatial derivatives as it employs quite a small number of grid points, then the obtained nonlinear system of ordinary differential equations is solved using the Newton-Raphson method in the temporal domain. The total temporal domain is divided into a set of the time intervals, and in each of them, the DQ rule is employed to discretize the temporal derivatives. After solving the hyperbolic heat conduction to obtain the temperature distribution and time history, the deformation and stress of the cylindrical panel have been obtained under different boundary and initial conditions. For non-Fourier heat conduction, the cylindrical panel will be under steady state condition after a few time steps, so no changes in displacements and stresses will be observed.

Also, it is shown that higher CNT volume fraction will result in higher stress in the CNT reinforced nanocomposite cylindrical panel due to the higher thermal conductivity of CNTs. Finally, it is shown that changing θ has a negligible impact on the stresses, but the influence on radial and circumferential displacements is considerable.

The main contribution of this chapter is presenting the unique thermomechanical behaviour of the cylindrical panel under thermal shock on the boundary. As shown a thermal shock can extremely change the stress distribution, and we may have stress concentration at some point in the cylindrical panel.

Chapter 8:

Conclusions and future perspectives

8.1 Conclusions

The conventional form of heat conduction, namely the Fourier law, has broad and successful applications in the thermal systems which have a large spatial dimension with the focus of its long time behavior. However, as a result of the assumption of the infinite speed of heat propagation in the Fourier law, the predicted thermal response may slightly deviate from the actual situation involving high-temperature gradients, ultrafast heating and/or micro/nano-scale heat conduction.

With respect to the fast growth of modern microfabrication technology, quite a number of tiny devices with micro- and nano-scale dimensions emerge in various micromechanical and microelectronic systems. The overshooting phenomenon, which is investigated in this research may lead to permanent damage in these highly sensitive electromechanical devices if it is not handled properly. In small scale, where the characteristic time is comparable or less than the mean free time of heat carriers, it is well known that the conventional Fourier law leads to the inaccurate results. Also, the initial first and second-order time derivatives of temperature field control the occurrence of the overshooting phenomenon and the second derivative of temperature should be higher than the first derivatives of temperature.

The combined application of the DQM and the Newton Raphson method is used to solve the DPL, hyperbolic and Fourier heat conduction equations to obtain temperature, displacements and stresses in different kinds of nanocomposites. The DQM is used to discretize the spatial

derivatives as it employs quite a small number of grid points, then the obtained nonlinear system of ordinary differential equations is solved using the Newton-Raphson method in the temporal domain. The entire temporal domain is divided into a set of time intervals, and in each of them, the DQ rule is employed to discretize the temporal derivatives. After solving the DPL, hyperbolic, or Fourier heat conduction to obtain the temperature distribution and time history, the deformation and stress of the structures have been obtained under different boundary and initial conditions.

In nanoscale, it is shown that when the values of relaxation time are large, the time delay effect is restricted to a physical domain close to the boundary. On the contrary, decreasing the value of the time delay pushes the thermal waves forward. Furthermore, when the characteristic length is small, there is a sharp decline in temperature near the boundary, while the temperature or heat flux in the center of the medium based on the Fourier heat conduction has no difference than that obtained from DPL or hyperbolic heat conduction. The small characteristic length confines the effects of the interactions between boundary and energy carriers within a physical domain near the boundary for nanoscale structures.

One of the drawbacks of the presented method is the negative temperature which is experimentally impossible to occur. To justify this incident, there are two schools of thought, both of which based on extended irreversible thermodynamics and rational thermodynamics. They consider heat flux (q) as a parameter that varies with time, which makes it possible to have heat flux flowing from cold to hot without violating the second law of thermodynamics. This means in hyperbolic heat conduction both $\frac{\partial T}{\partial x}$ and q can have the same sign. It should be mention that even when heat flows from the cold to hot, the entropy rate is positive. Thus, the hyperbolic equations used in this study are compatible with the second law of thermodynamics whether or not it is physically real.

8.2 Recommendations for future work

The present research has made significant contributions to advanced heat conduction in applying state-of-the-art non-Fourier heat conduction models, and to applied mathematics in developing efficient tool for solving nonlinear, coupled sets of partial differential equations. However, these themes can be further enhanced and expanded. Following recommendations for conducting further research in these areas are suggested:

- As continuum formulation can be applied only for certain regimes or scales, more fundamental approaches based on particle behavior in heat conduction are preferable in the micro- and nanoscale domains.
- At the micro- and nanoscale of, the effect of appropriate spatial and time scales, in relation to the physical dimension of the domain, the speed at which the heat conduction occurs and the temperature ranges within which the heat conduction takes place need to be carefully considered. It is important to obtain the range at which each of these features lead to overshooting.
- Considering the effects of hyperbolic heat conduction in porous materials would be of great importance as they usually show a relatively high time lag.
- Since laser applies a high heat flux in a short period of time, the analysis of laser beam-induced heating is not possible using the classical Fourier law. An in-depth research in non-Fourier heat conduction models is needed here to prevent the damage to human tissue.
- There are three required conditions for overshooting to happen: (1) initial high temperature gradient; (2) thickness of the medium should be in a specific range; (3)

the right value of time lags. So, to have an accurate understanding of heat wave propagation in different materials and prevent overshooting, it is important to obtain the time lags experimentally.

- When there are different thermal shocks on the boundaries, there are more chance for heat waves to interfere. In this case, it is important to consider two-dimensional or three-dimensional problems in which the number of heat wave interferences increases and more likely overshooting phenomenon will occur.

References

- [1] D. Y. Tzou, Experimental support for the lagging behavior in heat propagation, *Journal of Thermophysics and Heat Transfer* 9 (4) (1995) 686–693.
- [2] L. Wang, X. Zhou, X. Wei, *Heat conduction: mathematical models and analytical solutions*, Springer Science & Business Media, 2007.
- [3] V. A. Cimmelli, K. Frischmuth, Nonlinear effects in thermal wave propagation near zero absolute temperature, *Physica B: Condensed Matter* 355 (1-4) (2005) 147–157.
- [4] S. C. Mishra, R. K. Chaurasia, Analysis of dual-phase-lag non-fourier conduction and radiation heat transfer in a planar slab, *Numerical Heat Transfer, Part A: Applications* 68 (9) (2015) 1010–1022.
- [5] T. Qiu, C. Tien, Heat transfer mechanisms during short-pulse laser heating of metals, *Journal of Heat Transfer* 115 (4) (1993) 835–841.
- [6] M. Xu, J. Guo, L. Wang, L. Cheng, Thermal wave interference as the origin of the overshooting phenomenon in dual-phase-lagging heat conduction, *International Journal of Thermal Sciences* 50 (5) (2011) 825–830.
- [7] C. Cattaneo, A form of heat-conduction equations which eliminates the paradox of instantaneous propagation, *Comptes Rendus* 247 (1958) 431.
- [8] P. Vernotte, Some possible complications in the phenomena of thermal conduction, *Compte Rendus* 252 (1961) 2190–2191.
- [9] T. Fung, Solving initial value problems by differential quadrature method part 1: first-order equations, *International Journal for Numerical Methods in Engineering* 50 (6) (2001) 1411–1427.

[10] H. Rahideh, P. Malekzadeh, M. G. Haghghi, Heat conduction analysis of multi-layered fgms considering the finite heat wave speed, *Energy conversion and management* 55 (2012) 14–19.

[11] K.-C. Liu, Y.-N. Wang, Y.-S. Chen, Investigation on the bio-heat transfer with the dual-phase-lag effect, *International Journal of Thermal Sciences* 58 (2012) 29–35.

[12] D. Y. Tzou, The generalized lagging response in small-scale and high-rate heating, *International Journal of Heat and Mass Transfer* 38 (17) (1995) 3231–3240.

[13] W. Dai, F. Han, Z. Sun, Accurate numerical method for solving dual-phase-lagging equation with temperature jump boundary condition in nano heat conduction, *International Journal of Heat and Mass Transfer* 64 (2013) 966–975.

[14] F. Guo, G. Wang, G. Rogerson, Analysis of thermoelastic damping in micro-and nanomechanical resonators based on dual-phase-lagging generalized thermoelasticity theory, *International Journal of Engineering Science* 60 (2012) 59–65.

[15] Grammenoudis P, Tsakmakis C. Micropolar plasticity theories and their classical limits. Part I: Resulting model. *Acta Mech* 189 (2007) 151–175.

[16] Motoo Fujii, Xing Zhang, Huaqing Xie, Hiroki Ago, Koji Takahashi, Tatsuya Ikuta, Hidekazu Abe, and Tetsuo Shimizu. Measuring the thermal conductivity of a single carbon nanotube. *Physical review letters*, 95(6):065502, 2005.

[17] R Mao, BD Kong, C Gong, S Xu, T Jayasekera, K Cho, and KW Kim. First-principles calculation of thermal transport in metal/graphene systems. *Physical Review B*, 87(16):165410, 2013.

[18] Bohayra Mortazavi and Sad Ahzi. Thermal conductivity and tensile response of defective graphene: A molecular dynamics study. *Carbon*, 63:460–470, 2013.

- [19] Victor A Ermakov, Andrei V Alaferdov, Alfredo R Vaz, Alexander V Baranov, and Stanislav A Moshkalev. Nonlocal laser annealing to improve thermal contacts between multi-layer graphene and metals. *Nanotechnology*, 24(15):155301, 2013.
- [20] Chunwei Zhang, Weiyu Chen, Yi Tao, Weiwei Zhao, Shuang Cai, Chenhan Liu, Zhenhua Ni, Dongyan Xu, Zhiyong Wei, Juekuan Yang, et al. Electron contributions to the heat conduction across au/graphene/au interfaces. *Carbon*, 115:665–671, 2017.
- [21] Deyu Li, Yiyang Wu, Philip Kim, Li Shi, Peidong Yang, and Arun Majumdar. Thermal conductivity of individual silicon nanowires. *Applied Physics Letters*, 83(14):2934–2936, 2003.
- [22] SL Sobolev. Equations of transfer in non-local media. *International journal of heat and mass transfer*, 37(14):2175–2182, 1994.
- [23] Robert Alan Guyer and JA Krumhansl. Solution of the linearized phonon boltzmann equation. *Physical Review*, 148(2):766, 1966.
- [24] RA Guyer and JA Krumhansl. Thermal conductivity, second sound, and phonon hydrodynamic phenomena in nonmetallic crystals. *Physical Review*, 148(2):778, 1966.
- [25] Linjuan Wang, Jifeng Xu, and Jianxiang Wang. A peridynamic framework and simulation of non-fourier and nonlocal heat conduction. *International Journal of Heat and Mass Transfer*, 118:1284–1292, 2018.
- [26] Mingtian Xu. A non-local constitutive model for nano-scale heat conduction. *International Journal of Thermal Sciences*, 134:594–600, 2018.
- [27] Navvab Shafiei, Mohammad Kazemi, MajidGhadiri, Nonlinear vibration of axially functionally graded tapered microbeams , *International Journal of Engineering Science* 102 (2016) 12-26.
- [28] Sundaramoorthy Rajasekarana, Hossein Bakhshi Khanikib, Bending, buckling and

vibration of small-scale tapered beams, *International Journal of Engineering Science*, 120 (2017) 172-188.

[29] A. Pourasghar, Z. T. Chen. Thermoelastic response of CNT reinforced cylindrical panel resting on elastic foundation using theory of elasticity. *Compos Part B/Eng.* 2016, 99, 436-44

[30] Ehsan Taati, On buckling and post-buckling behavior of functionally graded micro-beams in thermal environment, *International Journal of Engineering Science*, 128 (2018) 63-78.

[31] B. Shen and P. Zhang, Notable physical anomalies manifested in non-fourier heat conduction under the dual-phase-lag model, *International Journal of Heat and Mass Transfer*, 51, 1713–1727, 2008.

[32] W.-B. Lor and H.-S. Chu, Effect of interface thermal resistance on heat transfer in a composite medium using the thermal wave model, *International Journal of Heat and Mass Transfer*, 43, 653–663, 2000.

[33] A. Sasmal and S. C. Mishra, Analysis of non-fourier conduction and radiation in a differentially heated 2-d square cavity, *International Journal of Heat and Mass Transfer*, 79, 116–125, 2014.

[34] M. Al-Nimr and M. K. Alkam, Overshooting phenomenon in the hyperbolic microscopic heat conduction model, *International Journal of Thermophysics*, 24, 2, 577–583, 2003.

[35] A. Pourasghar and Z. Chen, Hyperbolic heat conduction and thermoelastic solution of functionally graded cnt reinforced cylindrical panel subjected to heat pulse, *International Journal of Solids and Structures*, 2018.

[36] A. Pourasghar and Z. Chen, Effect of hyperbolic heat conduction on the linear and

nonlinear vibration of cnt reinforced size-dependent functionally graded microbeams, *International Journal of Engineering Science*, 137, 57–72, 2019.

[37] S. Singh and S. Kumar, Numerical study on triple layer skin tissue freezing using dual phase lag bio-heat model, *International Journal of Thermal Sciences*, 86, 12–20, 2014.

[38] K.-C. Liu and H.-T. Chen, Investigation for the dual phase lag behavior of bio-heat transfer, *International Journal of Thermal Sciences*, 49, 1138–1146, 2010.

[39] M. Xu and L. Wang, Thermal oscillation and resonance in dual-phase-lagging heat conduction, *International Journal of Heat and Mass Transfer*, 45, 1055–1061, 2002.

[40] L. Wang and X. Zhou, Dual-phase-lagging heat conduction, 2000.

[41] J. Ghazanfarian and A. Abbassi, Effect of boundary phonon scattering on dual-phase-lag model to simulate micro-and nano-scale heat conduction, *International Journal of Heat and Mass Transfer*, 52, 3706–3711, 2009.

[42] H. Basirat, J. Ghazanfarian, and P. Forooghi, Implementation of dual-phase-lag model at different knudsen numbers within slab heat transfer, in *Proceedings of the International Conference on Modeling and Simulation (MS06), Konia, Turkey*, 895, 2006.

[43] P. J. Antaki, New interpretation of non-fourier heat conduction in processed meat, *Journal of Heat Transfer*, 127, 189–193, 2005.

[44] W. Kaminski, Hyperbolic heat conduction equation for materials with a nonhomogeneous inner structure, *Journal of Heat Transfer*, 112, 555–560, 1990.

[45] M. J. Noroozi, S. Saedodin, and D. D. Ganji, A new solution for nonlinear dual phase lagging heat conduction problem, *Alexandria Engineering Journal*, 552, 1745–1752, 2016.

[46] C. Shu, Q. Yao, and K. Yeo, Block-marching in time with dq discretization: an efficient method for time-dependent problems, *Computer Methods in Applied Mechanics and*

Engineering, 191, 4587–4597, 2002.

[47] A. Pourasghar and Z. Chen, Dual-phase-lag heat conduction in fg carbon nanotube reinforced polymer composites, *Physica B: Condensed Matter*, 2019.

[48] A. Pourasghar, R. Moradi-Dastjerdi, M. Yas, A. Ghorbanpour Arani, and S. Kamarian, Three-dimensional analysis of carbon nanotube-reinforced cylindrical shells with temperature-dependent properties under thermal environment, *Polymer Composites*, 39, 1161–1171, 2018.

[49] A. D. Polyanin and V. F. Zaitsev, *Handbook of nonlinear partial differential equations*. Chapman and Hall/CRC, 2016.

[50] C. Dorao, Simulation of thermal disturbances with finite wave speeds using a high order method, *Journal of computational and applied mathematics*, 231, 637–647, 2009.

[51] Y. J. Yu, C.-L. Li, Z.-N. Xue, and X.-G. Tian, The dilemma of hyperbolic heat conduction and its settlement by incorporating spatially nonlocal effect at nanoscale, *Physics Letters A*, 380, 255–261, 2016.

[52] T. Xiao, S. Gong, X. Lei, Z. Jiang, Y. Wang, D. Wu, Z. Xiao, Z. Zhu, Z. Li, High temperature response capability in carbon nanotube/polymer nanocomposites, *Composites Science and Technology*.

[53] D. Wentzel, S. Miller, I. Sevostianov, Dependence of the electrical conductivity of graphene reinforced epoxy resin on the stress level, *International Journal of Engineering Science* 120 (2017) 63–70.

[54] K.-t. Lau, C. Gu, D. Hui, A critical review on nanotube and nanotube/nanoclay related polymer composite materials, *Composites Part B: Engineering* 37 (6) (2006) 425–436.

[55] H. Dai, Carbon nanotubes: opportunities and challenges, *Surface Science* 500 (1-3) (2002) 218–241.

[56] H. K. Choi, H. Jung, Y. Oh, H. Hong, J. Yu, E. S. Shin, Analysis of the influence of interphase characteristics on thermal conduction in surface-modified carbon nanotube-reinforced composites using an analytical model, *Composites Science and Technology*.

[57] S. N. Leung, Thermally conductive polymer composites and nanocomposites: Processing-structure-property relationships, *Composites Part B: Engineering*.

[58] M. Chipara, J. Cruz, E. R. Vega, J. Alarcon, T. Mion, D. M. Chipara, E. Ibrahim, S. C. Tidrow, D. Hui, Polyvinylchloride-single-walled carbon nanotube composites: Thermal and spectroscopic properties, *Journal of Nanomaterials* 2012 (2012) 15.

[59] D. C. Hammerand, G. D. Seidel, D. C. Lagoudas, Computational micromechanics of clustering and interphase effects in carbon nanotube composites, *Mechanics of Advanced Materials and Structures* 14 (4) (2007) 277–294.

[60] M. Griebel, J. Hamaekers, Molecular dynamics simulations of the elastic moduli of polymer–carbon nanotube composites, *Computer methods in applied mechanics and engineering* 193 (17-20) (2004) 1773–1788.

[61] A. Selmi, C. Friebel, I. Doghri, H. Hassis, Prediction of the elastic properties of single walled carbon nanotube reinforced polymers: A comparative study of several micromechanical models, *Composites Science and Technology* 67 (10) (2007) 2071–2084.

[62] D. Luo, W.-X. Wang, Y. Takao, Effects of the distribution and geometry of carbon nanotubes on the macroscopic stiffness and microscopic stresses of nanocomposites, *Composites Science and Technology* 67 (14) (2007) 2947–2958.

[63] T. Gates, G. Odegard, S. Frankland, T. Clancy, Computational materials: multi-scale modeling and simulation of nanostructured materials, *Composites Science and Technology* 65 (15-16) (2005) 2416–2434.

[64] J. D. Eshelby, The determination of the elastic field of an ellipsoidal inclusion, and related problems, *Proceedings of the Royal Society of London. Series A. Mathematical and Physical Sciences* 241 (1226) (1957) 376–396.

[65] T. Mori, K. Tanaka, Average stress in matrix and average elastic energy of materials with misfitting inclusions, *Acta metallurgica* 21 (5) (1973) 571–574.

[66] R. Christensen, K. Lo, Solutions for effective shear properties in three phase sphere and cylinder models, *Journal of the Mechanics and Physics of Solids* 27 (4) (1979) 315–330.

[67] Z. Hashin, The differential scheme and its application to cracked materials, *Journal of the Mechanics and Physics of Solids* 36 (6) (1988) 719–734.

[68] M. M. Najafabadi, M. Ahmadian, E. Taati, Effect of thermal wave propagation on thermoelastic behavior of functionally graded materials in a slab symmetrically surface heated using analytical modeling, *Composites Part B: Engineering* 60 (2014) 413–422.

[69] I. Carlomagno, V. Cimmelli, A. Sellitto, Phonon and electron temperature and non-fourier heat transport in thin layers, *Physica B: Condensed Matter* 511 (2017) 61–67.

[70] Q. Zhuang, B. Yu, X. Jiang, An inverse problem of parameter estimation for time-fractional heat conduction in a composite medium using carbon–carbon experimental data, *Physica B: Condensed Matter* 456 (2015) 9–15.

[71] B. Yilbas, A. Al-Dweik, S. B. Mansour, Analytical solution of hyperbolic heat conduction equation in relation to laser short-pulse heating, *Physica B: Condensed Matter* 406 (8) (2011) 1550–1555.

[72] T. Fung, On the equivalence of the time domain differential quadrature method and the dissipative runge–kutta collocation method, *International journal for numerical methods in engineering* 53 (2) (2002) 409–431.

[73] J. Liu, X. Wang, An assessment of the differential quadrature time integration scheme for nonlinear dynamic equations, *Journal of Sound and Vibration* 314 (1-2) (2008) 246–253.

[74] J. Ding, Thermal and mechanical analysis of material response to nonsteady ramp and steady shock wave loading, *Journal of the Mechanics and Physics of Solids* 54 (2) (2006) 237–265.

[75] B. Zhou, W. Luo, J. Yang, X. Duan, Y. Wen, H. Zhou, R. Chen, B. Shan, Thermal conductivity of aligned cnt/polymer composites using mesoscopic simulation, *Composites Part A: Applied Science and Manufacturing* 90 (2016) 410–416.

[76] S. Hepplestone, A. Ciavarella, C. Janke, G. Srivastava, Size and temperature dependence of the specific heat capacity of carbon nanotubes, *Surface science* 600 (18) (2006) 3633–3636.

[77] A. Pourasghar, M. Yas, S. Kamarian, Local aggregation effect of cnt on the vibrational behavior of four-parameter continuous grading nanotube-reinforced cylindrical panels, *Polymer Composites* 34 (5) (2013) 707–721.

[78] D.-L. Shi, X.-Q. Feng, Y. Y. Huang, K.-C. Hwang, H. Gao, The effect of nanotube waviness and agglomeration on the elastic property of carbon nanotube-reinforced composites, *Journal of Engineering Materials and Technology* 126 (3) (2004) 250–257.

[79] T. Mura, *Micromechanics of defects in solids*, Springer Science & Business Media, 2013.

[80] M. Yas, A. Pourasghar, S. Kamarian, M. Heshmati, Three-dimensional free vibration analysis of functionally graded nanocomposite cylindrical panels reinforced by carbon nanotube, *Materials & Design* 49 (2013) 583–590.

[81] J. Jam, A. Pourasghar, S. Kamarian, Effect of the aspect ratio and waviness of carbon nanotubes on the vibrational behavior of functionally graded nanocomposite cylindrical panels, *Polymer Composites* 33 (11) (2012) 2036–2044.

[82] Shuangwen Li, Yiyu Feng, Yali Li, Wei Feng, and Katsumi Yoshino. Transparent and flexible films of horizontally aligned carbon nanotube/polyimide composites with highly anisotropic mechanical, thermal, and electrical properties. *Carbon*, 109:131–140, 2016.

[83] Shrouk A Karim, Alaa Mohamed, MM Abdel-Mottaleb, TA Osman, and A Khattab. Visible light photocatalytic activity of pan-cnts/zno-nh₂ electrospun nanofibers. *Journal of Alloys and Compounds*, 772:650–655, 2019.

[84] Yu Pan, ShiQi Xiao, Xin Lu, Chuan Zhou, Yang Li, ZhiWei Liu, BoWen Liu, Wei Xu, ChengChang Jia, and XuanHui Qu. Fabrication, mechanical properties and electrical conductivity of al₂o₃ reinforced cu/cnts composites. *Journal of Alloys and Compounds*, 782:1015–1023, 2019.

[85] Ifra Marriam, Fujun Xu, Mike Tebyetekerwa, Yang Gao, Wei Liu, Xiaohua Liu, and Yiping Qiu. Synergistic effect of cnt films impregnated with cnt modified epoxy solution towards boosted interfacial bonding and functional properties of the composites. *Composites Part A: Applied Science and Manufacturing*, 110:1–10, 2018.

[86] Young Seok Song and Jae Ryoun Youn. Influence of dispersion states of carbon nanotubes on physical properties of epoxy nanocomposites. *Carbon*, 43(7):1378–1385, 2005.

[87] Zdenko Špitalský, L`ibor Matějka, Miroslav Šlouf, Elena N Konyushenko, Jana Kovářová, Josef Zemek, and Jiř Kotek. Modification of carbon nanotubes and its effect on properties of carbon nanotube/epoxy nanocomposites. *Polymer Composites*, 30(10):1378–1387, 2009.

[88] Gui-Lin She, Yi-Ru Ren, and Kun-Ming Yan. On snap-buckling of porous fg curved nanobeams. *Acta Astronautica*, 2019.

[89] Amin Pourasghar, Mostafa Homauni, and Saeed Kamarian. Differential quadrature based nonlocal flapwise bending vibration analysis of rotating nanobeam using the eringen nonlocal elasticity theory under axial load. *Polymer Composites*, 37(11):3175–3180, 2016.

[90] AI Aria and MI Friswell. A nonlocal finite element model for buckling and vibration of functionally graded nanobeams. *Composites Part B: Engineering*, 166:233–246, 2019.

[91] Mohammad Reza Barati. On non-linear vibrations of flexoelectric nanobeams. *International Journal of Engineering Science*, 121:143–153, 2017.

[92] Liang Chen, Zhen Huang, and Satish Kumar. Phonon transmission and thermal conductance across graphene/cu interface. *Applied Physics Letters*, 103(12):123110, 2013.

[93] Shu-Wei Chang, Arun K Nair, and Markus J Buehler. Geometry and temperature effects of the interfacial thermal conductance in copper–and nickel–graphene nanocomposites. *Journal of Physics: Condensed Matter*, 24(24):245301, 2012.

[94] Patrick E Hopkins, Mira Baraket, Edward V Barnat, Thomas E Beechem, Sean P Kearney, John C Duda, Jeremy T Robinson, and Scott G Walton. Manipulating thermal conductance at metal–graphene contacts via chemical functionalization. *Nano letters*, 12(2):590–595, 2012.

[95] Yee Kan Koh, Myung-Ho Bae, David G Cahill, and Eric Pop. Heat conduction across monolayer and few-layer graphenes. *Nano letters*, 10(11):4363–4368, 2010.

[96] Bohayra Mortazavi and Timon Rabczuk. Multiscale modeling of heat conduction in graphene laminates. *Carbon*, 85:1–7, 2015.

[97] C Shu, L Wang, and YT Chew. Numerical computation of three-dimensional

incompressible navier–stokes equations in primitive variable form by dq method. *International Journal for Numerical Methods in Fluids*, 43(4):345–368, 2003.

[98] Z Zong and KY Lam. A localized differential quadrature (ldq) method and its application to the 2d wave equation. *Computational Mechanics*, 29(4-5):382–391, 2002.

[99] TC Fung. Stability and accuracy of differential quadrature method in solving dynamic problems. *Computer Methods in Applied Mechanics and Engineering*, 191(13-14):1311–1331, 2002.

[100] C-N Chen. Extended gdq and related discrete element analysis methods for transient analyses of continuum mechanics problems. *Computers & Mathematics with Applications*, 47(1):91–99, 2004.

[101] M Tanaka and W Chen. Coupling dual reciprocity bem and differential quadrature method for time-dependent diffusion problems. *Applied Mathematical Modelling*, 25(3):257–268, 2001.

[102] DY Tzou. Nonlocal behavior in phonon transport. *International Journal of Heat and Mass Transfer*, 54(1-3):475–481, 2011.

[103] Amin Pourasghar and Saeed Kamarian. Dynamic stability analysis of functionally graded nanocomposite non-uniform column reinforced by carbon nanotube. *Journal of Vibration and Control*, 21(13):2499–2508, 2015.

[104] Ngabonziza Y, Li J, Barry C.F. Electrical conductivity and mechanical properties of multiwalled carbon nanotube-reinforced polypropylene nanocomposites. *Acta Mech.* 220 (2011) 289-298.

[105] Moradi-Dastjerdi R, Pourasghar A., Foroutan M. The effects of carbon nanotube orientation and aggregation on vibrational behavior of functionally graded nanocomposite

cylinders by a mesh-free method. *Acta Mech.* 224 (2013) 2817–2832.

[106] Kundalwal S.I, Meguid S.A. Effect of carbon nanotube waviness on active damping of laminated hybrid composite shells. *Acta Mech.* 226 (2015) 2035–2052.

[107] Allaoui A, Bai S, Cheng HM, Bai JB. Mechanical and electrical properties of a MWNT/epoxy composite. *Comput Sci Technol.* 62 (2002)1993–98.

[108] Han Y, Elliott J. Molecular dynamics simulations of the elastic properties of polymer/carbon nanotube composites. *Comput Mater Sci.* 39 (2007) 315–23.

[109] Griebel M, Hamaekers J, Heber F. A molecular dynamics study on the impact of defects and functionalization on the Young modulus of boron–nitride nanotubes. *Comput Mater Sci* 45 (2009) 1097–1103.

[110] Liu YJ, Chen XL. Evaluations of the effective material properties of carbon nanotube-based composites using a nanoscale representative volume element. *Mech Mater* 35 (2003) 69–81.

[111] G.D. Seidel, D.C. Lagoudas, Micromechanical analysis of the effective elastic properties of carbon nanotube reinforced composites, *Mechanics of Materials.* 38 (2006) 884–907

[112] Eshelby JD. The determination of the elastic field of an ellipsoidal inclusion and related problems. *Proc R Soc.*241 (1957)376–396.

[113] Mori T, Tanaka K. Average stress in matrix and average energy of materials with misfitting inclusion. *Acta Metall.* 21 (1973) 571–574.

[114] Christensen RM, Lo KH. Solutions for effective shear properties in three sphere and cylinder models. *J Mech Phys Solids.* 27 (1979) 315–330.

[115] Hashin Z. The differential scheme for its application to cracked materials. *J Mech Phys Solids.* 36 (1988) 719–734.

[116] Qing-sheng Yang a, Xiao-qiao He b, Xia Liu a, Fang-fang Leng a, Yiu-Wing Mai, The effective properties and local aggregation effect of CNT/SMP composites, *Composites: Part B* 43 (2012) 33–38.

[117] Pallab Barai, George J. Weng, A theory of plasticity for carbon nanotube reinforced composite, *International journal of plasticity*, 27 (2011) 539–559.

[118] B. Safaei, R. Moradi-Dastjerdi, Z. Qin, F. Chu, Frequency-dependent forced vibration analysis of nanocomposite sandwich plate under thermo-mechanical loads, *Composites Part B: Engineering* 161 (2019) 44–54.

[119] R. Kolahchi, B. Keshtegar, M. H. Fakhar, Optimization of dynamic buckling for sandwich nanocomposite plates with sensor and actuator layer based on sinusoidal-visco-piezoelasticity theories using grey wolf algorithm, *Journal of Sandwich Structures & Materials* (2017) <https://doi.org/10.1177/1099636217731071>.

[120] B. Safaei, R. Moradi-Dastjerdi, F. Chu, Effect of thermal gradient load on thermo-elastic vibrational behavior of sandwich plates reinforced by carbon nanotube agglomerations, *Composite Structures* 192 (2018) 28–37.

[121] R. Moradi-Dastjerdi, H. Malek-Mohammadi, Biaxial buckling analysis of functionally graded nanocomposite sandwich plates reinforced by aggregated carbon nanotube using improved high-order theory, *Journal of Sandwich Structures & Materials* 19 (6) (2017) 736–769.

[122] R. Kolahchi, M. S. Zarei, M. H. Hajmohammad, A. Nouri, Wave propagation of embedded viscoelastic fg-cnt-reinforced sandwich plates integrated with sensor and actuator based on refined zigzag theory, *International Journal of Mechanical Sciences* 130 (2017) 534–545.

[123] R. Moradi-Dastjerdi, H. Malek-Mohammadi, H. Momeni-Khabisi, Free vibration

analysis of nanocomposite sandwich plates reinforced with cnt aggregates, ZAMM-Journal of Applied Mathematics and Mechanics/Zeitschrift für Angewandte Mathematik und Mechanik 97 (11) (2017) 1418–1435.

[124] M. H. Hajmohammad, M. S. Zarei, A. Nouri, R. Kolahchi, Dynamic buckling of sensor/functionally graded-carbon nanotube-reinforced laminated plates/actuator based on sinusoidal-visco-piezoelectricity theories, Journal of Sandwich Structures & Materials (2017) <https://doi.org/10.1177/1099636217720373>.

[125] R. Shokri-Oojghaz, R. Moradi-Dastjerdi, H. Mohammadi, K. Behdinan, Stress distributions in nanocomposite sandwich cylinders reinforced by aggregated carbon nanotube, Polymer Composites. DOI: 10.1002/pc.25206.

[126] SJ Salami, Extended high order sandwich panel theory for bending analysis of sandwich beams with carbon nanotube reinforced face sheets, Physica E 76 (2016) 187–197.

[127] Xiang HJ, Yang J. Free and forced vibration of a laminated FGM Timoshenko beam of variable thickness under heat conduction. Compos Part B/Eng 2008;39:292–303.

[128] Ke LL, Yang J, Kitipornchai S. Nonlinear free vibration of functionally graded carbon nanotube-reinforced composite beams. Compos Struct 92 (2010) 676–683.

[129] Ke LL, Wang Y, Yang J, Kitipornchai S. Nonlinear free vibration of size-dependent functionally graded microbeams, International Journal of Engineering Science 50 (2012) 256–267.

[130] Min Tang, Qiao Ni, LinWang, Yangyang Luo, Yikun Wang, Size-dependent vibration analysis of a microbeam in flow based on modified couple stress theory, International Journal of Engineering Science 85 (2014) 20–30.

[131] Shafiei N, Mousavi A, Ghadiri M, On size-dependent nonlinear vibration of porous and imperfect functionally graded tapered microbeams, International Journal of Engineering

Science 102 (2016) 12–26.

[132] Rasool Moradi-Dastjerdi, Amin Pourasghar, Dynamic analysis of functionally graded nanocomposite cylinders reinforced by wavy carbon nanotube under an impact load, *Journal of Vibration and Control* 22 (2016) 1062-1075.

[133] Prylutskyi YI, Durov SS, Ogloblya OV, Buzaneva EV, Scharff P. Molecular dynamics simulation of mechanical, vibrational and electronic properties of carbon nanotubes. *Comput Mater Sci* 17 (2000) 352–355.

[134] C. Shu, *Differential quadrature and its application in engineering*, Springer, Berlin, (2000).

[135] Shu, C., Richards BE, Application of generalized differential quadrature to solve two-dimensional incompressible Navier Stokes equations, *Int. J. Numer Meth. Fluid*, 15 (1992) 791-798.

[136] J. E. Jam, A. Pourasghar, S.kamarian, Sh. Maleki, Characterizing elastic properties of carbon nanotube-based composites by using an equivalent fiber, *Polymer Composites* 34 (2013) 241–251.

[137] Babaei MH, Chen Z. Transient hyperbolic heat conduction in a functionally graded hollow cylinder. *J Thermo Phys Heat Trans* 2010; 24:325–30.

[138] H.T. Thai, S.E. Kim, Size-dependent functionally graded Kirchhoff and Mindlin plate models based on a modified couple stress theory, *Compos Struct.* 95 (2013) 142–153.

[139] Ke LL, Wang Y, Yang Z. Thermal effect on free vibration and buckling of size-dependent microbeam, *Physica E* 43 (2011) 1387-1393.

[139] Mitra, K., Kumar, S., Vedevarz, A., & Moallemi, M. K. (1995). Experimental Evidence of Hyperbolic Heat Conduction in Processed Meat. *Journal of Heat Transfer*, 117(3),

568.

[140] Novichenok, N.L. and Shul'man, Z.P., *Teplofizicheskie svoistva polimerov* (Thermal Properties of Polymers), Minsk: Nauka i tekhnika, 1971.

[141] A.D. Polyenin, A.I. Zhurov, A.V. Vyaz'min, Exact solutions of nonlinear heat- and mass transfer equations, *Theor. Found. Chem. Eng.* 34 (2000) 403–415.

[142] Gülnihal Meral, Differential quadrature solution of heat- and mass-transfer equations, *Applied Mathematical Modelling* 37 (2013) 4350–4359.

[143] L. H. Liu, H. P. Tan, and T. W. Tong, Non-Fourier effects on transient temperature response in semitransparent medium caused by laser pulse, *International Journal of Heat and Mass Transfer*, 44 (2001). 3335–3344.

[144] Kang I., Heung Y., Kim J., Lee J., Gollapudi R., Subramaniam S., Narasimhadevara S., Hurd D., Kirker G., Shanov V., Schulz M., Shi D., Boerio J., Mall S., Ruggles-Wren D., Introduction to carbon nanotube and nanofiber smart materials, *Compos Part B-Eng* 37 (2006) 382-394.

[145] Jackson E.M, Laibinis P.E, Collins W.E, Ueda A, Wingard C.D, Penn B, Development and thermal properties of carbon nanotube-polymer composites, *Compos Part B-Eng* 89 (2016) 362-373.

[146] J.M.L. Reis, R.P. Lima, S.D. Vidal, Effect of rate and temperature on the mechanical properties of epoxy BADGE reinforced with carbon nanotubes, <https://doi.org/10.1016/j.compstruct.2017.11.081>

[147] Odegard GM, Gates TS, Wise KE, Park C, Siochi EJ., Constitutive modelling of nanotube-reinforced polymer composites. *Compos Sci Technol* 63 (2003) 1671-87.

[148] Hyun Su Kim, Ji-un Jang, Jaesang Yu, Seong Yun Kim, Thermal conductivity of

polymer composites based on the length of multi-walled carbon nanotubes, *Compos Part B-Eng*79 (2015) 505-512.

[149] J. Gou, B. Minaie, B. Wang, Z. Liang, C. Zhang., Computational and experimental study of interfacial bonding of single-walled nanotube reinforced composites stiffness, *Comput Mater Sci*, 31 (2004) 225-236

[150] Berber S, Kwon Y-K, Tománek D. Unusually high thermal conductivity of carbon nanotubes. *Phys Rev Lett*84 (2000) 4613-6.

[151] Liu. T. T, Wang. X., Dynamic elastic modulus of single-walled carbon nanotubes in different thermal environments, *Physics Letters A* 365 (2007) 144-148.

[152] Hong W-T, Tai N-H, Investigations on the thermal conductivity of composites reinforced with carbon nanotubes. *Diamond Relat Mater*17 (2008) 1577-81.

[153] Yas MH, Pourasghar A, Kamarian S, Heshmati M. Three-dimensional free vibration analysis of functionally graded nanocomposite cylindrical panels reinforced by carbon nanotube. *Material and Design* 49 (2013) 583-590.

[154] A. Pourasghar, Z. Chen, Thermoelastic response of CNT reinforced cylindrical panel resting on elastic foundation using theory of elasticity, *Compos Part B-Eng* 99 (2016) 436-444

[155] Shen H.S., Xiang Y, Postbuckling of axially compressed nanotube-reinforced composite cylindrical panels resting on elastic foundations in thermal environments, *Compos Part B-Eng*67 (2014) 50-61.

[156] Alibeigloo A, Elasticity solution of functionally graded carbon nanotube-reinforced composite cylindrical panel subjected to thermo mechanical load, *Compos Part B-Eng*87 (2016) 214-226.

[157] Bahtui A, Eslami MR. Coupled thermoelasticity of functionally graded cylindrical shells. *Mech Res Commun* 34 (2007) 1-18.

[158] Hui-Shen Shen, Y. Xiang, Yin Fan, Nonlinear vibration of functionally graded graphene-reinforced composite laminated cylindrical shells in thermal environments, *Composite Structures* 182 (2017) 447–456

[159] Shen H.S., Postbuckling of nanotube-reinforced composite cylindrical shells in thermal environments. Part II: Pressure-loaded shells. *Compos. Struct.* 93 (2011) 2496-503.

[160] Alibeigloo. A, Liew. K. M., Thermoelastic analysis of functionally graded carbon nanotube reinforced composite plate using theory of elasticity, *Composite Structures* 106 (2013) 873-881.

[161] Yas, M. and Aragh, B. S., 2010. ‘Three-dimensional analysis for thermoelastic response of functionally graded fiber reinforced cylindrical panel’, *Composite Structures* 92 (10), 2391–2399.